SOLAR AND STELLAR CORONAL PLASMAS

NASA Grant NAGW-112

Semiannual Report #12 – #17

For the Period 1 May 1986 through 30 April 1989

Principal Investigator
Dr. Leon Golub

April 1989

Prepared for:

National Aeronautics Space Administration
Headquarters
Washington, D. C. 20546

Smithsonian Institution
Astrophysical Observatory
Cambridge, Massachusetts 02138

The Smithsonian Astrophysical Observatory
is a member of the
Harvard-Smithsonian Center for Astrophysics

The NASA Technical Officer for this grant is Dr. S. Kane, Code ES, NASA Headquarters, Washington, DC 20546.

SOLAR AND STELLAR CORONAL PLASMAS

NASA Grant NAGW-112

Semiannual Report #12 – #17

For the Period 1 May 1986 through 30 April 1989

Principal Investigator
Dr. Leon Golub

April 1989

Prepared for:

National Aeronautics Space Administration
Headquarters
Washington, D. C. 20546

Smithsonian Institution
Astrophysical Observatory
Cambridge, Massachusetts 02138

The Smithsonian Astrophysical Observatory
is a member of the
Harvard-Smithsonian Center for Astrophysics

The NASA Technical Officer for this grant is Dr. S. Kane, Code ES, NASA Headquarters, Washington, DC 20546.

I. Progress Summary

Work performed during the past year is summarized in this section. The discussion is subdivided into subject areas, as indicated.

The following work has been completed in the area of solar and stellar magnetic fields, related photospheric phenomena and the relationships between magnetism, rotation, coronal and chromospheric emission in solar-like stars:

A paper on the comparison between x-ray bright points (XBP) and He I 10830 dark points (Golub, Harvey, Herant and Webb 1989) was completed. Using several sets of simultaneous x-ray and He I 10830 images we compared dark points in He I with XBP on the x-ray images. For the largest and most obvious features there is a strong correlation; however, about two-thirds of the x-ray features were *not* identified on the He I images. Once an x-ray feature is located, it is nearly always possible to find a corresponding He I feature. The conclusion is that, using current selection methods, the He I 10830 data cannot be used as a one-to-one proxy for the x-ray data.

Schrijver 2et al. (1989) have derived an improved relation between magnetic flux (Φ_B and chromospheric Ca II H+K line core emission flux densities (ΔF_{CaII}) for solar active and quiet regions. They find that ΔF_{CaII} approximates $\Phi_B^{0.6}$, in contrast with previous determinations of a linear relationship (which were biased due to analysis of data with a much smaller range in ΔF_{CaII} amd Φ_B). The new ΔF_{CaII}-Φ_B relation is nearly identical with a preliminary one found for less active dwar stars (Saar and Schrijver 1987), which in turn is consistent with stellar X-ray - magnetic flux and stellar flux-flux (ΔF_{CaII}-F_X) correlations (Saar and Schrijver 1987; Schrijver 1983). The agreement between relations derived for individual solar active regions and from hemisphere-averaged stellar data implies that important physical similarities exist between magnetic structures on the Sun and magnetically "quiet" dwaraf stars, at least at the chromospheric level. The internal consistency of the solar and stellar chromospheric and coronal relations further implies that the same may hold true in stellar coronae. The nonlinearity of the stellar ΔF_{CaII}-F_X may then suggest that the chromospheres and coronae of

Table of Contents

cool stars are heated by different mechanisms.

Bopp *et al.* (1989) have made a detailed study of the interesting binary star, HD 17433. They find that the star lies above the main sequence and may be quite young (approximately Pleiades age). Magnetic activity levels in HD 17433 are high, with chromospheric, transition region, and coronal emission fluxes at the stellar suraface up to 200 times that of the active Sun. Consistent with these elevated activity levels, Bopp *et al.* (using an improved magnetic line profile model) estimate that roughly 66% of the photosphere is covered by magnetic regions with a mean field strength of 2000 Gauss. This represents the irst successful detection of a magnetic field on an active subgiant. Interestingly, the derived magnetic parameters are considerably larger than those expected from extrapolation of the preliminary relations found for dwarafs (Saar 1987).

The TiO bands are sensitive indicators of temperature in stellar atmospheres. The very presence of these features in dwarf stars with $T_{eff} > 4250$ K (approx K5V) is direct evidence for cool sp[ots. Saar and Nefff (1988) used observations of two TiO bands with differing temperature sensitivities to extract both the temperature (from the relative band depths) and the projected area (from the absolute band strengths relative to the continuum) of stellar spots. Two X-ray bright K dwarfs were studied and spots with ΔT approx 750 K were found to cover approximately 20% of the surface of BD+26730. The spectroscopic technique of determining star spot properties is superior to photometric techniques, which have difficulty detecting spots if there is no rotational modulation o the stellar light. A full description of this work will be submitted to Ap.J. Letters shortly.

Theoretical studies have been carried out in the following areas, among others:

1. Neutral Beams as the Dominant Energy Transport Mechanism in Two-Ribbon Flares

We have presented an alternative to the model of mildly relativistic electron beam for the transportation of flare-energy from the corona to the chromosphere (see Dennis (Sol. Phys. 100): neutral berams of protons and electrons with equal velocity and with the protons, by virtue of their larger

mass, carrying most of the beam energy. In Martens (1988) the basic physical model is derived and found to be in agreement with observational requirements. In Martens and Young (1989) we make a detailed comparison with the observationally much better documented acceleration of protons in the geomagnetic tail, and find great similarity between the two. In Korevaar and Martens (1989) recent observations of polarized emission lines are reviewed, which clearly favor neutral beams over electron beams. Also, the dimensionless model equations for the proton acceleration are derived and found to have the same parameters as those for the geotail: this makes numerical results for the geotail directly applicable to solar two-ribbon flares.

2. MHD and Circuit Models for Filament Eruptions

We have modelled the formation and eruption of solar prominences with different approaches and compared the results. An MHD equilibrium model (van Ballegooijen and Martens 1989) has demonstrated the formation of a filament as the result of cancellation of photospheric flux at the neutral line, and the subsequent loss of equilibrium as more and more flux cancels. This is consistent with the scenario derived from recent observations by Martin and coworkers. A simplified circuit code (Martens and Kuin 1989) reproduces the results of the MHD equilibrium calculations exactly and moreover, is also able to follow the filament after its loss of equilibrium. The filament is found to erupt, and its velocity curve is in agreement with that of typical filament eruptions. We are now modeling specific flares for which detailed velocity curves are available from observations.

3. Studies of Radio Emission Mechanisms in Transient Events

Tearing modes and Alfven waves are important phenomena in plasma astrophysics and in laboratory plasma. The periodicity of tearing modes has been observed in experiments of tokamak plasma (Sunnji Tsiji, 1983). Huang (1987) derived a complex eigenvalue of tearing modes from MHD theory and found that the real part is consistent with the growth rate for tearing modes in the classical theory (Furth *et al.*, 1963). The imaginary part (or the frequency) is just in the range of Alfven waves (the phase velocity of tearing modes has the same magnitude as Alfven velocity). Therefore, Huang (1988)

considered the plasma resistivity and the electric current along magnetic field line and derived the growth rate of Alfven waves, which is directly proportional to the plasma resistivity and the electric current density. The modulation of Alfven waves for the motion of a single electron possibly results in the resonance wave-particle interaction (Huang, 1989), and the growth rate of Alfven waves in this case is one or two orders of magnitude higher than the linear exponential growth rate and leads to a turbulent spectrum, which is a possible explanation for the anomalous growth of tearing modes.

The following radio observations designed for coronal activity studies of the Sun and of solar-type coronae are in progress:

a. Solar Observations

In conjunction with T. Bastian at NRAO we are in the process of calibrating a unique database on two solar active regions. The data consist of VLA and OVRO observations. The OVRO observations - made over a very wide range of frequencies - are complementary to the high spatial resolution VLA observations that were made at 10 frequencies in a 500 MHz band at 5 GHz and at 1.4 and 8 GHz. This database will allow us to study for the first time the structure of active regions as a function of frequency, and allow us to build a consistent model of the radio emission. However, analysis has been delayed by the discovery during the calibration procedure that the VLA's calibration of solar observations was in error. The error has been traced and corrected.

In conjunction with J. Neff at GSFC, we have obtained a very deep SWP high dispersion spectra of the Lyman-α line from a G type subgiant star. The unique aspect of this work is that the star has a radial velocity sufficiently high to remove the Lyman-α line core from the ISM absorption. Thus, we will be able to model the line emission from a star of spectral type similar to the Sun, but with a different effective gravity. This procedure should allow us to understand more clearly the formation mechanism of this line in the Solar atmosphere.

b. Stellar Observations

In collaboration with observers at Haystack, we initiated and performed a very sensitive VLBI experiment in an attempt to directly measure the sizes of the radio-emitting regions of stellar coronae. Of the six stars observed, three were detected and two were resolved. For two stars, we were able to place a limit on the size of the quiescent radio emission less than 0.4 stellar diameters. These are the first measurements of the sizes of stellar coronae. The success of these observations has also allowed us to immediately eliminate at least one possible radio emission mechanism (gyroresonance emission) from consideration.

In conjunction with T. Bastian at NRAO, we are in the process of finalizing the analysis of several exceptionally large stellar radio flares on the M Dwarf AD Leo. These flares were remarkable in that the emission -- despite the fact that it MUST have been produced by a coherent mechanism such as an electron-cyclotron maser or plasma radiation -- was broadband in nature ($\delta\nu/\nu > 0.03$). This observation has forced a revision in the idea that the coherent mechanisms must be intrinsically narrow-band. As a consequence, it appears that the quiescent emission from M dwarfs may be attributable to a superposition of many small flare-like events.

II. Bibliography - Work Completed During the Past Year

A. Refereed Publications

Golub, L., K. L. Harvey, M. Herant and D. F. Webb 1989, "X-ray Bright Points and He I 10830 Dark Points", Solar Physics (submitted).

Saar, S. H. and J. E. Neff 1988, "Spot Temperatures and Area Coverages on Active Dwarf Stars", in IAU Colloq. 104, eds. Haisch and Rodono.

Maggio, A. *et al.* 1988, "Einstein Observatory Magnitude Limited Survey of Late-Type Giant and Supergiant Stars", Astrop. J. (in press).

Saar, S. H. 1988, "The Magnetic Fields on Cool Stars and Their Correlation with Chromospheric and Coronal Emission".

Golub, L., T. W. Hartquist and A. C. Quillen 1989, "Comments on the Observability of Coronal Variations", Solar Physics (in press).

Schrijver, C.J., J. Cote, C. Zwann, and S.H. Saar 1989, "Relations Between the Photospheric Magnetic Field and the Emission from the Outer Atmospheres of Cool Stars I. The Solar Ca II K Line-Core Emission", Ap.J., 337, 964.

Bopp, B.W., S.H. Saar *et al.* 1989, "The Active Chromosphere Binary HD 17433 (VY Ari)", Ap.J., April 15.

P.C.H. Martens 1988, "The Generation of Proton Beams in Two-Ribbon Flares", Ap.J. Lett. 330, L131-L133.

P.C.H. Martens and A. Young 1989, "Proton Acceleration in Solar Flares and in The Geomagnetic Tail: A Comparison", in 2Nonlinear Effects in Vlasov Plasmas" Ed.F. Doveil, Editions de Physique, Orsay.

P.C.H. Martens and N.P.M. Kuin 1989, "A Circuit Model for Filament Eruptions and Two-Ribbon Flares", Sol. Phys., in press.

A.A. van Ballegooijen and P.C.H. Martens 1989, "Formation and Eruption of Solar Prominences", Ap.J., in press.

P. Korevaar and P.C.H. Martens 1989, "Time Dependent Corona Models: Scaling Laws", submitted to Astron. Astrophys.

P.C.H. Martens and A. Young 1989, "Neutral Beams in Two-Ribbon Flares and in the Geomagnetic Tail", submitted to Ap.J.

Golub, L., K. L. Harvey and D. F. Webb 1986, "Magnetogram and Soft X-ray Comparison of XBP and ER". NASA CP-2442, ed. A. I. Poland.

Bookbinder, J.A., E.W. Brugel and A. Brown 1989, "Mg II Line Profiles of the Mira S Carinae", Ap.J., in press..

Neff, D.H. *et al.* 1989, "Chromospheric and Coronal Emission Properties of a Volume-Limited Sample off K Dwarf Stars", submitted to Ap.J.

Bookbinder, J.A. *et al.* 1989 "Dynamic Spectra of Radio Bursts from Flare Stars", submitted to Ap.J.

Bookbinder, J.A. 1989, "A Radio Survey of Low X-ray Luminosity M Stars", submitted to Ap.J.

Bookbinder, J.A., L. Golub and R. Rosner 1989, "The Einstein Stellar Survey: K and M Stars", submitted to Ap.J.

B. Abstracts, Conference Talks, etc.

Saar, S.H. and J.E. Neff "Spot Temperatures and Area Coverages on Active Dwarf Stars", 1988, in IAU Colloquium 104, *Solar and Stellar Flares, Poster Volume*, eds. B.M. Haisch and M. Rodono (Catania: Catania Astrophysical Observatory) in press.

Bruning, D.H. and S.H. Saar "Line Asymmetries in Late-type Dwarf Photospheres", 1988, in *The NATO Advanced Research Workshop on Solar and Stellar Granulation* ed R. Rutten and G. Severino (Dordrecht: Kluwer) in press.

Bruning, D.H. and S.H. Saar "Spectral LineAsymmetries in Late-type Dwarf Photospheres", 1988, Bull. A.A.S., 20, 696.

Saar, S.H. *et al.* "Correlations Between He I D3 and Rotation in G and K Dwarfs", 1988, Bull. A.A.S. 20, 997.

Ambruster, C.A. and S.H. Saar "IUE Emission Line and Magnetic Field Variability of the Subgiant K Star HD 17433", 1988, Bull, A.A.S. 20, 995.

G. Huang "The Polarization and Harmonic Structure of Solar Radio Spikes", 1989, Bull. A.A.S. 20, 979.

Bookbinder, J.A. "Dynamic Spectra of Stellar Radio Bursts" 1989, URSI Commission J, Boulder CO.

Bookbinder, J.A. "Stellar Radio Emission, in Activity in Cool Star Envelopes" 1988, eds. O. Havnes, B. Pettersen, J. Schmitt and J.E. Solheim, Kluwer Publishers, p. 257.

Stencel, R.S., J.A. Bookbinder and K. Holtrop "Dusty Plasmas in Astrophysics" 1988 in 2nd Kansas Workshop on Plasma Astrophysics, ed. T. Armstrong.

Bookbinder, J.A., T.S. Bastian, G.A. Dulk and M.M. Davis 1988, in IAU Colloq. 104.

Herant, M. *et al.* "Multi-Wavelength Observations of the 23 June 1745UT M8 Flare" 1989 173 AAS Mtg. Boston, MA.

Quillen, A., L. Golub, F.R. Harnden, Jr. and S. Saar "Comparison of Predicted vs. Measured Stellar Magnetic Fields" 1988, 171st AAS mtg., Austin TX.

Center for Astrophysics
Preprint Series No. 2820

X-RAY BRIGHT POINTS AND He λ10830 DARK POINTS

L. Golub
Smithsonian Astrophysical Observatory

K. L. Harvey
Solar Physics Research Corporation

M. Herant
Harvard University

and

D. F. Webb
Emmanuel College
and
American Science & Engineering

X-RAY BRIGHT POINTS AND He I λ10830 DARK POINTS

L. Golub
Smithsonian Astrophysical Observatory
Cambridge, Mass.

K. L. Harvey
Solar Physics Res. Corp.*
Tucson, Ariz.

M. Herant, Harvard University
Cambridge, Mass.

and

D. F. Webb
Emmanuel College
Boston, Mass.
and
American Science & Engineering
Cambridge, Mass.

* Visitor, National Solar Observatory. National Optical Astronomy Observatories operated by the Association of Universities for Research in Astronomy, Inc. under contract with the National Science Foundation.

ABSTRACT

Using near-simultaneous full disk Solar x-ray images and He I 10830Å spectroheliograms from three recent rocket flights, we compare dark points identified on the He I maps with x-ray bright points identified on the x-ray images. We find that for the largest and most obvious features there is a strong correlation: most He I dark points correspond to x-ray bright points. However, about two-thirds of the x-ray bright points were not identified on the basis of the helium data alone. Once an x-ray feature is identified it is almost always possible to find an underlying dark patch of enhanced He I absorption which, however, would not *a priori* have been selected as a dark point. Therefore, the He I dark points, using current selection criteria, cannot be used as a one-to-one proxy for the x-ray data. He I dark points do, however, identify the locations of the stronger x-ray bright points.

1. Introduction

The name "x-ray bright point" or XBP was given to the numerous small regions of enhanced emission which were seen on early high resolution x-ray images (Vaiana *et al.* 1970) of the Solar corona. For large, long-lived regions, whenever detailed comparison between coronal features and magnetic field maps is performed, one finds that non-flaring coronal emission is associated with closed loop structures which appear as bipoles on magnetograms and as loops in x-rays (Vaiana and Rosner 1978). For the smallest features the comparison is not as striaghtforward, particularly because there are many small magnetic bipoles which are not associated with any obvious x-ray emission. The XBP, which are associated with magnetic bipoles, are so numerous that if they are caused by newly emerging magnetic flux, then they could be responsible for the vast majority of the emerging magnetic flux coming to the Solar surface (Golub *et al.* 1977).

The sharp division in x-ray brightness between open and closed regions is particularly useful for identifying and studying small bipolar regions. Such studies have indicated that the vast majority of closed, compact emission features in the corona correspond to regions having lifetime τ of two days or less (Golub *et al.* 1974). For the larger (τ > 2 days) regions, it is clear that they represent emerging flux: these regions generally develop arch filament systems and pores, and occasionally small sunspots. The more numerous shorter-lived regions exhibit fewer indicators of flux emergence; until now we have only established that there is a statistical correlation between magnetic bipole separation and magnetic flux, and the age of the XBP (Golub *et al.* 1977).

Unfortunately, because x-ray observations can only be obtained from instruments above the atmosphere, only infrequent sounding rocket x-ray data with sufficient spatial resolution and sensitivity to detect XBP have been obtained since the Skylab mission. On the other hand, daily groundbased full disk He I λ10830 spectroheliograms have been available since *Skylab* from the National Solar Observatory (NSO) at Kitt Peak. The Helium data have been used, among other things, for studying the small regions which are called "dark points" when seen in Helium, under the working hypothesis that there is a one-to-one association between dark points and XBP. This assumption is based on a study carried out in 1973 (Harvey *et al.* 1975) using some of the earliest He I data available. This study was

a qualitative comparison of four pairs of observations in x-rays and He I D_3, which is essentially identical to He I 0830 (Harvey and Hall 1971; Giovanelli *et al.* 1972).

The He λ10830 absorption line is produced by He I in its triplet state. It is formed in the chromosphere, at about the same height as the Ca K and H_α lines. Goldberg (1939; see also Zirin 1975; Kahler, Davis and Harvey 1983) suggested that UV emission from the corona can overpopulate the triplet state of He I through photoionization followed by recombination. This model explains the resemblance between He I spectroheliograms and x-ray maps, as well as the presence of a faint network similar to that which can be seen in Ca K or H_α.

Because of the correlation between x-ray emission and He I absorption, combined with the relative lack of x-ray data in recent years, there has been a tendency within the Solar community to use the He I λ10830 spectroheliograms as a substitute for the unavailable coronal x-ray data. While this has been shown to be justified in the case of large, long-lived structures such as active regions and coronal holes (Kahler, Davis and Harvey 1983), quantitative comparisons of the smallest features have not until now been carried out. The purpose of this letter is to show that the validity of using He I dark points as a proxy for x-ray bright points is limited and that He I λ10830 maps and x-ray images, despite evident similarities, cannot be used interchangably.

2. Comparison of He I λ10830 and X-ray Data

K. Harvey (1985) conducted an extensive survey of NSO magnetograms and He I λ10830 spectrohelioqrams collected from 1970 to 1984, partly as an attempt to analyze in detail the connection between magnetic activity and small coronal features. Within the time frame of this study, three x-ray datasets which are appropriate for use in this study were obtained from flights of the A.S.&.E. rocket-borne grazing incidence telescope (see Vaiana *et al.* 1973 for instrument description). Near simultaneous (i.e., within two hours) ground-based data were obtained for these flights, as summarized in Table 1. Note that full disk Helium and magnetic field scans take approximately 40 minutes each; times listed in the table are start times.

Table 1. Dates and Times of X-ray, He I and Magnetogram Data Used.

Date	X-ray (UT)	He I 10830	Magnetogram
6/27/74	1948	1605 1657 1804	1508 1854
9/16/76	1803	1841	1532
11/16/79	1703	1646	1543, 1743, 1828, 1917, 2007, 2100

We have performed the comparison as a double-blind experiment. Using these datasets we compared the XBP as marked by one of us (L.G.) against the He I dark points identified separately (by K. L. H.). The procedures for selecting x-ray bright points have been discussed in our earlier papers, but may be summarized briefly as follows: we examine the photographs for small, compact, isolated regions of x-ray emission. This may be pointlike, or give the appearance of elongated loop structure, or they may be fairly diffuse and best described as "cloudlike". The main criterion is that the region be self-contained and clearly isolated from any larger structure. The upper limit on size is arbitrarily taken

to be one arcminute.

Dark points were selected on the basis of a visual inspection of the He I λ10830 spectrohelioqrams using as criteria the size and intensity of isolated structures. Structures identified as dark points are typically less than 40 arcsec in extent, although some larger regions are included, particularly those in coronal holes, having an intensity at least 20% darker than the surrounding network. No attempt was made to eliminate filament fragments which can have a similar appearance. Consistency in the selection of features that are dark points depends strongly on the day-to-day variations of the calibration of the He I λ10830 data and the print quality.

The result of this comparison is best illustrated visually as in Figure 1. This figure shows the central portions of the He I and x-ray images obtained on 27 June 1974, and it illustrates the result which we find in general for all of the observations. There are four categories of correspondence between the two images. These are: He I dark points which *are* and *are not* associated with XBP, and XBP which *are* and *are not* associated with dark points.

In Figure 1 only three of these categories needed to be labelled since the last category was not present. That is, there were no XBP which did not have an associated He I feature. Thus, the figure contains three types of overlay symbols: a solid circle indicates an XBP located at the place where a He dark point was identified, a dotted circle indicates an XBP which did not have a *previously* identified He dark point, and a square indicates a helium feature which did not have an XBP.

The major conclusions reached from comparison of the x-ray and He I λ10830 data are:

1. There are, in general more XBP identified than there are He I dark points selected - 162 compared with 65;

2. Most of the dark points have corresponding XBP - 53 out of 64. In the few cases for which there is no XBP present, the helium feature tends to be a piece of filament material. Filaments appear as absorption features in He I λ10830, much as they do in Hα.

3. In essentially every case, an XBP can later be associated with a patch of He I absorption.

Results 1 and 2 are summarized quantitatively in Table 2.

Table 2. Statistics of Dark Point/Bright Point Identifications.

Date	# d.p.	# XBP	# d.p. w/o XBP	# XBP w/o d.p.
6/27/74	31	58	1	27
9/16/76	26	90	6	70
11/16/79	9	14	5	10

Explanation of column headings:

d.p. = number of He I dark points identified
XBP = number of x-ray bright points identified
d.p. w/o XBP = number of He I dark points which did not have corresponding x-ray bright points
XBP w/o d.p. = number of x-ray bright points which did not have *previously selected* dark points.

The key numbers in this table is listed in the last two columns. Our comparison shows that only ¼ to ½ of the x-ray bright points correspond to helium features which are identified on the basis of the He I data alone. It is, of course, quite possible that essentially all of the XBP correspond to helium features, which would be consistent with the small number of dark points without XBP, shown in the table's fourth column. However, the results of this study show that using present identification methods, ½ to ¾ of the x-ray bright points may not be located on the basis of the He I λ10830 data. On the other hand most He I dark points correspond to x-ray bright points, specifically the brighter ones (see Figure 1).

Although there are major differences apparent when comparing the two sets of small scale features, the statistical results should be viewed with caution because of two important considerations. As can be seen from Table 1, the datasets are not strictly simultaneous and it can be argued that the short lifetime and rapid variability of helium dark points and x-ray bright points may be partially responsible for the lack of correlation between the two maps. This may be particularly true for the

smaller, weaker x-ray bright points which, if they are not in the very early or very late stages of development, characteristically have shorter lifetime than the larger XBP (Golub *et al.* 1974).

The second point is that the selection criteria for x-ray bright points and helium dark points are somewhat subjective. Our analysis of the correlation between x-ray bright points and helium dark points is based on today's best effort. We do not rule out the possibility of empirically developing a reliable automated selection algorithm, perhaps in conjunction with magnetic field and H_α information.

3. Implications

On the basis of the assumed correlation between XBP and emerging magnetic flux certain major conclusions were reached: that the small regions contribute the majority of the emerging flux at nearly all phases of the Solar cycle (Davis, Golub and Krieger 1977), and that this would lead to an anticorrelation in the cycle behavior between the large (active regions as represented by sunspots) and the small (XBP) emerging regions (Golub, Davis and Krieger 1979; Davis 1983). By arguing that bright points are associated with small regions of emerging magnetic flux, Golub *et al.* 1979 put forward the suggestion that the Solar cycle is a variation in the size distribution of new emerging flux rather than a variation in the total quantity of flux.

Recent studies have greatly confused this proposed picture. In particular, time sequences of high resolution magnetograms show that many, if not most, of the observed small bipoles represent "chance encounters" of small opposite polarity magnetic elements which appear to come together and disappear (Martin *et al.* 1985). The work done by Harvey (1985) shows that two-thirds of the He I dark points are associated with chance encounters of opposite polarities, while the remaining one-third result from emerging new flux. If one were to assume that the He I dark points identify all of the XBP, instead of the fraction which we report here in Table 2, then we would conclude that chance encounters are mainly responsible for the XBP. The conclusions reached by Golub, Davis and Krieger (1979) would therefore be incorrect (Zwaan 1987).

Even though we have shown in this paper that there is a limit in finding from the ground-based data alone all of the XBP, this limit is largely irrelevant to the earlier bright point studies. The reason is that most of the earlier bright point studies were done using short x-ray exposures (Golub *et al.* 1977) in order to eliminate possible bias caused by the varying large scale coronal structures and coronal holes. Thus, the bright points studied were the largest and most easily seen, and those correspond quite well to the features selected in the Helium λ10830 data. The data used in the present study were taken with a different telescope than the one used on Skylab, but we attempted to chose exposure times which would produce images as close as possible to those used in the earlier work.

In Golub, Harvey and Webb (1986) we examined the relationship between XBP and ephemeral magnetic regions, using these same x-ray data and near-simultaneous magnetograms. Our conclusion was that the separation of the ER into encounters between opposite polarity network elements and emerging bipoles makes almost no difference in the probability of seeing an x-ray feature. Thus, if two-thirds of the magnetic features are chance encounter ("reconnection") events, then two-thirds of the x-ray features will by probabilities alone also be associated with reconnection events. The XBP which we studied would then be dominated by chance encounters and should have the same Solar cycle properties as the He I dark points.

The question remaining is why the XBP show an anticorrelation with the Solar cycle, as do the dark points (Harvey 1985), while the ER do not behave the same way. Unfortunately, we are not at this time in a position to answer this crucial question. A possible answer may be provided by noticing that the fractional area coverage of mixed polarity on the Sun is anticorrelated with the Solar cycle (Giovanelli 1979). The fraction of the Sun's surface covered by mixed polarity field tracks well with the variation in XBP number as a function of phase in the Solar cycle. However, Golub *et al.* (1977) established quite clearly that the size and lifetime of an XBP correlates well with the quantity of magnetic flux in the bipolar region. It is not clear whether area coverage of mixed polarities in itself is sufficient to explain the XBP variation, as Harvey (1985) argued, since field strength or quantity of flux in the region should also be a factor. For example, if at Solar minimum the mixed polarity field on the Sun consists of relatively small bits of magnetic flux, then the distribution of XBP lifetimes should be skewed toward short-lived regions. However, since the *Skylab* mission we have not had any time resolved x-ray data from which to determine changes in the XBP lifetime distribution as a function of Solar cycle. Moreover, it will be possible to make such a differentiation only if the distribution of lifetimes or fluxes for the emerging regions is different than that of the chance encounters.

The detailed comparisons between x-ray and magnetic data, with time resolved sequences of both, were done during the *Skylab* mission. At that time the magnetograph being used had lower spatial resolution and sensitivity than the present instrument. In the intervening fifteen years, no time sequences of high resolution x-ray data have been available. A step toward an answer may be pro-

vided by future flights of x-ray telescopes with higher spatial resolution, which could provide snapshots of the detailed structure within XBP, as well as time sequence observations to study the relation between XBP and the evolving underlying magnetl field. Such data may show a difference in topology between emerging and reconnecting features, which would at least help in determining whether there are differences in the coronal behavior of these two different kinds of magnetic regions. If we can successfully differentiate between the two types of region then one would expect that the two classes would have different Solar cycle properties, as determined by time-resolved data.

4. Acknowledgements

This work was supported as SAO by NASA Grant NAGW-112, at Emmanuel College by AFGL contract F19628-87-K-0033, and at A.S.&.E. by NASA Contract NAS5-25496.

5. References

Davis, J.M., L. Golub and A.S. Krieger 1977, *Ap. J.*, **214**, L141.

Davis, J. M. 1983, *Sol. Phys.*, **88**, 337.

Giovanelli, R. G., D. Hall and J. W. Harvey 1972, Solar Physics, **22**, 53.

Golub, L. 1980, *Phil. Trans. R. Soc. London A*, **297**, 595.

Golub, L., A.S. Krieger, J.W. Harvey and G.S. Vaiana 1977, *Sol. Phys.*, **53**, 111.

Golub, L., K. L. Harvey and D. F. Webb 1986, NASA CP-2442, ed. A. I. Poland, p.365.

Harvey, J. W. and D. Hall 1971, IAU Symp. **43**, 279.

Harvey, J. W., A. S. Krieger, A. F. Timothy and G. S. Vaiana 1975, in G. Righini (ed.), "Skylab Solar Workshop", Oss. e Mem. Osservatorio di Arcetri, **104**, 50.

Harvey, K. 1985, Australian J. Phys., **58**, 385.

Kahler, S. W., J. M. Davis and J. W. Harvey 1983, *Sol. Phys.*, **87**, 47.

Vaiana, G.S., A.S.Krieger and A.F. Timothy 1973, *Sol. Phys.*, **32**, 81.

Zwaan, C. 1987, *Ann. Rev. Astron. and Astroph.*, **25**, 83.

6. Figure Caption

Figure. 1. a) He I λ10830 spectrohellogram taken at 1657 UT (end at ~1740 UT) on 27 June 1974. Overlay indicates comparison with x-ray bright points, as follows: solid circle indicates He I dark point with corresponding XBP, dotted circle indicates location of XBP for which no He I feature was selected and squares indicate small pieces of filament material.

b) X-ray image obtained at 1948 UT on 27 June 1974.

Fig. 1a

Fig. 1b

Comments on the Observability of Coronal Variations

L. Golub[1], T. W. Hartquist[2] and A. C. Quillen[1,3]

1. Smithsonian Astrophysical Observatory, Cambridge Mass.

2. Max-Plank-Institut fur Physik und Astrophysik, D-8046 Garching

3. Astronomy Dept., Caltech, Pasadena Cal.

ABSTRACT

We discuss the observable variability of spectral lines in the soft x-ray and XUV region. Rapid variability of coronal emission, both in flaring and non-flaring structures has been reported and is particularly prominent when high spatial resolution is available. Examination of the ionization and recombination timescales for the formation and removal of ions with prominent Solar emission lines shows that variability timescales are often limited by these atomic processes, independent of the physical process which is causing the change in the Solar atmosphere. Rapid heating can lead to an initial freezing-in of abundances of some ions; observations of at least one low and one high excitation line from such an ion would permit studies of the time evolution of the emission measure and temperature. In some cases, rapid cooling leads to freezing-in of the abundance of an ion and observations of low excitation line of this ion will not yield accurate information about the thermal evolution. Thus, future observations of Mg X 609 Å should be augmented by simultaneous observation at another wavelength, such as 63 Å. In addition, with the ability to produce images in isolated spectral lines it becomes possible to select those for which rapid variability is observable, such as O VII, rather than lines which were selected on the basis of previous hardware constraints, such as O VIII.

Submitted to *Solar Physics*

1. Introduction

Techniques for the fabrication of thin film multilayer coatings capable of reflecting x-rays have progressed rapidly in recent years (for a review, see Barbee 1985). It has now become possible to design and construct astronomical instruments which employ multilayer coated optical elements and operate at normal incidence at wavelengths in the region from 44 to ~304 Å (Golub, *et al.* 1985, Underwood *et al.* 1987; Walker *et al.* 1988). With the development of normal incidence x-ray and XUV telescopes, high spatial (~0.1 arcsec) resolution observations of individual spectral lines emitted by the Solar coronal and transition region plasmas are now possible. Designs which include dispersive elements are also being developed, as are designs using multilayers at grazing angles permitting their use at shorter wavelengths (see the review by Catura and Golub 1988).

Because this new technology is available and is beginning to be used in Solar observations, the present time is opportune for addressing questions related to the observability of temporal variations in individual emission lines caused by the dynamical and physical evolution of the emitting regions. In the following, we will identify previously detected Solar emission lines which are suitable for the study of variability in plasmas with the specific combinations of pressure, temperature and spatial scales which are found in the Solar atmosphere, and then we will explore the types of variability which can be observed in each of these lines.

Rapid non-flare variability of coronal emission from individual loop structures seen in Fe XV at 284 Å was reported by Sheeley and Golub (1978). These data had 2 arcsec resolution, which permitted the individual loops in active regions to be resolved, whereas simultaneous observations in broadband x-rays, which had somewhat lower resolution, did not resolve these structures. Short time scale variability was not observed in x-rays and this lack of variability was interpreted as due to an averaging over the emission from several loops in the active region (Nolte, Solodyna and Gerassimenko 1979), which smooths out the variability of the individual structures.

These observations show that rapid variability does occur within active regions, and that spatial resolution of better than 2 arcseconds is needed for studies of these structures. However, our present study shows that the interpretation given by Nolte, *et al.* for the lack of variability in x-rays may not be correct. The x-ray emission which they observed was dominated by Fe XVII in the thin Be filter, or by a combination of Fe XVII, O VII and O VIII in the Polypropylene filter, with the latter possibly dominating. As we discuss in §3.3, the time scale for variability of the emission in O VIII at the temperature and density appropriate to typical coronal regions is several minutes. This is equal to or greater than the time scales observed in Fe XV, for which ionization equilibrium is established in a few tens of seconds.

Thus, the failure to observe variability in x-rays may have been an artifact of the instrumentation used, rather than anything intrinsic to the active region under study. Instruments which can provide imaging in a single spectral line are in some ways more susceptible to this problem, because an incorrect choice cannot be compensated by another line in the passband. For the study described above, the ability to choose O VII rather than O VIII would have provided diagnostics with 0.1 second time resolution.

Observations in more than one spectral line are needed in order to distinguish between temperature and density variations, since the emission from any single line by itself will yield information that mixes emission measure and temperature. For example, it is possible to observe temporal variability more rapid than the ionization times if the emission measure changes rapidly.

High spatial and moderate spectral resolution observations may reveal not only the variability of individual loop structures, but also the possible substructure within coronal loops. In coronal heating

models based on reconnection and current dissipation (e.g. Kuperus, Ionson and Spicer 1981), the primary heating is confined to very thin current sheaths which may heat the loops in either a steady or intermittent fashion. In either case, the loops should exhibit small scale thermal substructure with associated variability.

Martens *et al.* (1985) have reported observations of the corona using the HXIS instrument on the SMM satellite; their interpretation of the data is that "0.1% of the loop is filled with a plasma with a temperature of about 10^7 K and a density of 10^{11} cm^{-3}". The temperature and density in the remaining 99.9% of the loop volume are "much smaller". Observations such as these offer indirect evidence that loop substructure is present, and it is likely to be highly variable on short timescales.

The aim of this paper is to discuss the appropriateness of specific XUV and soft x-ray emission lines for studies of coronal variability. Among our major conclusions are the realization that, for many of the typical regions found in the Solar outer atmosphere, the observable timescales for variability are determined by the ionization and recombination timescales of the plasma rather than by the inherent nature of the physical process causing the variability. Moreover, we find that cases exist in which conductive cooling dominates and that in some of these cases the "freezing-in" of the ionization structure of a species affects the emissivity. If the particular lines being observed originates from a lowly excited level then the freezing-in will lead to the line's strength varying slowly compared to the cooling time. On the other hand, we show that diagnostics exist which can be used to determine whether or not conductive cooling is important in a particular event.

The organization of this paper is as follows: In section II we list the lines which are most likely to be used in future observations and describe their applicability in diagnostic studies of coronal emission under the variety of conditions encountered on the Sun. In section III we consider the ways in which the timescale for electron impact production of particular species affects the utility of those species for diagnosing changes in the coronal plasma; in the same section, we also treat cooling plasmas.

2. Selection of Lines

The x-ray and XUV emission lines which we have studied were selected on the basis of several criteria:

i) We chose the strongest lines in the Solar spectrum, based both on theoretical calculations and on observations which ensure that the line is actually present;

ii) We arbitrarily chose to limit our search to the range of wavelengths for which multilayer optics might be used. We take this range to be ~15 Å at the short end and 304 Å at the other end.

iii) Specific consideration was given to selecting those lines which would provide unambiguous diagnostics over the full range of temperatures from the chromosphere through flare levels (i.e. 10^4 to $10^{7.5}$ K).

The results of this search are not entirely satisfactory, in that the combination of technological difficulties and placement in the spectrum of the most interesting lines overlap in unfortunate ways. The results of the search can be summarized by the following three groupings:

I. 15-44 Å: This region contains the emission lines which for pure coronal imaging and diagnostics might be considered the most desireable, *viz.* Fe XVII, O VII, O VIII, C VI, etc. However, it does not seem possible at the present time to manufacture multilayers which work with any reasonable efficiency at normal incidence at these wavelengths. Grazing incidence (~ 10 - 20°) applications are possible, but these to some extent remove the enormous advantage in terms of spatial resolution which is achieved by going to normal incidence.

II. 44-170 Å: In this region production of high performance multilayers becomes feasible, especially longward of 60 Å. However, the coronal emission lines in this region are comparatively weak and construction of a practical observing instrument is difficult because of the low intensity levels.

III. 171 - 304 Å: Strong emission lines with important diagnostic value are found in this spectral region and high reflectivity multilayers are easily manufactured at these wavelengths. However, the spectrum is relatively crowded with strong emission lines and, because only a few layers are needed in order to achieve high reflectivity in the multilayer it is quite difficult to obtain a narrow band coating. Thus, the data will in general be contaminated by a mixture of different lines all imaged on top of each other. In principle this problem can be overcome by introducing a dispersive element into the optical system, or by very clever design of the multilayer; neither of these two solutions has yet been demonstrated in practice, however.

The lines which we have chosen are listed in Table I-a. Sources examined in the selection process include, among others: Freeman and Jones (1970), Manson (1972), Malinovsky and Heroux (1973), Doschek and Cowan (1984) and Acton, *et al.* (1985). The decision as to which lines will be most useful for coronal studies depends to a large extent upon the plasma conditions which are prevalent in the atmospheric feature (or event) of interest. There is no single best answer to this question, since typical features or events usually have a connection to the photosphere or below, thus encompassing temperatures from ~5000 K to 10^6 or as high as 10^8 K in extreme cases. However, a useful method of characterizing the study is to examine the coronal temperature, pressure and geometry, after which the lower temperature portions of the atmosphere are to some extent specified.

A simplified tabulation of typical plasma parameters is provided in Table I-b. It should be understood that these are only typical values, listed in order to show the general range observed. In the

following discussion we use this table as a starting point for an examination of the spectral lines which will be most useful for studying each of these coronal phenomena.

The Solar atmosphere is inherently complicated and atmospheric studies typically will require high resolution two-dimensional imaging and some type of spectroscopy. Structures with sizes ranging from the resolution limit (~ 200 km) to several Solar radii (>10^6 km) are seen and major changes in these structures occur on times scales from milliseconds during the rise phase of a flare (bursts), to tens of minutes for flares (gradual phase), to months for the evolution of the large scale structure. It is not likely that a single instrument can be designed which will diagnose the full range of conditions which are present on the Sun, and in fact the usual answer is to provide a complement of instruments which together form a Solar observatory.

The range of wavelengths over which multilayer coated optics can be used helps in deciding which subset of the overall problem will be attacked. In the "multilayer regime" the emission lines listed in table I-a cover a temperature range which includes the transition region and the corona, as well as thermal flare plasma. Thus our discussion centers around the type of problem typically treated by a grazing incidence x-ray telescope, with the addition of some of the lower temperature regions usually treated by an XUV or UV spectroheliograph, such as the S-082A instrument on *Skylab*. The spectral lines which are of interest for the regions or events listed in Table I-b are obtained from Table I-a by comparing the temperature, emission measure and variability timescales; results are listed in Table I-b in the last column.

3. Response of the Plasma to Rapid Heating or Cooling

3.1 General Principles

Shapiro and Moore (1977) and Shapiro and Knight (1978) have pointed out that the plasma properties in solar flare regions vary on timescales which are short relative to the timescales on which the ionization structure attains equilibrium. It is feasible to perform detailed calculations of the nonequilibrium ionization structure and emissivity for a small number of specific combinations of plasma conditions and thermal histories as did Shapiro and Moore (1977).

However, coronal events display a wide variety of properties and in practice more general considerations, of utility for the study of any given coronal plasma, are required. For instance, Shapiro and Knight (1978) discussed the initial increases in the strengths of high excitation lines (i.e., those for which the excitation energy is comparable to or higher than kT_0, where T_0 is the original temperature), and the subsequent decreases due to collisionally induced ionization. They argued that the observed enhancement of a single properly-chosen high excitation line can be used to determine the increase in temperature, while the subsequent decay of the line strength yields information about the density of the plasma. They envisaged the ionization remaining frozen-in initially with its preheating structure and the increase in a line's emissivity being due to the temperature increase; the contribution to the line strength's increase due to stripping of less ionized species was ignored. The subsequent decrease in the line's emissivity occurs at the density-dependent ionization rate.

In fact, a plasma in which both the density and temperature have grown rapidly can be studied best by comparing the temporal evolution of the strength of a high excitation line and a low excitation line. The increase in the strength of the low excitation line will be due primarily to the increase in the emission measure ($n_e^2 V$, where V is the volume) since the temperature dependence of an electron impact excitation rate generally is fairly weak when the energy of the impacting electron is much greater than the excitation energy. The increase of the strength of the high excitation line will result from both the rise in the emission measure and from the rise of the temperature, the latter usually leading to a rapid growth in the collisional excitation rate of a high excitation line.

In structures in which the conductive cooling is very strong, the cooling may also occur on a timescale which is short compared to that required for electron impact induced ionization to produce species which normally would be abundant in an equilibrium situation. The absence of emission features which would be prominent in an equilibrium plasma at its temperature maximum may lead one to underestimate the maximum temperature attained. Clearly, the variability of the plasma properties cannot be observed in lines of those species which cannot be ionized on timescales shorter than the evolutionary timescales of the plasma.

Simultaneous observations of a high excitation line and of a low excitation line are also useful for diagnostic studies of a plasma which is cooling rapidly. In plasma which is cooling due to rapid conductive heat loss, the ionization states may be frozen in with a structure similar to that which obtains in a high temperature equilibrium plasma. If freezing in does occur, low excitation lines emitted from highly ionized species will continue to be strong and would generally increase in strength as a function of time if the plasma pressure remains constant during the cooling phase. However, the strengths of the corresponding high excitation lines would decrease relatively rapidly with plasma temperature. From simultaneous measurements of a low excitation line and a high excitation line of frozen in highly ionized species, the temperature and emission measure evolutions could be derived. As a practical matter, it is preferable if the two lines are of the same ion, in order to keep the analysis as uncomplicated as possible.

An example of this effect is given in Figure 1, which compares the 52.9 Å emission of Fe XV to the 284 Å emission, using values taken from Mewe *et al.* (1985). The emissivity curves for the ion are identical, but dividing by the fractional abundance f for the respective lines in question introduces a major change, as shown by the upper curves in the figure. Thus, if material which is initially at a temperature of log T = 6.3 cools rapidly to a temperature of, e.g., log T = 6.0, then the decrease in strength of Fe XV at 284 Å can be as much as a factor of three less than that of the 52.9 Å line.

3.2 Variability Timescales for Line Emission

In section 2, we identified lines which have been detected previously and which are prime candidates for use in higher resolution studies of the corona. So that we can identify which lines are likely to be of diagnostic value, we have calculated the ionization and recombination timescales of various ions at different temperatures for plasma in which the pressure n_eT is arbitrarily taken to be equal to the value $3x10^{15}$ cm^{-3} K, where n_e and T are the electron density and temperature. Data for the calculation of these timescales come from the compilation by Arnaud and Rothenflug (1985) and references therein, primarily the papers of Woods, Shull and Sarazin (1981) and of Shull and van Steenburg (1982). In general, the time scales are inversely proportional to the pressure, but at high densities, dielectronic recombination may be suppressed.

The fraction, *f*, of an element that is in a given ionization stage in a low density equilibrium plasma can be found in the paper by Arnaud and Rothenflug (1985). For several species, we give *f* and various ionization and recombination timescales as a function of temperature in Table 2. In addition to several ions which are especially prominent in the Solar spectrum, the species C^{+5} and Fe^{+9} are included because they have lines which arise from states with very different excitation energies, making them useful as diagnostics when studying rapid heating events. The species Fe^{+17}, O^{+6} and Mg^{+9} are abundant in equilibrium plasmas over a wide range of temperatures and are observable in at least two types of Solar coronal regions (*viz.* Table 5).

We calculate timescales for four processes which can influence the appearance and disappearance of a line. The timescale, t_{if}, for the ionization of the next less ionized stage of an element and the timescale, t_{ir}, for the ionization to the next more ionized stage of that element are shown. t_{rr} is the timescale for the recombination to the next less highly ionized stage of the element and t_{rf} is the timescale for the recombination of the next more highly ionized stage of the element. This nomenclature is defined schematically in Figure 2. The timescales are normalized at $n_eT = 3x10^{15}$ cm^{-3}-K. The ionization timescale is equal to $(n_e [C_{ea}(T) + C_{di}(T)])^{-1}$ where C_{ea} is the autoionization excitation rate coefficiant (significantly large for the lithium like ion O+5 and for iron ions in the Sodium - Sulphur series) and C_{di} is the direct (electron impact) ionization rate coefficient. The recombination timescale is equal to $(n_e [\alpha_r(T) + \alpha_d(T)])^{-1}$ where α_r is the radiative recombination rate and α_d is the dielectronic recombination rate. Table 3 contains results extracted from Tables 2 for the temperature T_{max} at which a species attains its maximum abundance.

Normally the power emitted per unit volume in a single line by a plasma in equilibrium is written as the product of an emission rate coefficient, P_λ, and n_e^2. Note that even though in equilibrium plasmas the concentrations of species such as C^{+5} and Fe^{+9} may peak at the same temperature, the behavior of the line emissivities will differ greatly in response to rapid heating, as shown by the differences in the P_λ/f curves; this behavior during rapid heating was discussed at the beginning of §3.1. P_λ/f should be multiplied by the fraction of the element in the appropriate species to calculate the power in the line when the plasma is not in equilibrium.

Assume that we are interested in observing the emission from a species formed by the ionization of more lowly ionized species in a plasma which has been rapidly heated. The charge on the nucleus of that species is z and its ionization stage is ζ where $\zeta = 0$ for a neutral species and $\zeta = z$ for a fully ionized system. The number density is written $n_{z,\zeta}$. Because the ionization timescales increases rapidly with charge, it is normally sufficient to assume that a large fraction of an element is initially in the next lowest ionization stage when calculating the evolution of the population of a species. During the interval when $n_{z,\zeta}$ peaks, the system of equations

$$dn_{z,\zeta-1}/dt = -n_{z,\zeta-1}/t^*_{if} + n_{z,\zeta}/t^*_{rr}$$

$$dn_{z,\zeta}/dt = n_{z,\zeta-1}/t^*_{if} + n_{z,\zeta+1}/t^*_{rf} - (1/t^*_{ir} + 1/t^*_{rr})\, n_{z,\zeta}$$

$$n_{z,\zeta+1} = n_z - n_{z,\zeta} - n_{z,\zeta-1}$$

$$n_{z,\zeta-1}(t=0) = n_z$$

will govern the behavior of $n_{z,\zeta}$. The asterisks on t^*_{if}, t^*_{rf}, t^*_{ir}, and t^*_{rr} indicate that they should be evaluated by multiplying the results in Table 2 by (3×10^{15} cm^{-3}-K / n_eT). Values of P_λ/f can be used with the derived $n_{z,\zeta}$ to calculate the line strengths.

The abundance of a species $n_{z,\zeta}$ in a plasma which is heated can be approximated from the above equations if a few simplifying assumptions are made. We assume that initially $n_{z,\zeta-1} = n_z$, and that throughout the initial rise in $n_{z,\zeta}$ that $n_{z,1}$ can be set to 0. The question we ask is, if the plasma is heated instantaneously to a higher temperature, what is the timescale to form species z,ζ? Given these assumptions, one can show that

$$n_{z,\zeta} = (n_z\, \tau_{app} / t^*_{if})\,(1 - e^{-t/\tau_{app}})$$

with

$$\tau_{app} = (t_{if}^{-1} + t_{ir}^{-1} + t_{rr}^{-1})^{-1}$$

Values of this quantity for the species which we considered are given in Table 3.

The abundance of a particular species in a recombining plasma cannot always be followed with such a small set of equations, because the recombination time scale is not a strongly monotonically decreasing function of ζ. At log T = 6.5 the values of t_{rr} for Fe^{+23}, Fe^{+21}, Fe^{+11}, and Fe^{+8} are 43.4s, 27.8s, 14.5s, and 21.8s respectively. Hence, in a plasma which has cooled very rapidly, the recombination eventually leads to significant populations in a range of ionization stages. However, in many cases it is sufficient to compare the recombination timescales to the cooling timescales to determine at what temperature the ionization structure is last in statistical equilibrium. As long as the recombination continues to occur on a timescale long compared to either the cooling timescale or the timescale since rapid cooling has stopped, the ionization structure can be assumed to be that which obtains in an equilibrium plasma at the temperature at which cooling first becomes more rapid than recombination.

The set of equations given above should be sufficient to follow the abundance of a species z,ζ in a cooling plasma under certain restricted conditions. For instance, if a plasma is cooling from an equilibrium at which $n_{z,\zeta} >> n_{z,\zeta+i}$ for all i>2, the three equations should give a reasonable description of the evolution of $n_{z,\zeta}$. Clearly, the initial values of $n_{z,\zeta-1}$, $n_{z,\zeta}$ and $n_{z,1}$ should be specified to be those for a plasma in equilibrium at the initial temperature.

We have given in Table 4 the timescales for cooling due to radiative losses in equilibrium plasma in which $n_eT = 3\times10^{15}$ cm^{-3}-K initially; these timescales are appropriate for a plasma cooling isochorically and were obtained by using data given in a figure produced by R. Edgar with J. Raymond's code and provided by J. Raymond, showing the power loss coefficient as a function of temperature. The

cooling timescale for isobaric cooling is obtained by multiplying the results given in Table 4 by 5/3.

The timescale for conductive cooling may be calculated by considering a loop of half-length l in which radiative losses are balanced exactly by heating and which is cooling isochorically due to conduction. Several approximate solutions have been calculated for this case; Krall has suggested that the temperature, T_o, at the apex of the loop evolves as

$$T_o = T_\infty \left(1 + \frac{1.4X10^9 \, T_{oo}^{5/2}}{n \, l^2} \right)^{-2/5}$$

where T_{oo} is the initial temperature at the apex of the loop.

In calculating the conductive cooling time we will use Krall's result. However, we note that the equation of thermal balance is a partial differential equation with time and spatial derivatives; if one assumes that conductivity is the only process responsible for energy loss or gain, that flows are very subsonic, that the loop is a cylinder in which conductive heat transfer is parallel to the axis of symmetry, and that the gas cools either isobarically or isochorically, then the equations can be solved by a separation of variables. No solution exists for a cooling loop with T = 0 at the base and T a maximum at the top. Consequently, any value for the conductive cooling time which one may adopt is somewhat arbitrary and is likely to be corret only to within an order of magnitude of the true value.

3.3 Emission From Solar Coronal Features

We have given in Table 5 typical timescales for the appearance and disappearance of lines prominent in the spectra of the coronal features listed in Table Ib, using the temperature and density values appropriate to the different types of regions under consideration. The timescales given take into account the number, $n_{z,\zeta}$ of atoms contributing to the emission and are calculated in several steps. $\tau_{app.}$, the minimum time for the appearance of the line, is the ionization time for formation of ~60% (one e-folding) of the ion from the next less ionized state of the element, calculated assuming the temperature instantaneously becomes the maximum temperature for emission of the line. These times were calculated from the times listed in Table 3 using the temperatures and pressures typically found in the coronal features emitting the line. $\tau_{recom.}$ is a lower limit on the disappearance time of the line. It is the time for 60% of the ion to recombine to the next less ionized state at the temperature and pressure found in the coronal feature.

For comparison also given is $\tau_{dis.,cond.}$, the disappearance timescale of the line assuming that conductive cooling is the dominant cooling mechanism, and $\tau_{dis.,rad.}$, the disappearance timescale of the line assuming that radiative cooling is the dominant cooling mechanism. These are the times for the emissivity of the line to drop to 1/e of its maximum value. Conductive cooling rates were calculated assuming constant heat flux throughout the loops (Krall 1977). Radiative cooling rates were calculated using analytic fits to Raymond's power loss function (*viz.* Rosner, Tucker and Vaiana 1978).

$\tau_{dis.,cond.}$ and $\tau_{dis.,rad.}$ were calculated assuming ionization equilibrium. In these cases, it is necessary to consider not only the timescale for a given change in temperature which is given directly from the cooling curves, but also to consider the change in emission which occcurs for a given change in temperature. In this way, the timescales given in Table 5 for disappearance of a line refer to the same quantities listed for appearance of the line.

The cooling timescale due to radiative losses is inversely proportional to the pressure, in optically thin plasmas. For the high temperature plasmas encountered in active regions and flares in the Solar corona, the pressures are usually very much higher than the value of 3×10^{15} which we have used as a normalization. Thus radiative cooling times for flares are typically 10^2 to 10^3 seconds and are comparable to the typical conductive cooling times calculated for flare loops. We wish to point out only that conductive cooling may in some cases be more important than radiative cooling in the coronal plasma. As discussed above, freezing-in can occur when the cooling is very rapid, and in those cases simultaneous observations of properly chosen high and low excitation lines should be used in order to diagnose both the emission measure and the temperature variations.

3.4 The Case of Mg X

Of the lines listed in Table 5, the only one for which freezing-in might occur under coronal conditions is Mg X emitted by large scale coronal structures. However, as pointed out in §3.3, the correct values for conductive cooling times are uncertain by a large factor and conductive cooling might be important in a wider variety of situations in the Solar atmosphere; the opposite may also be true. Under the assumption that there will turn out to be cases for which we need to consider rapid cooling we give a treatment which is of general validity for a gas which has just begun to cool isochorically.

The total power emitted in a line in a cooling plasma is given by

$$E_\lambda(z,\zeta) = P_\lambda(z,\zeta)\, X(z,\zeta)\, (n_e^2 V)$$

where $P_\lambda(z,\zeta)$ is the line power rate coefficient, V is the volume of the emitting gas, λ is the wavelength, and

$$X(z,\zeta) \equiv n_{z,\zeta}/n_e$$

In general, the mass of gas will remain constant as it cools, i.e., $n_e V$ remains constant. We restrict consideration to rapid cooling so that n_e remains constant; this is equivalent to requiring that the sound crossing time in the loop is long compared to the cooling time. The timescale on which the line strength varies is then given by

$$t_{dis} = \left(P_\lambda^{-1} \frac{dP_\lambda}{dT}\, dT/dt + X^{-1}\, dX/dt \right)^{-1}$$

A reasonable estimate for t_{dis} is obtained by replacing dT/dt with

$$(T/t_{rad} + T/t_{cond})$$

and $X^{-1}\, dX/dt$ with the minimum of

$$\left[\frac{1}{X_{eq}(z,\zeta)} \frac{dX_{eq}(z,\zeta)}{dT} \left(\frac{T}{t_{rad,cool}} + \frac{T}{t_{cond,cool}} \right) , \frac{1}{t_{rr}^*} \right]$$

where X_{eq} is given from equilibrium calculations.

The data necessary to calculate t_{dis} for Mg X are given in Table 2 and Table 4, and by the equation for the conductive cooling time. If the Mg^{+9} abundance freezes-in then observations of Mg X at, for example, both 63 Å and 609 Å will permit a determination of the temperature over a broader range than if the Mg^{+9} attained its equilibrium value. This also means that the timescale for disappearance of the Mg X emission can be significantly larger than that of another ion formed at a similar temperature. Under conditions of rapid cooling (which presumably alternate with periods of heating) the 609 Å line will show less variability than will the 63 Å line. Measurement of both lines permits an accurate temperature determination, and measurement of a line of a species which attains equilibrium abundance rapidly (such as O VII) can be used to determine the emission measure and thence n_e.

4. Summary

With a view toward observations of the Solar transition region and corona using imaging of individual spectral lines in the soft x-ray and XUV portion of the spectrum, we have discussed some of the major factors which enter into the choice of spectral line to be used. The discussion has centered around the lines which are available to the technology of multilayer coatings, but is more general in its range of applicability. Because of our interest in coronal heating and the rapid variability of coronal structures we have concentrated on the observability of variations in line strength for the range of features found in the Solar corona. Examination of the ionization and recombination timescales for the formation and removal of ions which are prominent in the coronal spectrum shows that variability timescales are often limited by these atomic processes, independent of the physical process which might be assumed to be causing the changes.

In some situations, the plasma may be heated on timescales which are short compared to the time needed for the ionization structure to attain equilibrium. Such rapid heating can lead to a freezing-in of the initial ionization structure. In such cases, comparison of a low excitation line of a species to a high excitation line (preferably of the same species) would permit accurate determination of the time evolution of both the emission measure and the temperature. Similarly, there are some situations in which rapid cooling may lead to a freezing-in of the abundance of an ion. In particular, Mg X viewed in large scale coronal structures should show this effect. Observations in the 609 Å line of Mg X should be supplemented by the short wavelength line such as Mg X at 63 Å.

Studies of rapid variability in active regions should be performed with spectral lines which are capable of being formed on short timescales. For example, at typical active region temperatures of 2-3X10^6 K, the species O VII can appear on times a factor 100 shorter than those for the appearance of O VIII. Disappearance times for O VII are about one order of magnitude shorter than those for O VIII.

This work was supported by NASA Grant NAGW-112 to the Smithsonian Institution and by the Smithsonian Institution Visitors' Program. We would like to thank Dr. John Raymond for helpful discussions during preparation of this manuscript.

5. References

Acton, L. W., M. E. Bruner and W. A. Brown 1985, *Ap. J.*, **291**, 865.

Arnaud, M. and R. Rothenflug 1985, *Astron. Astrophys. Suppl. Ser.*, **60**, 425.

Barbee, T. W. 1985, SPIE Proc. **563**, 2.

Catura, R. C. and L. Golub 1988, *Rev. de Physique Appl.*, , .

Doschek, G. A. and R. D. Cowan 1984, *Ap. J. Suppl. Ser.*, **56**, 67.

Freeman, F. F. and B. B. Jones 1970, *Sol. Phys.*, **15**, 288.

Golub, L., G. Nystrom, E. Spiller and J. Wilczynski 1985, SPIE Proc. **563**, 266.

Krall, K. R. 1977, *Sol. Phys.*, **55**, 455.

Kuperus, M., J. A. Ionson and D. S. Spicer 1981, *Ann. Rev. Astron. and Astroph.*, **19**, 7.

Malinovsky, M. and L. Heroux 1973, *Ap. J.*, **181**, 1009.

Manson, J. E. 1972, *Sol. Phys.*, **27**, 107.

Martens, P. C. H., G. H. J. van den Oord and P. Hoyng 1985, *Sol. Phys.*, **96**, 253.

Mewe, R., E. H. B. M. Gronenschild and G. H. J. van den Oord 1985, *Astron. Astrophys. Suppl. Ser.*, **62**, 197.

Nolte, J. T., C. V. Solodyna and M. Gerassimenko 1979, *Sol. Phys.*, **63**, 113.

Rosner, R., W. H. Tucker and G. S. Vaiana 1978, *Ap. J.*, **220**, 643.

Shapiro, P. R. and J. W. Knight 1978, *Ap. J.*, **224**, 1028.

Shapiro, P. R. and R. T. Moore 1977, *Ap. J.*, **217**, 621.

Sheeley, N. R., Jr. and L. Golub 1979, *Sol. Phys.*, **63**, 119.

Shull, J. M. and M. Van Steenberg 1982, *Ap. J. Suppl. Ser.* **48**, 95.

Stern, R., Wang, E., Bowyer, S. 1978, *Ap. J. Supp. Ser.*, **37**, 195.

Underwood, J. H., M. E. Bruner, B. M. Haisch, W. A. Brown and L. W. Acton 1987, *Science*. **238**. 61.

Walker, A. B. C., J. Lindblom, R. B. Hoover and T. W. Barbee 1988, Proc. IAU Colloq. No. 102 (in press).

Woods, D. T., J. M. Shull and C. L. Sarazin 1981, *Ap. J.*, **249**, 399.

6. Figure Captions

Figure 1. Comparison of the emissivity of a low and high excitation line of the species Fe^{+14}. The upper curves show the emissivity divided by the fractional abundance for each line.

Figure 2. Schematic illustration of the nomenclature used for labelling the formation and removal processes of species *i*.

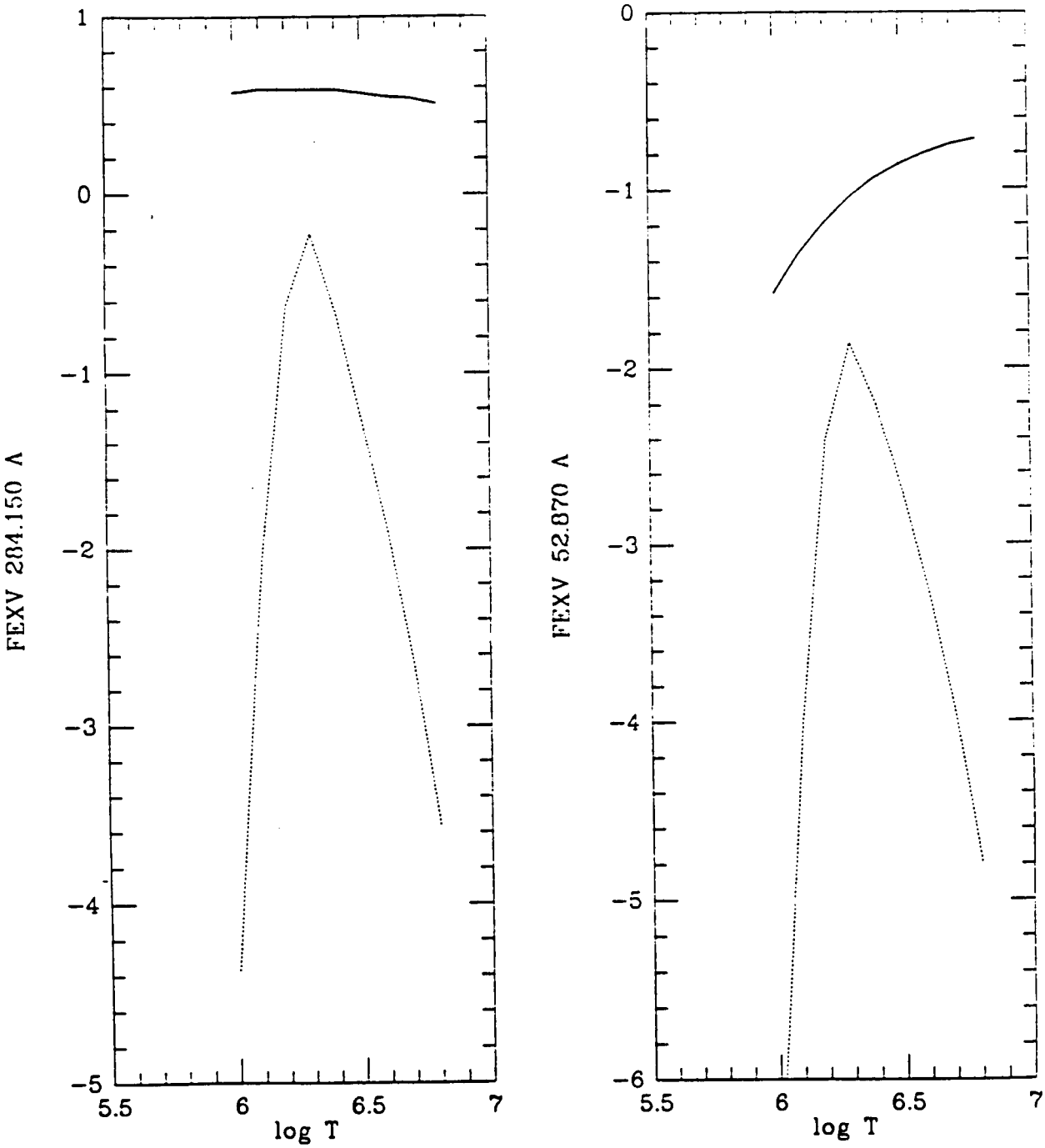
FEXV 284.150 Å
1
0
-1
-2
-3
-4
-5
5.5
6
6.5
7
log T
FEXV 52.870 Å
0
-1
-2
-3
-4
-5
-6
5.5
6
6.5
7
log T

Fig. 1

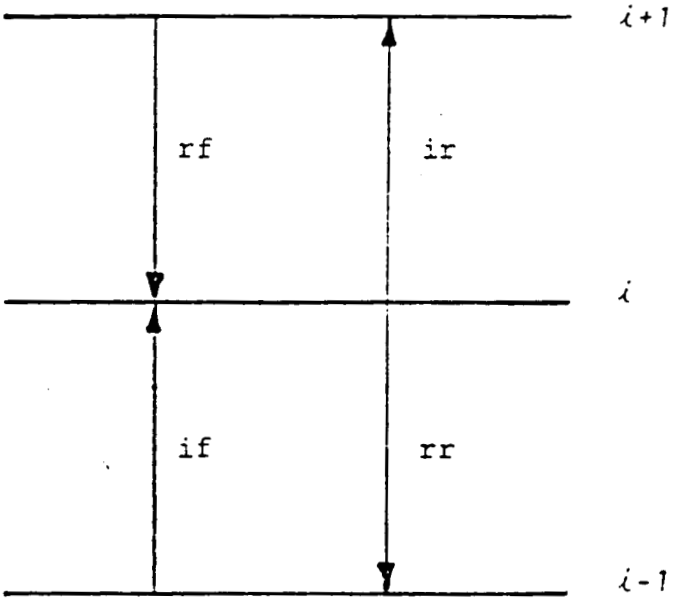

Fig. 2

Table I-a. Soft X-ray and XUV Lines Included in This Study

Species	Wavelength (Å)	$\log(T_{max})$
Fe XVII	16.78	6.6
	17.05	
	17.10	
O VIII	18.97	6.5
O VII	21.60	6.3
	21.81	
	22.10	
C VI	33.74	6.1
Si XII	45.52	6.3
	45.68	
Si XI	49.22	6.2
Mg X	57.9	6.1
Si VIII	61.0	6.0
Fe XVI	62.88	6.4
	63.71	
Mg X	63.15	6.1
	63.29	
Ne VIII	88.08	5.8
Fe XVIII	93.93	6.8
Ne VIII	98.26	5.8
Ne VII	115.52	5.7
	116.69	
Fe XXII	116.29	7.1
	117.17	
Fe IX	171.07	6.0
O V	172.17	5.4
O VI	172.94	5.5
	173.08	
Fe X	174.53	6.1
	177.24	
Fe XI	180.41	6.2
	182.17	
	188.22	
O VI	183.95	5.5
	184.13	
Fe XXIV	192.03	7.3
Fe XII	192.40	6.2
	193.52	
	195.13	
Fe XIV	211.32	6.2
	274.24	
He II	256.37	4.6
Fe XV	284.16	6.3
He II	303.79	4.6
Si XI	303.33	6.2

Table I-b. Typical Plasma Parameters for Solar Atmospheric Features

Target	Size [$x10^9$cm]	N_e [cm^{-3}]	T [10^6 K]	Lines
Quiet Corona	20	$1\text{-}3x10^8$	1.6	O VII, C VI, Mg X, Fe XI, Fe XII
Extended Corona	70	10^7	1.4	Fe X, Mg X, Ne VII
Polar Plumes	50	10^8	1.3	Mg X, Fe X, Ne VIII
Active Region	5-20	10^9-10^{10}	2-3	O VIII, Fe XVII, Fe XVI, Fe XV
Loop Microstructure	<1	10^{11}	10	Fe XVIII, Fe XXII, Fe XXIV
X-ray Bright Point	.2-2	$5x10^9$	1.8	O VII, Si XII, Fe XIV
Compact Flare	2-3	10^{11}	20	Fe XXII, Fe XXIV
Two-Ribbon Flare	10	$2x10^{10}$	10	Fe XVIII, Fe XXII, He II

Table 2. Ionization and Recombination Timescales as a Function of Temperature

log T	t_{if}	t_{ir}	t_{rr}	t_{rf}	-log *f*
		C VI			
5.7	7.8e3	2.1e5	1.6e2	86	1.7
5.8	1.4e3	2.4e4	2.2e2	1.3e2	0.9
5.9	3.5e2	4.2e3	2.6e2	1.9e2	0.4
6.0	1.2e2	1.1e3	2.7e2	2.9e2	0.2
6.1	56	4.0e2	2.7e2	4.3e2	0.4
6.2	31	1.8e2	2.8e2	6.5e2	0.7
6.3	20	1.0e2	3.1e2	9.9e2	1.0
6.4	15	65	3.7e2	1.5e3	1.4
6.5	12	48	4.7e2	2.3e3	1.7
		Fe IX			
5.6	95	69	0.76	0.37	2.2
5.7	4.0	19	0.89	0.51	1.3
5.8	2.0	7.2	1.1	0.70	0.8
5.9	1.2	3.4	1.5	0.96	0.5
6.0	0.79	2.0	2.2	1.4	0.5
6.1	0.60	1.3	3.3	2.0	0.9
6.2	0.50	0.99	5.1	2.9	1.8
6.3	0.45	0.82	8.1	4.5	3.5
		Fe XVIII			
6.3	5.5e3	1.2e4	1.1e2	41	2.5
6.4	1.4e3	2.8e3	1.3e2	59	1.5
6.5	4.8e2	8.9e2	1.5e2	82	0.9
6.6	2.2e2	3.7e2	1.7e2	1.1e2	0.5
6.7	1.2e2	1.9e2	2.1e2	1.5e2	0.4
6.8	77	1.2e2	2.8e2	2.0e2	0.6
6.9	57	85	3.9e2	2.8e2	1.0
7.0	47	68	5.7e2	4.1e2	1.8
7.1	42	59	8.6e2	6.1e2	3.0
		Mg X			
5.8	2.7e2	1.3e3	13	58	3.0
5.9	90	3.7e2	21	88	1.5
6.0	39	1.4e2	34	1.3e2	0.7
6.1	21	70	56	2.0e2	0.7
6.2	13	41	92	3.1e2	0.9
6.3	9.6	28	1.5e2	4.6e2	1.2
6.4	7.8	22	2.5e2	6.3e2	1.5
6.5	6.8	18	4.1e2	7.8e2	1.7
6.6	6.5	17	6.7e2	9.0e2	1.8
6.7	6.5	16	1.1e3	1.0e3	1.9
6.8	6.9	17	1.8e3	1.2e3	2.2

O VII

5.3	5.6e-2	-	28	11	2.8
5.4	6.5e-2	-	42	17	1.1
5.5	7.7e-2	-	63	26	0.2
5.6	9.2e-2	6.e9	94	40	0.1
5.7	0.11	8.e7	1.4e2	61	0.0
5.8	0.14	2.7e6	2.1e2	93	0.0
5.9	0.16	1.8e5	3.0e2	1.4e2	0.0
6.0	0.20	2.3e4	4.0e2	2.0e2	0.0
6.1	0.24	4.5e3	4.4e2	2.7e2	0.0
6.2	0.29	1.3e3	4.3e2	3.3e2	0.1
6.3	0.36	4.8e2	4.2e2	3.9e2	0.3
6.4	0.44	2.3e2	4.4e2	4.6e2	0.6
6.5	0.54	1.3e2	5.0e2	5.7e2	1.1
6.6	0.68	88	6.2e2	7.4e2	1.7

O VIII

5.9	1.8e5	3.2e6	1.4e2	94	3.1
6.0	2.3e4	2.6e5	2.0e2	1.4e2	2.1
6.1	4.5e3	3.9e4	2.7e2	2.1e2	1.3
6.2	1.3e3	8.6e3	3.3e2	3.1e2	0.7
6.3	4.8e2	2.7e3	3.9e2	4.7e2	0.4
6.4	2.3e2	1.1e3	4.6e2	7.1e2	0.3
6.5	1.3e2	5.5e2	5.7e2	1.1e3	0.5
6.6	88	3.3e2	7.4e2	1.6e3	0.8
6.7	66	2.3e2	1.0e3	2.5e3	1.1
6.8	54	1.8e2	1.4e3	3.8e3	1.3
6.9	49	1.5e2	2.1e3	5.8e3	1.6
7.0	47	1.4e2	3.2e3	8.9e3	1.8
7.1	48	1.4e2	5.0e3	1.4e4	2.0
7.2	50	1.4e2	7.9e3	2.1e4	2.2
7.3	55	1.5e2	1.3e4	3.3e4	2.3

Table 3. Ionization and Recombination Timescales* for Selected Lines

Ion	$\log(T_{max})$	-log(f)	t_{if}(sec)	t_{ir}(sec)	t_{rr}(sec)	t_{rf}(sec)	τ_{app}
C^{+5}	6.0	0.2	120	1.1e3	290	270	65
Fe^{+23}	7.2	0.5	590	1.4e3	890	1.0e3	206
Fe^{+21}	7.0	0.7	260	460	220	200	75
Fe^{+17}	6.7	0.4	120	190	150	210	51
Fe^{+16}	6.4	0.1	23	1.4e3	130	21	10
Fe^{+15}	6.3	0.9	16	40	13	9.9	4.2
Fe^{+14}	6.3	0.8	9.0	16	9.9	7.0	2.8
Fe^{+13}	6.2	0.8	8.3	15	4.3	5.8	1.9
Fe^{+11}	6.2	0.6	2.4	4.6	3.9	3.9	1.1
Fe^{+10}	6.1	0.6	2.2	3.7	2.6	2.4	0.80
Fe^{+9}	6.0	0.6	2.0	3.5	1.6	1.4	0.54
Fe^{+8}	6.0	0.5	0.8	2.0	1.3	2.2	0.40
Mg^{+9}	6.1	0.7	21	69	200	56	14
Ne^{+7}	5.8	0.6	13	56	100	18	7.0
Ne^{+6}	5.7	0.5	4.0	29	11	3.3	1.6
O^{+7}	6.4	0.3	230	1.1e3	710	460	103
O^{+6}	6.3	0.3	0.4	480	390	420	0.4
O^{+5}	5.5	0.6	4.1	0.08	63	5.8	2.3
O^{+4}	5.4	0.3	0.8	10	3.7	1.1	0.4
Si^{+11}	6.3	0.6	42	130	290	95	26
Si^{+10}	6.2	0.6	21	74	60	18	8.3
Si^{+7}	5.9	0.3	4.9	19	7.8	10	2.3

*) At the temperature of maximum emission.

Table 4. Radiative Cooling Timescales for an Equilibrium Plasma

log T	$t_{cool.}$(sec)	n_e*	log T	$t_{cool.}$(scc)	n_e*
4.8	0.87	5.0e10	6.1	690	2.4e9
4.9	0.97	4.0e10	6.2	970	1.9e9
5.0	1.5	3.0e10	6.3	2.2e3	1.5e9
5.1	3.9	2.4e10	6.4	5.5e3	1.2e9
5.2	5.5	1.9e10	6.5	1.4e4	1.0e9
5.3	7.7	1.5e10	6.6	1.9e4	8.0e8
5.4	11	1.2e10	6.7	3.1e4	6.0e8
5.5	27	1.0e10	6.8	4.9e4	5.0e8
5.6	69	8.0e9	6.9	7.8e4	4.0e8
5.7	140	6.0e9	7.0	1.1e5	3.0e8
5.8	220	5.0e9	7.1	2.2e5	2.4e8
5.9	340	4.0e9	7.2	4.4e5	1.9e8
6.0	490	3.0e9	7.3	8.5e5	1.5e8

*) Assuming Solar abundances and $n_eT = 3x10^{15}$ cm^{-3} K. Cooling is assumed to occur isochorically; timescales for isobaric cooling are obtained by multiplying these values by 5/3. See text for further discussion.

Table 5. Heating and Cooling Timescales* for Solar Coronal Features.

Feature	Line	$\tau_{app.}$	$\tau_{recom.}$	$\tau_{dis.\ cond.}$	$\tau_{dis.\ rad.}$
Quiet Corona	O VII	3.0	$3x10^3$	$5x10^4$	10^4
Extended Corona	Fe X	120	500	$2x10^4$	$1.5x10^5$
	Mg X	2000	$4x10^4$	$2x10^4$	$1.5x10^5$
Polar Plumes	Fe X	12	50	10^5	$1.4x10^4$
	Mg X	370	$4.5x10^3$	10^5	$1.4x10^4$
Active Region	O VIII	28	200	$8x10^4$	10^3
	Fe XVII	4.0	30	10^5	10^3
Microstructure	Fe XVIII	1.0	1.2	600	600
	Fe XXII	3.0	0.7	250	400
X-ray Bright Point	O VII	0.1	100	800	500
Compact Flare	Fe XXII	3.0	1.3	400	10^3
	Fe XXIV	10	2	750	$2x10^3$
Two-Ribbon Flare	Fe XVIII	5.0	6	10^4	$3x10^3$
	Fe XXII	15	3	$5x10^3$	$2x10^3$

*) Using T and n_e values from Table I-b. All times are in seconds.

SPOT TEMPERATURES AND AREA COVERAGES ON ACTIVE DWARF STARS

Steven H. Saar[1] and James E. Neff[2]

[1]Harvard-Smithsonian Center for Astrophysics
[2]NASA Goddard Space Flight Center

ABSTRACT

We use spectra of the 7100 and 8860 Å bands of TiO to estimate the temperature and projected area of cool spots on two active K dwarf stars: HD 82558 and the flare star BD +26°730.

OBSERVATIONS AND ANALYSIS

The TiO bands are sensitive indicators of temperature in stellar atmospheres. The very presence of these features in dwarf stars with $T_{eff} \geq 4250$ K (≈K5V) is direct evidence for cool spots. Ramsey and Nations (1980) first used the 8860 Å TiO band to detect spots on HR 1099. Following their success, work has concentrated on RS CVn stars (Huenemoerder and Ramsey 1987; Huenemoerder 1988). In this paper we discuss the extension of this technique to measurements of the spot characteristics on active *dwarf* stars.

We obtained spectra of the TiO region using the the National Solar Observatory's McMath Solar telescope and the stellar spectrograph system described by Smith and Jaksha (1984). Using the Bausch and Lomb grating in first order and the 105 mm transfer lens, the 2 pixel resolution on the TI CCD detector was $\lambda/\Delta\lambda$=13,000. Signal-to-noise ratios were typically 100 to 300.

The two wavelength regions we selected, 7100 and 8860 Å, contain TiO absorption bands with various temperature sensitivities. The 7100 Å bands (at 7055, 7088, and 7126 Å; the γ (0,0) system) first become visible for an immaculate star at spectral type about K5, while the 8860 Å band (the δ (0,0) system) is not evident until M1. Modeling the two bands simultaneously, therefore, permits an estimate of both the size (from the absolute band strengths) and the temperature (from the ratio of the band strengths) of cool spots on the stellar surface. Our approach is essentially a simplified version of the one used by Huenemoerder and Ramsey (1987), in which the normalized spectrum from a spotted star (F_{total}) is modeled as the weighted sum of F_{spot} and F_{phot}, the normalized spectra of suitable standard stars with the effective temperature of the spot and the photosphere, respectively. The model is given by

$$F_{total} = \frac{AR_\lambda F_{spot} + (1-A)F_{phot}}{AR_\lambda + (1-A)},$$

where A is the total fractional projected area of spots on the observed hemisphere (weighted by limb-darkening) and R_λ is the surface flux ratio between the spots and the photosphere. We assumed that R_λ can be represented by the ratio of the respective Planck functions: i.e., $R_\lambda = B_\lambda(T_{spot})/B_\lambda(T_{phot})$. We performed simultaneous least squares fits in both wavelength regions to the above equation. Various standard star spectra were used to simulate F_{spot} and F_{phot} until the best fit was achieved. Values of T_{eff} for the standard stars were taken from de Jager and Nieuwenhuijzen (1987).

RESULTS AND DISCUSSION

In this preliminary study, we have focussed on two dwarf stars: BD +26°730 (=Gliese 171.2A; K5Ve, B–V=1.12) and HD 82558 (K2Ve, B–V=0.91). We used the spectrum of ξ Boo B (K4V, B–V=1.16) as the model immaculate photosphere for BD +26°730 and the spectrum of HD 149661 (=12 Oph; K1V, B–V=0.82) for the immaculate photosphere of HD 82558. A sequence of models were then generated for each star, using M giant spectra of varying T_{eff} to simulate spot spectra (the TiO bands are insensitive to gravity; Wing, Dean, and MacConnell 1976).

Excess absorption in the TiO bands is clearly present in the spectrum of BD +26°730 (Fig. 1). The best fit to both bands was obtained using 2 Cen (M4.5III) to simulate the cool spot spectrum. With T_{phot}=4250 K, we find T_{spot}=3500 ± 150 K, $\Delta T \equiv T_{phot}-T_{spot}$=750 ± 150 K and $A = 0.20 \pm 0.04$.

The 7100 Å band of HD 82558 is somewhat weaker than that of BD +26°730 (Fig. 2a), while the 8860 Å band does not appear to be present (Fig. 2b) at all, indicating that the spots on HD 82558 must be warmer than those on BD +26°730. We found that μ Gem (M3III) was the coolest star whose spectrum we could use as F_{spot} and still fit the HD 82558 data. With T_{phot} = 4900 K, we derive $T_{spot} \geq$ 3700 K, $\Delta T \leq$ 1200 K, and $A \geq$0.22.

BD +26°730 (Bopp *et al.* 1983) and HD 82558 (Fekel *et al.* 1986) are among the most chromospherically active K dwarfs known. Both have rotational periods of less than 2 days. BD +26°730 exhibits flare activity, which is unusual for K dwarfs, and shows large, long-term luminosity changes, probably arising from a stellar activity cycle (Hartmann *et al.* 1981). The derived area coverages are similar to those found on the most active BY Dra and RS CVn variables (e.g., Poe and Eaton 1985; Rodonò *et al.* 1986; Huenemoerder 1988). The derived temperature differences between spot and photosphere fall in the range seen for other BY Dra variables (e.g., ΔT = 600 K for BY Dra, Vogt 1983; ΔT = 850 K for AU Mic, Rodonò *et al.* 1986).

Spectroscopic determinations of spot properties measure ***absolute*** spot parameters, unlike photometric methods, which are differential in nature. We are continuing TiO observations, both in an effort to survey the spot properties of flare stars and to search for rotational modulation. Analysis of the latter will allow us to partly remove the geometric ambiguities in the interpretation of A and determine actual positions and sizes of the dominant starspots. With the survey results, we can explore (among other things) whether the increased area covered by starspots could explain the greater number and strength of stellar flares relative to the Sun.

This work is based on data obtained at the National Solar Observatory (NSO), which is operated by AURA, Inc. under contract with the NSF. The research is supported by the Smithsonian Institution Fellowship Program, NASA grant NAGW-112, and a fellowship from the National Research Council. Finally, we thank the NSO for granting us observing time and travel support, and for their hospitality.

REFERENCES

Bopp, B. W., Africano, J. L., Stencel, R. E., Noah, P. V., and Klimke, A. 1983, *Ap. J.*, **275**, 691.
De Jager, C., and Nieuwenhuijzen, H. 1987, *Astr. Ap.*, **177**, 217.
Fekel, F. C., Bopp, B. W., Africano, J. L., Goodrich, B. D., Palmer, L. H., Quigley, R., and Simon, T. 1986, *A. J.*, **92**, 1150.
Hartmann, L., Bopp, B. W., Dussalt, M., Noah, P. V., and Klimke, A. 1981, *Ap. J.*, **249**, 662.
Huenemoerder, D. P. 1988, in *Cool Stars, Stellar Systems, and the Sun*, eds. J. Linsky and R. Stencel (Dordrecht: Reidel), p. 512.
Huenemoerder, D. P., and Ramsey, L. W. 1987, *Ap. J.*, **319**, 392.
Poe, C. H., and Eaton, J. E. 1985, *Ap. J.*, **289**, 644.
Ramsey, L. W., and Nations, H. L. 1980, *Ap. J. (Letters)*, **239**, L121.
Rodonò, M. *et al.* 1986, *Astr. Ap.*, **165**, 135.

Smith, M. A., and Jaksha, D. 1984, in *Cool Stars, Stellar Systems, and the Sun*, eds. S. Baliunas and L. Hartmann (Dordrecht: Reidel), p. 183.

Vogt, S. S. 1983, in *Activity in Red Dwarf Stars*, eds. M. Rodonò and P. Byrne, (Dordrecht: Reidel), p. 137.

Wing, R. F., Dean, C. A., and MacConnell, D. J. 1976, *Ap. J.*, **205**, 186.

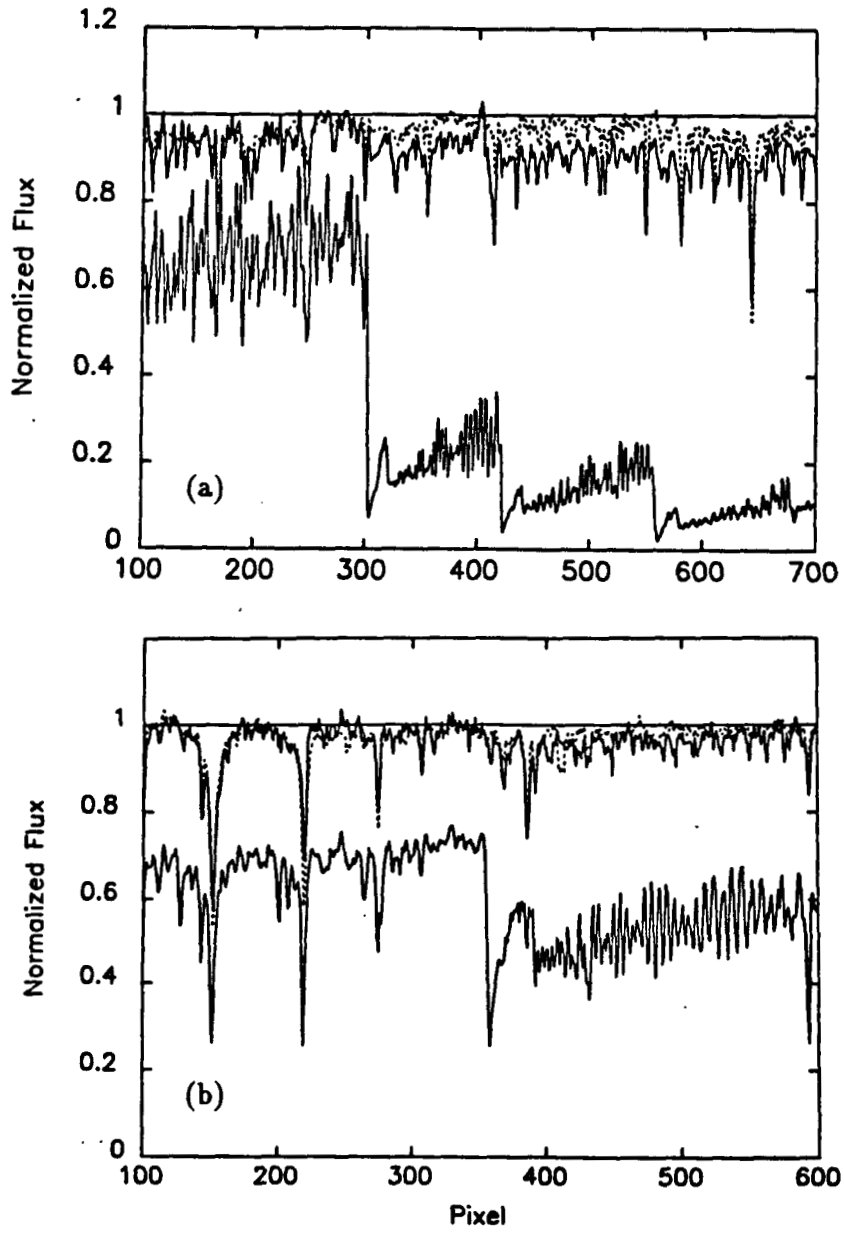

Figure 1. The 7100 Å (a) and 8860 Å (b) spectral regions of the K5Ve flare star BD +26°730 (upper solid curves), the photospheric proxy ξ Boo B (K4V; dashed curves), and the starspot proxy 2 Cen (M4.5III; lower solid curves). Note the excess absorption in the BD +26°730 spectra at the wavelengths of the TiO bands (which are clearly visible in the 2 Cen spectra). We derive $T_{spot} = 3500 \pm 150$ K and $A = 0.20 \pm 0.04$.

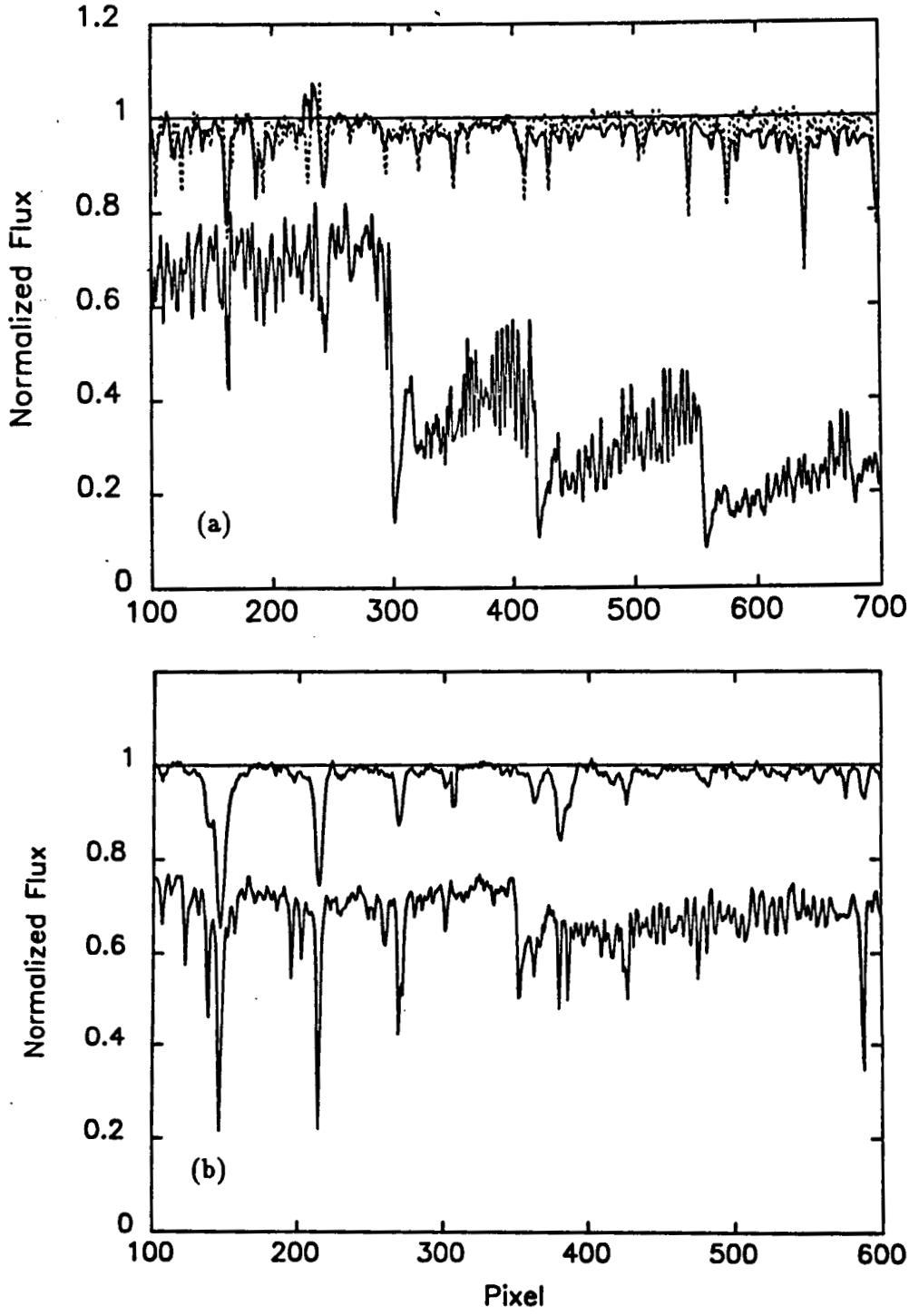

Figure 2. The 7100 Å (a) and 8860 Å (b) spectral regions of the K2Ve flare star HD 82558 (upper solid curves). The spectrum of the photospheric proxy HD 149661 (K1V) is shown in 2a (dashed line). Note the absence of TiO absorption at 8860 Å, indicating warmer spots. An M3III star was the coolest that would fit the data at both wavelengths (μ Gem; lower curves), implying $T_{spot} \geq 3700$ K, and $A \geq 0.22$.

Neutral Beams in Two-Ribbon Flares and in the Geomagnetic Tail*

P.C.H. Martens A. Young

Harvard-Smithsonian Center for Astrophysics

Abstract

We study the current sheet created in the wake of an erupting filament during a two-ribbon flare. A comparison with the geomagnetic tail shows that the physics of these systems is very similar, and that the existence of super Dreicer fields and the generation of neutral beams travelling down the postflare loops with small pitch angles may be expected. The observational evidence for neutral beams is reviewed, and found to be generally supportive, while contradicting the widely held hypothesis of electron beams.

Numerical simulation of individual particle orbits confirms the similarity with the acceleration process in the geomagnetic tail. It is further demonstrated that the results for selfconsistent numerical simulations of the current sheet in the geomagnetic tail can directly be scaled to the coronal current sheet, and the scaling parameters are derived.

Subject Headings: Plasmas, Particle Acceleration, Sun: Magnetic Fields, Sun: Flares, Sun: X-Rays

*Paper presented at the "Second Workshop on Impulsive Flares", University of New Hampshire, Sept. 1988

1 Introduction

Two-ribbon flares are the largest flares observed on the sun, and filament eruptions are often considered as their physical cause (Carmichael 1964, Van Tend and Kuperus 1978). Observations (Dennis 1985, Cliver *et al.* 1986), as well as numerical models (Kuin and Martens 1986, Mikic *et al.* 1988), and theoretical considerations (Pneumann 1980, Kaastra 1985) demonstrate the origin of a current sheet below the erupting filament, where the postflare loops are formed, and where most of the conversion of magnetic energy to particle kinetic energy takes place. This current sheet will be considered here in detail, and compared to the geomagnetic tail and a laboratory experiment (Stenzel *et al.* 1985).

During a large two-ribbon flare about 10^{32} erg of magnetic energy is dissipated and eventually radiated away over the whole electromagnetic spectrum, or emitted as relativistic particles. The peak conversion rate, in the impulsive phase of the flare, is about 10^{29} erg s^{-1}. In the current sheet the magnetic energy is either converted into thermal energy, producing a superhot (10^8 K) plasma in the flare loops, or into electron beams, or, perhaps, neutral beams. The observed hard X-rays would be radiated directly from a superhot plasma, while electron beams would generate "thick target" hard X-rays upon impact on the chromosphere, after traveling downward along the postflare loops. There has been quite a debate in the literature on the "thermal" (superhot plasma) versus the "nonthermal" (electron beam) hypothesis (see Dennis 1988), and neither theory is fully selfconsistent or fully consistent with observations at the moment.

In this paper we will further explore the third alternative mentioned above: neutral beams. This was originally proposed by Simnett and Strong (1984) and Simnett (1986), because these

beams would explain several observations, such as the timing of the chromospheric upflows versus the hard X-rays, much better than either electron beams or a superhot plasma. Recently Martens (1988a,b) and Martens and Young (1988) demonstrated an acceleration mechanism for these beams that is analogous to the acceleration mechanism that operates in the geomagnetic tail (Speiser 1965, 1967, 1968). Several drawbacks of pure electron beams, such as the unacceptably large currents and self magnetic fields induced by the beams (Hoyng *et al.* 1976), as well as the reflection or "mirroring" of the beam electrons with suffiently large pitch angles, are nonexistent in this model because the beams are neutral - with equal amounts of protons and electrons traveling at the same speed - and the beams are injected into the postflare loops with very small pitch angles, as they are in the geomagnetic tail (see Lyons and Williams 1984 for a recent review).

In Section 2 of this paper we will present a brief summary of the acceleration mechanism for the neutral beams, as it is proposed for the geomagnetic tail and in the current sheet of two-ribbon flares. Essential for this mechanism is the existence of very strong electric fields (much larger than the Dreicer field) perpendicular to the magnetic field inside the sheet. We will analyze the the theoretical and observational evidence for the existence of these fields. A comparison between the physical parameters of the coronal current sheet and of the geomagnetic tail will further reveal that despite the enormous differences in their physical parameters, the non-dimensional description is very similar, and consequently an identical acceleration proccess may indeed be expected.

In Section 3 we will explore the observational consequences of neutral beams. Dennis (1988) has recently compared these beams to the Loch Ness monster; because it is almost impossible

to find observations that rule them out directly. We take issue here with this assertion by discussing three independent tests for neutral beams with protons in the 100 KeV range. The first test is the observation of redshifted Lymanα radiation generated by transitions between protons within the beam and neutral chromospheric hydrogen, a test that was proposed by Orral and Zirker (1976) and Canfield and Chang (1985). This crucial test could be carried out on a UV spectrometer with modest temporal and spatial resolution (1%). The second test is the measurement of the polarization of line emission caused by the beam impact ionization of chromospheric hydrogen. This observation has been carried out recently at Meudon in the $H\alpha$ line (Hénoux and Chambe 1988, Hénoux *et al.* 1988, and Hénoux 1989) for three different flares. The results are consistent with the neutral beam model, and *totally inconsistent with deka KeV electron beams*. The third one is the observation of impact polarization in the S I 1437 Å line with the UVSP instrument aboard SMM (Hénoux *et al.*, 1983), which leads to a similar result. In this Section we will also summarize the evidence for neutral beams offered by Simnett (1986), and the measurement of an upper cutoff in proton spectra (Heristchi *et al.* 1976), expected in the present model.

Finally, in Section 4, we will present our numerical results for the simulation of particle orbits in the current sheet of a two-ribbon flare. The results are consistent with the numerical results of Speiser (1965, 1967) for particle orbits in the geomagnetic tail. We will then explore the requirements for fully selfconsistent models for the current sheet, that take into account the current and field generated by the accelerated particles. The familiar MHD-description is inadequate for this type of current sheet, since the particles are essentially collisionless during and after the acceleration, just as in the geomagnetic tail. (However in the geotail the particles

are also collisionless *before* the acceleration, which they are not in the corona). Consequently one cannot assign a temperature or uniform pressure to the plasma. Also, standard MHD resistivity becomes a questionable concept in these circumstances (even if one allows for "anomalous" resistivity). Lyons and Speiser (1985) have recognized this problem for the geotail and derived a formula for its "equivalent" resistivity, which can be negative in certain circumstances! It is a different concept from anomalous resistivity because collisions and wave-particle interactions play no role and consequently the magnetic energy is not converted into thermal particle energy (i.e. kinetic energy with no preference velocity direction) but into beam kinetic energy.

A plasma under these circumstances is usually described by the Vlasov equation that determines the evolution of the distribution function of the particles. However, in simulations for low density plasmas one often encounters difficulties here because densities tend to turn negative. Thus one is forced to model these collisionless current sheets at the most elementary level: by following each individual particle in its orbit, and considering the currents and magnetic fields generated by the these particle motions. Such simulations have been carried out for the geomagnetic tail (see the review by Hockney and Eastwood (1988), Chap. 9-4), but not for the sheet in two-ribbon flares. The basic model and selfconsistency relations for these simulations will be discussed in Section 4. It will be shown that the numerical results for the geomagnetic tail can be scaled to those for the current sheet in a two-ribbon flare, since the dimensionless governing equations have identical form with similar numerical values for the constants. Hence the demonstration of the formation of a quasi-stationary current sheet and proton acceleration for the geotail (Hamilton 1976, 1980) is also valid for the corona.

The final Section of this paper summarizes the main conclusions and suggests future obser-

vations.

2 The Particle Acceleration Mechanism

To explain the observed hard X-ray emission from flares as the result of the impact of a particle beam on the dense chromosphere, the mean energy of the particles has to be about 30 KeV if the beam is composed of electrons (Lin and Schwartz 1987), and 200 KeV if protons are the carriers of the beam energy (Simnett 1986). After acceleration in the current sheet, the mean free path (m.f.p.) for momentum loss by the electrons as well as the protons would be about 10^{10} cm, equal to the length of the whole erupting structure. (We have corrected here for the omission of a factor $(m_e/m_p)^{1/2}$ in Eq. (2) of Martens (1988a) for the m.f.p. of protons. Explicit expressions for the calculation of the m.f.p.'s are given in Trubnikov (1965). Other quantities discussed below are correctly calculated in Martens (1988a), and these calculations shall not be repeated here.)

Given the particle energies, and an estimate of the electric field strength in the sheet of 2 V cm^{-1}, found from the observed photospheric field strength and ribbon velocities (Kopp and Poletto 1986), one can easily calculate the acceleration length of the particles in the sheet, by equating the required particle energy to the potential drop in the sheet over an acceleration length. The result for the solar sheet is an acceleration length of the order of 10^5 cm, 5 orders of magnitude smaller than the m.f.p.! The actual m.f.p. of the particles may be 2 or at most 3 orders of magnitude smaller than 10^{10} cm, because of collective (e.g. wave-particle) interactions, giving rise to anomalous resistivity, but an increase of 5 orders is unlikely for anomalous processes.

Clearly then, particles do not interact during their acceleration process. and one has to consider a different way to limit the acceleration path to about 10^5 cm. This situation is quite similar to that in the geomagnetic tail, where also the m.f.p.'s for protons and electrons are many orders of magnitude larger than the tail's dimensions (see Lyons and Williams 1984 for a review). Early model calculations (Speiser 1965, 1967) prompted by in-situ satellite measurements of electric and magnetic fields have shown that in the geotail the orbits of individual particles are determined by the component of the magnetic field perpendicular to the sheet (B_p): after about half a gyration about this component the particles are ejected from the sheet with a very small pitch angle. Protons and electrons acquire the same velocity. and the beams emanating from the sheet are consequently neutral. For typical solar conditions this gyration radius is indeed about 10^5 cm for protons (Martens 1988a).

Therefore the results of the numerical calculations of Speiser (1965), and in particular the approximate analytical expressions derived there, can be applied to the solar case. The results of this analysis (Martens 1988a) are:

1. The drift of plasma into the sheet continuously supplies the needed 4×10^{35} protons/sec.
2. The sheet magnetic field (about 200 Gauss) generated by the proton current is acceptable despite the large number of accelerated protons. This stands in contrast with the result of Hoyng *et al.* (1976) for electron beams in single loops.
3. Neutral particle beams are injected at the top of the postflare loops with almost zero pitch angle.
4. The generation, timing, and spatial distribution of γ-rays and Hard X-rays, can be explained from a single power law proton spectrum, with cutoffs at about 200 KeV and 20 GeV.

5. The *effective* resistivity in the current sheet, defined as the ratio of electric field to current density, is over 5 orders of magnitude larger than the classical Spitzer resistivity.

Crucial in the derivation of the above results is the large electric field strength of 2 V cm^{-1}, 5 orders of magnitude larger than the Dreicer field. Kopp and Poletto derived this estimate from the $\vec{V} \times \vec{B}$ field determined by the lateral diplacement of the flare ribbons across the normal component of the photospheric magnetic field. It was shown by Forbes and Priest (1984) that in a system with an ignorable coordinate along the filament axis (as is indicated by observations), the electric field at the x-type neutral point is exactly the same as near the ribbons for stationary reconnection. Note that this electric field is *perpendicular* to the magnetic field, except at the neutral point, where there is no magnetic field.

This result is in contrast with the results of experiments in laboratory plasmas, where the electric field is usually limited to the Dreicer field (e.g. Stenzel *et al.* 1983, 1985). On the other hand, the electric field in the geomagnetic tail, determined by *in situ* observations of the reconnection rate, is about 8 orders of magnitude larger than the Dreicer field. In the experiment of Stenzel *et al.* the net electric field in the neutral sheet consists of two parts, an inductive part generated by the magnetic reconnection, and a space charge part, generated by charge build up at the anode and kathode at the endpoints of the sheet. The space charge electric field counteracts the inductive field in such a way that the net field is limited to the Dreicer field.

The current sheet in a two-ribbon flare and the geomagnetic tail are not bounded in the way a laboratory plasma is, and therefore charge separation at the endpoints of the sheet is not possible. For example, charge separation at the endpoints of the flare current sheet (see Fig. 1) would immediately be cancelled by removal of the excess charge carriers along the fieldlines of

the postflare loops connecting to the for all practical purposes infinite reservoir of particles in the chromosphere and photosphere. Consequently the net electric field is completely determined by the reconnection rate of the magnetic field.

As was noted by Kopp and Poletto (1986) the strict mathematical result of Forbes and Priest (1984) for the inductive electric field is not applicable in the absence of perfect symmetry along the axis of the filament. However, according to Faraday's law a net electric field is always induced along the magnetic null line when two flux systems exchange magnetic flux, irrespective of symmetry. Farady's law can be integrated along the x-type neutral line, as done in Kopp and Poletto (their Eq. (4)) to express the net voltage drop along the neutral line as a function of the increase in net flux in the postflare loop system. The latter is equal to the photospheric line of sight flux bypassed by the lateral motion of the flare ribbons, that is directly measured. The two flux systems in the present model are (1) the loops overlying the filament, and (2) the postflare loops plus the field of the filament (see Fig. 1). The flux exchange leads to the formation of new postflare loops through reconnection within the current sheet.

Clearly then, large electric fields in the current sheet that is created in the wake of an erupting filament can only be avoided when either there is a space charge electric field, or there is no reconnection at the top of the postflare loops (no flux exchange). The first possibility was ruled out above. The second one would imply that the same arcade of loops connects to the x-type neutral line during the flare, and its footpoints would not change position, in contrast to the observed lateral motion of the ribbons. However, it is possible that the observed Hα ribbons have nothing to do with loops connecting to the current sheet. Instead some MHD instability can be envisaged to take place at sequentially higher and higher loops that already existed before

the flare. The ribbons then still are the chromospheric signature of the energy release within each subsequent arcade of loops. In this picture the whole preflare structure would simply be stretched out during the flare, without any change in topology.

There are several possible observations that could determine whether the reconnection or the stretching picture is correct. The first one is by directly measuring the electric field during flares: a field of several V cm^{-1} would imply reconnection. A second straightforward test is the observation of changes in topology. Suppose one can observe a preflare loop overlying the filament before eruption, and determine its footpoint positions. If, during or after the eruption, the ribbons connecting the postflare loops cover or go beyond the footpoints of the preflare loop, reconnection *must* have taken place.

We are not aware of any direct observation of topology changes, but electric field measurements have recently been attempted. Foukal *et al.* (1983, 1986, 1987) have derived an upper limit of about 10 V cm^{-1} for the macroscopic electric field in eruptive prominences and postflare loops by observations of Stark broadening in Balmer and Paschen lines. Future observations of the polarization of the Paschen lines may allow the measurement of macroscopic electric fields of substantially less than 10 V cm^{-1}, and thus the results of Kopp and Poletto may be verified.

We conclude that the presence of super Dreicer fields in two-ribbon flares is not unambiguously demonstrated from observations, but does provide the most straightforward interpretation of the observations of the formation of postflare loops, and is also suggested by the presence of super Dreicer fields in the similar circumstances of the geomagnetic tail.

A three way comparison between the physical situation in the current sheet of a two-ribbon

flare, the geomagnetic tail and the laboratory plasma experiment of Stenzel *et al.* (1983, 1985) is presented in Table 1. The first part of the Table gives the observed quantities and their references. From these, and assuming that the beam generation mechanism of Speiser (1965, 1967) is at work, one can calculate the sheet physical parameters such as the drift velocity, the m.f.p.'s, the proton acceleration length, the effective resistivity, number of accelerated protons, net current, etc. (see Martens 1988a for the results for the geotail and the corona).

The effective resistivity is a parameter of particular significance since it is more than 5 orders of magnitude larger than the classical Spitzer resistivity in the coronal current sheet. It is derived by considering the momentum equation for the protons in the current sheet,

$$m_p \frac{d\vec{V}}{dt} = \epsilon \vec{E} - \frac{m_p V_p \vec{V}}{m.f.p.}. \tag{1}$$

In a stationary situation the left hand side of this equation vanishes on the average. The proton acceleration inside the sheet is limited by whatever mechanism ejects the protons from the sheet. Using the definition of the proton current density, $j = n_p \epsilon V_p$ one finds for the *effective* resistivity defined above

$$\eta_{eff} = \frac{m_p V_p}{n_p \epsilon^2 m.f.p.}. \tag{2}$$

The m.f.p. for proton-proton collisions is very large, so collisions are a very ineffective limiter. Speiser's (1965) calculations show that the gyration of the protons along the small remaining ***perpendicular*** component of the magnetic field results in the ejection of the accelerated protons after half a gyration. This limits the acceleration path of the protons to roughly 2 gyroradii of B_p, much less than the collisional m.f.p. Replacing the m.f.p. by two gyroradii one finds

$$\eta_{eff} = \frac{B_p}{n_p \epsilon c}. \tag{3}$$

A more detailed derivation of η_{eff}, and in particular its dependence upon the initial values of V_p is given in Lyons and Speiser (1985). A peculiar aspect of their results is that protons with very high intial velocities are actually decelerated in the sheet, and hence their η_{eff} is negative.

More recently (Martens and Young 1988) we have derived some new results for the current sheet in two-ribbon flares that strengthen the conclusions above. The thickness of the current sheet (δ) may be estimated from the induction law with the assumption of a quasistationary sheet, which is based on the observation that the duration of a flare is much longer than the Alfven travel time through the sheet. The result is

$$\delta = \frac{\eta c^2}{2\pi V_d} \approx 430cm. \tag{4}$$

where V_d is the plasma drift velocity into the sheet (≈ 15 km sec^{-1}). The net energy conversion in the sheet (P) can be derived as follows.

$$P = IEL \approx 6 \times 10^{28} erg/sec. \tag{5}$$

where I is the current in the sheet, E the electric field, and L the length of the sheet. This result is in good agreement with the energy requirements in the impulsive phase in large flares.

Finally, from magnetic flux conservation we derive an estimate for the perpendicular magnetic field component. Equating the inflow of magnetic flux to the outflow, one finds

$$V_{in} B_{sheet} = V_{out} B_p. \tag{6}$$

The inflow velocity is equal to the drift velocity, but the outflow velocity is not known a priori. Its maximum value is the local Alfven speed. For the geomagnetic tail all the quantities in Eq. (6), except V_{out}, have been measured (Lyons and Williams 1984), and V_{out} is found to be equal

to the Alfven speed. This corresponds to maximum energy conversion in the sheet. We *assume* that the same situation holds for the flare current sheet, and the result is $B_p \approx 0.7$ Gauss. Given this value the average energy of the accelerated protons can be calculated with the approximate formula given by Speiser (1965),

$$U_p \approx 2m_p c^2 (E/B_p)^2 \approx 174 KeV. \quad (7)$$

This result is consistent with the average energy of 200 KeV required from observations (Simnett 1986), that was used as an input parameter in our calculations. Hence the assumption $V_{out} = V_A$ is justified by the observational constraints on our model. We further note that $V_{out} = V_A$ is a common characteristic of many different sorts of sheet models (see Priest 1981, Chap. 3, for a review). Note also that the B_p calculated is the one at the edge of the sheet. Near the center B_p is much smaller, even reversing sign at the axis. Consequently the protons accelerated near the center of the sheet can acquire much higher energies, theoretically up to the full potential drop along the sheet of 20 GeV.

In the second part of Table 1 the results for some dimensionless parameters of the three plasmas are compared. It is obvious from the Debye number, plasma-β, and ratios of plasma- to gyrofrequency that the plasma of the geotail and the flare current sheet are quite similar, despite their greatly different dimensional parameters. Equally obvious is the great difference with Stenzel's plasma experiment, despite the greater similarity in dimensional parameters between the coronal current sheet and the experiment. The sheet thickness for the geotail and coronal current sheet are calculated with Eq.(4) above. For the geotail the result is in agreement with spacecraft measurements, while in the corona direct experimental verification is impossible at this time. The thickness of the laboratory sheet is directly observed. In Stenzel's laboratory

current sheet most of the current is not carried by protons, but by electrons. The net electric field is smaller than the Dreicer field because of the charge build-up at the anode and kathode, that cancels the inductive electric field. The derivation of the perpendicular field component for the coronal current sheet (Eq. (6)), only indirectly verifiable, was discussed above. The effective resistivity (Eq. (3)) can be verified indirectly from the observed net energy conversion rates (Eq. (5)), giving good agreement for the geotail and the corona. For the laboratory experiment η_{eff} is found as the ratio between current density and electric field.

Our conclusion from the comparison in Table 1 is that the particle acceleration process in the geomagnetic tail and in the current sheet of a two-ribbon flare, both astrophysical plasmas without walls and with resembling dimensionless characteristics, are likely to be similar.

3 Observational Signatures of Neutral Beams

Protons have been proposed as the primary means of energy transfer in flares from early on (Carmichael 1964, Elliot 1964, Schatzman 1967), but in the last decade or two electron beams have been the main focus of attention. Recently Simnett and Strong (1984) and Simnett (1986) have argued that the electron beam hypothesis should be reexamined, because it fails to explain some key observations, and that neutral beams with protons as the carriers of the beam energy provide a straightforward explanation for the same observations. Their main arguments are:
(1) SMM-FCS observations of the Ca XIX ion (Antonucci *et al.* 1982, 1984) show sometimes large non-thermal line broadening and high upflow velocities *prior* to the onset of the impulsive phase (hard X-ray emission) of flares. This requires large energy deposition in the chromosphere

prior to the impulsive phase, and electron beams cannot do this without generating substantial thick target X-ray emission, which is by definition not observed. Proton beams *can* generate such heating without producing X-rays. Only when the heating rate in the chromosphere due to the bombardment by protons surpasses a certain treshold value, a superheated plasma will be generated (Fisher *et al.* 1985, Fisher 1987) that emits hard X-rays: this is the impulsive phase of the flare. (Note that in this scenario the X-ray emission is generated by thermal electrons).

(2) X-rays generated by thick target impact of electron beams should be anisotropical and polarized, in contrast to thermal X-rays. Observations show isotropy (Kane *et al.* 1980) from simultanuous stereoscopic data, and only small upper limits to polarization (Tramiel *et al.* 1984) incompatible with electron beams. The data are fully compatible with the generation of a superhot plasma in the chromosphere by proton beams.

(3) Observations with the SMM-GRS instrument (Chupp *et al.* 1982, Forrest *et al.* 1981) demonstrate conclusively that high energy protons ($\geq$ 30 MeV) must be present from the onset of the impulsive phase of γ-ray flares: the γ-rays are cotemporal with the hard X-rays within the time resolution of the GRS instrument (2 sec.). The number of high energy protons is at least two orders of magnitude larger than that of high energy electrons (Ramathy and Murphy 1984). One acceleration mechanism for both MeV and KeV protons (as proposed in this paper) seems more straightforward than two different but exactly simultanuous mechanisms for KeV-electrons and MeV-protons.

Valid proof for the existence of proton beams, however, can never be obtained from arguments against electron beams or plausibility arguments alone. Dennis (1988) has compared proton beams to the Loch Ness monster just because all the evidence for their existence is of the above

nature. The observational difficulty with hecta KeV protons is that they do not generate X-rays upon impact, or μ-waves during their transport, as deka KeV electrons do.

We will discuss three independent observational tests for proton beams here, two giving evidence for proton beams, and the other inconclusive.

Orral and Zirker (1976) and Canfield and Chang (1985) have investigated the interaction of proton beams with the parly ionized chromosphere. They find that the main source of Lα wing emission is charge exchange from the proton beam followed by spontaneous bound-bound transitions of the beam atoms. The increase in Lα wing emission that is predicted for typical beam fluxes and proton energies is several orders of magnitude larger than what has been observed from Skylab for two flares (Canfield and VanHoosier 1980), but "it is not at all clear that those observations were obtained at a time when we expect protons to be present during these events" (Canfield 1988). Hence no clear indication or counterindication for proton beams is found here. Future space based measurements with UV spectrometers with a spectral resolution of 1% or less can resolve this question

Hénoux and Chambe (1988) calculated the polarization in the line emission of hydrogen atoms excited by a beam of protons or electrons. They found that the direction of vibration of the electric field vector generating the the Hα emission is polarized parallel to the incident beam for deka eV electrons and deka KeV protons. (The polarization depends mainly on the *velocity* of the beam particles, hence the m_p/m_e energy ratio). Assuming beam incidence perpendicular to the solar surface, an earth bound polarimeter would observe maximum intensity in the flare site - center of disk direction. For deka KeV electrons and deka MeV protons the electric field vector is polarized in the plane perpendicular to the beam, and hence an earthbound observer

sees polarization perpendicular to the flare site - disk center direction.

Three chromospheric flares were observed at Meudon on July 11 1982 (see the figures in Hénoux 1989, these proceedings), and the results clearly show polarization in the disk center direction for several Hα emitting spots. The timing coincides with the period from the onset to the peak of the soft X-ray emission as observed by GOES 2, which corresponds to the impulsive phase. Hénoux *et al.* (1988) rule out deka eV electrons for two reasons: (1) the m.f.p. of these electrons is so small that they have to come from the transition region, which is unlikely, and more important (2) these electrons do not carry enough energy to power the simultaneous X-rays. Deka KeV electrons, and hence standard electron beams, are ruled out because they would cause polarization in the perpendicular direction to the one observed.

For typical preflare coronal values of $T \approx 2 \times 10^6 K$ and $n_e \approx 2 \times 10^9 cm^{-3}$, and the height of the current sheet at the onset of the flare of about $10^9 cm$ (Martens and Kuin 1989, Takakura *et al.* 1986), one finds a preflare coronal column density of about $4 \times 10^{-6} g\,cm^{-2}$, less than model F_1 in Hénoux *et al.* (1988). From extrapolation of their results we find that the energy flux in the neutral beam that is required is to produce the polarization is about $10^{10} erg\,cm^{-2}\,s^{-1}$, and the protons need to have an initial energy in excess of 200 KeV to reach the Hα producing layer. This is in good agreement with the theoretical results of the previous section: there is a lower energy cutoff in the energy spectrum at 200 KeV, and with the power calculated in Eq. (5), and a surface area of the ribbons of about $10^{19} cm^2$ (length $10^{10} cm$, width $5 \times 10^8 cm$), the predicted energy flux in the beams is $10^{10} erg\,cm^{-2}\,s^{-1}$

Similar observations of impact polarization in the S I 1437 Å line have been made with the SMM-UVSP instrument (Hénoux *et al.* 1983). They found polarization up to 25% within 3 deg

of the flare site - center disk direction, again implying impact by electrons in the deka eV range or protons in the deka KeV range, and again totally inconsistent with the polarization direction expected from deka KeV electron beams. A polarization of 9% was observed during the peak of the impulsive phase (the onset of the soft X-rays), and 25% polarization occurred during the decay phase of the flare, with no polarization in between. While the latter peak in polarization is most easily accounted for by impact of deka eV electrons carrying down heat flux from the hot and dense postflare loops as was proposed by Hénoux *et al.* (1983), the polarization at the onset of the flare cannot be explained this way, in the absence of preflare dense loops. Neutral beams on the other hand, penetrate easily through the tenuous preflare plasma, as was demonstrated above. We thus submit that the flare onset polarization is caused by neutral beams, and that this effect vanishes as the flare loops become denser, because the proton m.f.p. in the corona declines. Later on, in the postflare phase, heat flux carrying electrons revive the polarization. Clearly more observations are required to test this scenario.

Finally we will briefly discuss an old observation that supports the specific proton acceleration mechanism described in the previous section. The maximum attainable proton energy is defined by the full potential drop along the current sheet. With the electric field strength of 2 V cm^{-1} and sheet length of about 10^{10} cm this maximum energy is about 10 GeV. This should be regarded as an absolute upper limit, since only the largest two-ribbon flares have such long filaments. Observations of high energy solar flare protons with the worldwide neutron monitor network in the early 70's (Heristchi *et al.* 1971, 1976), have produced direct evidence for a high energy cutoff in the proton spectrum in the range from 2 to 5 GeV for seven flares for which the cutoff energy could be calculated, close to our theoretical value.

4 Numerical Models

4.1 Single Particle Orbits

We have calculated the trajectories of protons through a model two-ribbon flare current sheet. The equation of motion for a collisionless proton is

$$m_p \frac{d\vec{V}}{dt} = \epsilon(\vec{E} + \frac{\vec{V} x \vec{B}}{c}). \tag{8}$$

We use a coordinate system with $\hat{y}$ along the axis of the sheet, $\hat{z}$ in the direction of the *width* of the sheet, and $\hat{x}$ along the *thickness*. Consequently the variation of the magnetic field in the $\hat{x}$ direction is strongest. We assume a stationary sheet ($\partial_t = 0$) with translation symmetry along its axis ($\partial_y = 0$), as in Speiser (1965). The induction electric field is directed along $\hat{y}$ and constant in space and time, by virtue of these assumptions, the absence of charge separation, and Faraday's law. From Table 1, $E_y = 2$ V cm^{-1}. The $\hat{z}$ component of the magnetic field is constant outside the sheet and varies linearly inside the sheet.

$$\begin{aligned} B_z &= B_s \quad for \quad x \leq -\delta \\ B_z &= -\frac{B_s x}{\delta} \quad for \quad -\delta \leq x \leq \delta \\ B_z &= -B_s \quad for \quad x \geq \delta, \end{aligned} \tag{9}$$

with $B_s = 200$ Gauss (Table 1) and $\delta = 430$ cm (Eq. (4). The y component of the magnetic field is zero everywhere, and the x component, constant in space and time, is found from Eq. (6). $B_p = 0.7$ Gauss. In reality B_p changes slowly in the $\hat{z}$ direction, reversing sign at the sheet axis. Here we use the B_p at the edge of the sheet. The numerical results show that the excursion of a proton in the $\hat{z}$ direction inside the sheet is about equal to the gyroradius calculated from B_p.

and the *final* velocity of the particle, $\approx 10^5$ cm. This is small compared to the scale for variation in B_p (10^9 cm), and hence the constancy of B_p is a good approximation.

Outside the sheet the magnetic field gradient vanishes, and the particle motion is fully integrable (Sivukhin 1965). The particle motion then consists of three components: (1) constant velocity *along* the magnetic field, (2) gyration around the magnetic field lines. (3) $\vec{E} \times \vec{B}$ drift into the sheet. Our numerical results reproduce this correctly. The interesting part of the trajectories is inside the sheet, where the equation of motion is not fully integrable. For most calculations we have restricted ourselves therefore to the time between entry and exit of an orbit. Figure 2 displays the result of one of our calculations.

Inside the sheet the length scale for the variation of the magnetic field is comparable to the proton gyroradius, and the three components of the particle motion described above couple in a nonlinear way. We found that the protons indeed follow trajectories of the type described by Speiser (1965, 1967, 1968), as was surmised in Sect. 2: the protons oscillate rapidly across the midplane of the sheet, at the same time are accelerated along the electric field, and finally are slowly deflected by the small perpendicular component of the magnetic field. After half such a gyration they are ejected from the sheet in a direction almost parallel to the magnetic field. For protons with initial energy of the order of the typical coronal thermal energy, the approximation formula for the final particle energy (Eq. (7)) was found to be correct within 2% for each of many test orbits.

Despite the nonlinearity of the equation of motion some analytical results can be established that lead to insight in the numerical results, and that are useful in the derivation of a fully selfconsistent model. In fact, Speiser (1965) derived an analytical approximation to the proton

trajectories inside the sheet.

Because of the absence of y dependence, the magnetic vector potential can be reduced to óne component,

$$\vec{B} = \vec{\nabla} \times (A_y \hat{y}). \tag{10}$$

In the particular case of the model calculation of this section

$$A_y = -B_p z - \frac{B_s x^2}{2} - E_y t. \tag{11}$$

The y component of the equation of motion (Eq. (8)) may be integrated to yield the conserved canonical momentum in the $\hat{y}$ direction.

$$P_y = m_p V_y - \frac{\epsilon A_y}{c} = C_1 \tag{12}$$

The constancy of B_p yields yet another integral

$$m_p V_z - \frac{\epsilon B_p y}{c} = C_2. \tag{13}$$

Finally, the stationarity gives rise to the third integral, expressing conservation of net energy. Internal multiplication of Eq. (8) with $\vec{V}$ and integration yields

$$\frac{m_p V^2}{2} - \epsilon E_y y = C_3. \tag{14}$$

The three equations above describe the velocity vector field completely as a function of position and initial conditions. However, the constants of motion are not in involution (Chen and Palmadesso 1985) and an analytical solution cannot be derived. The first and the last equation are valid irrespective of the form of A_y, the second depends on the constancy of B_p. However, it should be noted that for practical purposes B_p is usually constant for a typical trajectory.

For constant B_p one can further simplify these equations by changing to a frame in which the electric field is transformed away (see Speiser 1968 for further details).

One cannot derive the ejection energy and ejection angle from the above conserved quantities alone; the numerical integration is needed. However, if we use the numerical result that the particles with low initial velocities are ejected almost parallel to the magnetic field, so that $|\vec{V}_f| \approx |V_{f,z}|$, one can derive from Eq. (13) and Eq. (14) by eliminating y.

$$\frac{m_p V_f^2}{2} \approx 2m_p c^2 (\frac{E_y}{B_p})^2, \tag{15}$$

confirming the estimate of Eq. (7). The qualification *low* initial velocity refers here to the final velocity $V_f \approx \frac{2E_y c}{B_p}$.

4.2 Selfconsistent Sheet Models

In a selfconsistent model one has to take into account that the currents are the result of the relative motion of the protons and the electrons, in other words, the net currents that are found by considering the summation over the individual particle orbits calculated in the previous section need to be consistent with the currents in the originally assumed magnetic field. (In the model of Sect. 4.1 $j_y = \frac{B_x c}{4\pi\delta}$ inside the sheet, and the current density vanishes outside the sheet.)

It may be shown that in a current sheet of the type of the geomagnetic tail the current is mainly carried by the protons, because of their larger gyroradius, and that the electrons will move in such a way as to preserve charge neutrality, and prevent currents other than parallel to the sheet (Eastwood 1972, 1974). In this case the basic equations governing the formation and evolution of a sheet are:

(1) Faraday's law

$$\frac{1}{c}\frac{\partial \vec{B}}{\partial t} = -\vec{\nabla} \times \vec{E}, \tag{16}$$

(2) Ampère's law

$$\vec{\nabla} \times \vec{B} = \frac{4\pi}{c}\vec{j}. \tag{17}$$

(3) the momentum equation for the protons,

$$m_p \frac{d\vec{V}}{dt} = \epsilon(\vec{E} + \frac{\vec{V} x \vec{B}}{c}), \tag{18}$$

(4) the definition of the current density

$$\vec{j} \cdot \vec{E} = n_r \epsilon \overline{\vec{V}} \cdot \vec{E},$$

$$\vec{j} \times \vec{E} = \vec{0}. \tag{19}$$

where the bar indicates the local average over the velocity of all protons at that location. n_r is the proton density, found from summation over the individual protons. Note that since this density is found from summation mass continuity is automatically satisfied, and there is no risk of the density becoming negative at some point in space, as often happens in numerical simulations for low density plasmas with the MHD equations (see Hockney and Eastwood 1988, Chap. 9-4 for a detailed discussion of this approach).

We now consider a sheet of the same type as in Sect. 4.1, i.e. the same coordinate system, $B_y = 0$ and $\partial_y = 0$. We drop for the moment the stationarity, and allow for variations in the $\hat{z}$ direction. Using the above constraints and Faraday's law, Eq. (17), it is found that $\vec{E}$ in the x,z-plane is a gradient type vector. However, because of the absence of charge separation ($\nabla \cdot \vec{E} = 0$) and vanishing $\vec{E}$ at large distances, it can be shown that $E_x = E_z = 0$, and hence

Eastwood's (1972, 1974) result that $j_x = j_z = 0$ is rather plausible. Thus we have.

$$\begin{aligned} \vec{j} &= (0, j_y, 0) \\ \vec{E} &= (0, E_y, 0) \\ \vec{A} &= (0, A_y, 0). \end{aligned} \tag{20}$$

Note that these quantities are *not* independent of time and the z coordinate, as in the previous section. Ampère's law now reduces to

$$\nabla^2 A_y = -\frac{4\pi}{c} j_y, \tag{21}$$

where $\nabla^2 = \partial_x^2 + \partial_z^2$ in the absence of y-dependence.

Of the constants of motion for individual particles only one remains, the canonical momentum in the y-direction

$$P_y = m_p V_y + \frac{\epsilon A_y}{c} = constant. \tag{22}$$

Eqs. (19), (21), and (22) may be combined to give the field equation for the problem

$$\left(-\nabla^2 + \frac{\omega_{pp}^2}{c^2}\right) A_y = \frac{\omega_{pp}^2}{c^2} \frac{\overline{P_y} c}{\epsilon}. \tag{23}$$

with ω_{pp} denoting the (variable) proton plasmafrequency.

$$\omega_{pp}^2 = \frac{4\pi n_p e^2}{m_p}. \tag{24}$$

The field equation has to be solved in conjunction with the two remaining components of the momentum equation for the individual proton orbits, which after the elimination of V_y can be written in the following convenient notation

$$m_p \frac{d\vec{V}}{dt} = -\vec{\nabla}\left[\frac{1}{m_p}\left\{\left(\frac{\epsilon A_y}{2c}\right)^2 - \frac{\epsilon A_y}{2c} P_y\right\}\right]. \tag{25}$$

Note that A_y is a function of time in this equation, so energy is *not* a conserved quantity here.

The above equations model the three dimensional motions of the protons, taking into account the effect of finite gyroradius and frequency, that are absent in the MHD description. The model also represents sound- and Alfven waves. Numerical simulations have been done for the geomagnetic tail (Hamilton 1976, 1980, see Hockney and Eastwood 1988, Chap. 9-4, for an overview) and they demonstrate clearly the formation of a current sheet when particles are injected into an originally current-free x-type magnetic field configuration. It is further found that the sheet configuration is unstable for a cross-sheet field component (B_p) smaller than a certain threshold. It may be expected that the current sheet in a two-ribbon flare is unstable for this reason, because of its large B_s to B_p ratio in comparison to the geotail (Table 1).

We note that there is a natural length scale in the field equation (23), $\ell = \frac{c}{\omega_{pi}}$, that will probably determine the thickness of the current sheet. This length scale is only dependent on the density through Eq. (24). With the typical values of Table 1 we find $\ell \approx 10^5$ cm for the geotail, and $\ell \approx 300$ cm for the solar current sheet, in both cases close to the thickness of the current sheet, obtained from the induction equation (4). Comparison between the expressions for δ and ℓ shows this equality is not at all trivial. This fortunate coincidence further suggests that the results for the evolution of the current sheet in the geomagnetic tail can be scaled directly to the current sheet of a two-ribbon flare.

We have formalized this by considering the dimensionless model equations. First we introduce the following parameter and units:

$$\varepsilon = \frac{B_p}{B_s}.$$

$$
\begin{aligned}
t_o &= \frac{m_p c}{e B_s}, \\
V_o &= \frac{E_o c}{B_p}.
\end{aligned} \tag{26}
$$

Hence the time unit is the inverse proton gyrofrequency, the velocity is normalized such that the final velocity is of the order unity, and the initial (thermal) velocity and drift velocity are very small for both the geotail and the solar corona. The parameter ε expresses the dominance of the sheet magnetic field over the the perpendicular field. The dimensionless equations of motion become

$$
\begin{aligned}
\ddot{x} &= \dot{y} f(x, z, t), \\
\ddot{y} &= \varepsilon h(x, z, t) + \varepsilon \dot{z} g(x, z, t) - \dot{x} f(x, z, t), \\
\ddot{z} &= -\varepsilon \dot{y} g(x, z, t).
\end{aligned} \tag{27}
$$

The functions f, g, h represent respectively B_z, B_x, and E_y, and form the partial derivatives of the dimensionless potential $A(x, z, t)$. By construction they are all of order unity. The ε values for the geotail and the corona are given in Table 1.

Having introduced a unit for time and velocity, the unit for length is automatically determined

$$
l_o = V_o t_o = \frac{m_p c^2 E_o}{B_p B_s \epsilon}. \tag{28}
$$

Introducing this in the field equation (23), and using the obvious definition

$$
P_{y,o} = \frac{e A_{y,o}}{c}, \tag{29}
$$

one finds

$$
(-\nabla^2 + an) A = anP \tag{30}
$$

Here a new parameter α is introduced.

$$\alpha = \frac{4\pi \overline{n_p} E_o^2 m_p c^2}{(B_p B_s)^2} \tag{31}$$

For the geotail the value is 0.33, for the two-ribbon flare 0.43.

Thus the only two relevant parameters in this problem, ε and α, are quite similar in value for the geotail and the corona. Hence the numerical results for the evolution of the geomagnetic tail can simply be scaled to those for the corona, with the use of the physical units given above. The results of Hamilton (1980) show that for an ε-value as low as that calculated above for the coronal sheet the reconnection process will be non-stationary, with intermittent bursts, and the generation of multiple X- and O-type neutral lines in the sheet. This is not inconsistent with the observed nature of the hard X-ray emission.

5 Conclusions

We have argued that there is a great similarity between the physical situation of the geomagnetic tail and the current sheet in the wake of an erupting filament. We have demonstrated that the dimensionless parameters characterizing these plasmas are comparable, and that the predictions for total energy conversion, number of accelerated particles, and proton energies for a two-ribbon flare are in good agreement with observations.

Also, from a numerical computation of individual proton orbits we have verified the applicability of Speiser's (1965, 1967) proton acceleration mechanism to a sheet with solar parameters. Finally we have shown that the similarity between the solar current sheet and the geotail goes so far that the dimensionless evolution equations for both systems, under the assumption of

invariance along the sheet axis, and dominance of proton currents, have similar constants. Consequently the results of numerical simulations of the geotail (Hamilton 1980) can be scaled to the corona.

Further we have reviewed the observational material pertinent to neutral beams populated with hekta KeV protons, and standard deka Kev electron beams. We find that in addition to Simnett's (1986) arguments for neutral beams, recent line polarization measurements (Hénoux *et al.* 1989, these proceedings) seem to rule out standard electron beams in favour of neutral beams. However, the observations are too few, and their interpretation is not yet sufficiently established.

Future measurements of line polarization - either ground based Hα or UV space observations - are clearly desirable, as well as high spectral and temporal resolution measurements of red shifted Lymanα, advocated by Canfield and Chang (1985). On the theoretical side, the application of codes developed for the geotail to solar type sheets is called for.

Studies of coronal plasma processes at the Harvard-Smithsonian Center for Astrophysics are supported by NASA grant NAGW-112.

References

Antonucci, E. and 8 co-authors 1982, *Solar Phys.* **78**, 107.

Antonucci, E. Gabriel, A.H., and Dennis, B.R. 1984, *Ap. J.* **287**, 917.

Canfield, R.C. 1988, private communication.

Canfield, R.C., VanHoosier, M.E. 1980, *Solar Phys.* **67**, 339.

Canfield, R.C., Chang, C-R 1985, *Ap. J.* **295** 275.

Carmichael, H. 1964, "*AAS-NASA Symposium on the Physics of Solar Flares*", NASA SP-50. W.N. Hess (ed.) p. 451.

Chen, J., Palmadesso, P.J. 1986, *J. Geophys. Res.* **91**, 1499.

Chupp, E.L., and 8 co-authors 1982, *Astrophys. J. Letters* **263**, L95.

Cliver, E.W., Dennis, B.R., Kiplinger, A.L., Kane, S.R., Neidig, D.F., Sheely, N.R., and Koomen, M.J. 1986, *Ap. J.* **305**, 920.

Dennis, B.R. 1985, *Solar Phys.* **100**, 465.

Dennis, B.R. 1988, *Solar Phys.* in press.

Eastwood, J.W. 1972, *Planetary & Space Sci.* **20**, 1555.

Eastwood, J.W. 1974, *Planetary & Space Sci.* **22**, 1641.

Elliot, H. 1964, *Planetary & Space Sci.* **12**, 657.

Fisher, G.H. 1987, *Ap. J.* **317**, 502.

Fisher, G.H., Canfield, R.C., McClymont, A.M. 1985. *Ap. J.* **289**, 425.

Forbes, T.G., Priest, E.R. 1984, in: *"Solar Terrestrial Physics: Present and Future"*, NASA-SP 1120, p. 1. D.M. Butler and K. Papadopoulos (eds.).

Forrest, D.J., and 8 co-authors 1981, in: *"Proc. 17th Int. Cosmic Ray Conf."* **10**, 5.

Foukal, P., Miller, P., Gilliam, L. 1983. *Solar Phys.* **83**, 83.

Foukal, P., Hoyt, C., Gilliam, L. 1986. *Ap. J.* **303**, 861.

Foukal, P., Little, R., Gilliam, L. 1988. *Solar Phys.* **114**, 65.

Hamilton, J.M. 1976, *Reading University Computer Science Report.* RCS 49.

Hamilton, J.W. 1980, *"Computer Simulation of the Geomagnetic Current Sheet"*, Ph.D. Thesis, University of Reading.

Hénoux, J.C., and 7 co-authors 1983. *Ap. J.* **265**, 1066.

Hénoux, J.C., Chambe, G. 1988. *J.Q.S.R.T.*, in press.

Hénoux, J.C., Chambe, G., Feautrier, N., Sahal, S., Rovira, M. 1988, submitted to *Nature*.

Hénoux, J.C. 1989, *these proceedings.*

Heristchi, Dj., Trottet, G. 1971, *Physical Rev. Letters* **26**(4), 197.

Heristchi, Dj., Trottet, G., Perez-Peraza, J. 1976. *Solar Phys.* **49** 151.

Hockney, R.W., and Eastwood, J.W. 1988, *"Computer Simulations Using Particles"*. Adam Hilger, Philadelphia.

Hoyng, P., Brown, J.C., Van Beek, H.F. 1976. *Solar Phys.* **48**, 197.

Kaastra, J.S. 1985, *"Solar Flares : an Electrodynamic Model"*. Thesis. University of Utrecht.

Kane, S.R., Anderson, K.A., Evans, W., Klebesadel, R., and Laros, J. 1980, *Astrophys. J. Letters* **239**, L85.

Kopp, R.A., Poletto, G. 1986, *"Coronal and Prominence Plasmas"*, NASA-CP 2442. p. 469. A. Poland (ed.).

Kuin, N.P.M., Martens, P.C.H. 1986, *"Coronal and Prominence Plasmas"*, NASA-CP 2442. p. 241. A. Poland (ed.).

Lin, R.P., Schwartz, R.A. 1987, *Ap. J.* **312**, 462.

Lyons, L.R., Williams, D.J. 1984, *"Quantitative Aspects of Magnetospheric Physics"*. Reidel, Dordrecht.

Lyons, L.R., Speiser, T.W. 1985, *J. Geophys. Res.* **90**, 8543.

Martens, P.C.H. 1988a, *Ap. J. Letters*, **330**, L 131.

Martens, P.C.H. 1988b, in: *"Solar and Stellar Coronal Structure and Dynamics"*, p. 501. R.C. Altrock (ed.). Sunspot NM.

Martens, P.C.H., Young, A. 1988, in: *"Nonlinear Effects in Vlasov Plasmas"*, F. Doveil (ed.). in press.

Martens, P.C.H., Kuin, N.P.M. 1989, *Solar Phys.*, in press.

Mikic, Z., Barnes, D.C., Schnack, D.D. 1988, *Ap. J.* **328**, 830.

Orral, F.Q., Zirker, J.B. 1976, *Ap. J.* **208**, 618.

Pneumann, G.W. 1980. in: *"Solar and Interplanetary Dynamics"*. IAU Symp. **91**, p. 317. Eds. M. Dryer and E. Tanberg-Hanssen.

Priest, E.R. 1981. in: *"Solar Flare Magnetohydrodynamics"*. Chap. 3. p. 139. E.R. Priest (ed.). Gordon and Breach, New York.

Ramathy. R., Murphy, R.J. 1984, in: *"High Energy Transients in Astrophysics"*, p. 628. S. Woosley (ed.). A.I.P. New York.

Schatzman. E. 1967. *Solar Phys.* **1**. 411.

Simnett. G.M. 1986. *Solar Phys.* **106**. 165.

Simnett, G.W.. Strong. K.T. 1984. *Ap. J.* **284**, 839.

Sivukhin. D.V. 1965. in: *"Reviews of Plasma Physics"* **1**. 1. M.A. Leontovich (ed.). Consultants Bureau. New York.

Speiser. T.W. 1965. *J. Geophys. Res.* **70**. 4219.

Speiser. T.W. 1967. *J. Geophys. Res.* **72**. 3919.

Speiser. T.W. 1968. *J. Geophys. Res.* **73**. 1112.

Stenzel. R.L.. Gekelman, W., and Wild, N. 1983, *J. Geophys. Res.* **88**. 4793.

Stenzel. R.L.. Gekelman, W., Urrutia, J.M. 1985, in: *"Magnetic Reconnection & Turbulence"*. p. 63. Eds. M.A. Dubois. D. Gresillon, M.N. Bussac. Editions de Physique. Orsay.

Takakura, T.. Tanaka, K., Nitta, N., Kai, K., and Ohki, K. 1986, *Solar Phys.* **107**. 109.

Tramiel. L.J.. Chanan. G.A., Novick. R. 1984. *Ap. J.* **280**. 448.

Trubnikov, B.A. 1965, in: *"Reviews of Plasma Physics"* **1**, 105. M.A. Leontovich (ed.). Consultants Bureau, New York.

Van Tend, W., Kuperus, M. 1978, *Solar Phys.* **59**, 115

Tables

Table 1: A Comparison between the Plasmaphysics of the Geomagnetic Tail, the Current Sheet in a Two-Ribbon Flare, and Stenzel's Current Sheet Experiment.

Physical Quantity	Geomagnetic Tail	Two-Ribbon Flare	Laboratory
Observations			
Sheet Magnetic field	2×10^{-4} Gauss (1,2)	200 Gauss (3) (typical for active region)	12 Gauss (14)
Sheet Electrical Field	2.5×10^{-6} Volt/cm (1)	2 Volt/cm (4,5)	0.1 Volt/cm (14.15)
Energy of Accelerated Protons	2-100 KeV (1,6) (power law)	200 Kev - MeV range (7) (inferred from Hard X-Rays)	N.A.
Sheet Length	2.6×10^{10} cm (8)	1.2×10^{10} cm (9) (inferred from filament length)	180 cm (14)
Sheet Width ($\neq$ thickness!)	$1.3 - 13 \times 10^{10}$ cm (8)	10^{9} cm (9,10) (inferred from width ribbons)	$\approx$ 40 cm (14.15)
Density of Ambient Plasma	0.02 - 5 cm^{-3} (11)	10^{10} cm^{-3} (12) (typical for active region)	10^{12} cm^{-3} (14)
Temperature of Ambient Plasma	1.5×10^{6} K (13)	$2.0 - 3.0 \times 10^{6}$ K (12) (typical for active region)	$T_e \approx 1.2 \times 10^{5}$ K ($T_p \approx 0.2\ T_e$) (14)
Dimensionless Quantities			
Number of Particles in Debye Sphere	4.0×10^{12}	3.9×10^{7}	3.4×10^{4}
Plasma Beta (outside sheet)	5.2×10^{-3}	4.3×10^{-3}	2
Plasma Freq. /Gyrofreq.	9	1.6	267
Sheet Thickness/Proton Gyroradius before Acceleration	34 (1)	52	0.83 (14)
Sheet Thickness/Proton Gyroradius after Acceleration	0.88 (1)	1.9	N.A.
Electric Field/Dreicer Field	1.2×10^{6}	6.7×10^{3}	0.15
Parallel/Perpendicular Compononent Magnetic Field	20 (1)	290	not measured
Effective Resistivity/ Spitzer Resistivity	1.4×10^{9}	3.0×10^{6}	25
Observed/Calculated Proton Energy after Acceleration	1.5	1.2	N.A.

(1) Lyons, L.R., Williams, D.J. 1984, *"Quantitative Aspects of Magnetospheric Physics"*, Reidel, Dordrecht.

(2) Ness, N.F. *J. Geophys. Res.* **70**, 2989.

(3) Poletto, G., Vaiana, G.S., Zombeck, M.V., Krieger, A.S., Timothy, A.F. 1975. *Solar Phys.* **44**, 83.

(4) Kopp, R.A., Poletto, G. 1986. *"Coronal and Prominence Plasmas"*, NASA-CP 2442, p. 469. A. Poland (ed.).

(5) Foukal, P., Little, R., Gilliam, L. 1988, *Solar Phys.* in press.

(6) Lundin, R., Hultqvist, B., Pissarenko, N., Zackarov, A. 1981. *Kiruna Geophysical Institute*. Preprint # 81:1, Kiruna, Sweden.

(7) Simnett, G.M. 1986. *Solar Phys.* **106**, 165.

(8) Speiser, T.W., Ness, N.F. 1967. *J. Geophys. Res.* **72**, 131.

(9) Kaastra, J.S. 1985. *"Solar Flares : an Electrodynamic Model"*. Thesis, University of Utrecht.

(10) Martens, P.C.H., Kuin, N.P.M. 1989, *Solar Phys.*, in press.

(11) Akasofu, S.-I., Hones Jr., E.W., Bame, S.J., Asbridge, J.R., Lui, A.T.Y. 1973. *J. Geophys. Res.* **78**, 7257.

(12) Rosner, R., Tucker, W.H., Vaiana, G.S. 1978. *Ap. J.* **220**, 643.

(13) Rosenbauer, H.A., Grunwaldt, M.D., Montgomery, G., Paschmann, G., Sckopke. *J. Geophys. Res.* **80**, 2723.

(14) Stenzel, R.L., Gekelman, W., Urrutia, J.M. 1985, in: *"Magnetic Reconnection & Turbulence"*, p. 63. Eds. M.A. Dubois, D. Gresillon, M.N. Bussac. Editions de Physique, Orsay.

(15) Stenzel, R.L., Gekelman, W., and Wild, N. 1983. *J. Geophys. Res.* **88**, 4793.

Figure Captions

Figure 1: The magnetic field structure of an erupting filament. and the associated two-ribbon flare, viewed in a cross-section perpendicular to the filament axis. The location of energy conversion processes is indicated.

Figure 2: A Typical Proton Orbit in the Current Sheet of a Two-Ribbon Flare. Inside the sheet the motion along the $\hat{y}$ and $\hat{z}$ axis is scaled down by a factor 250 resp. 500 for clarity of presentation.

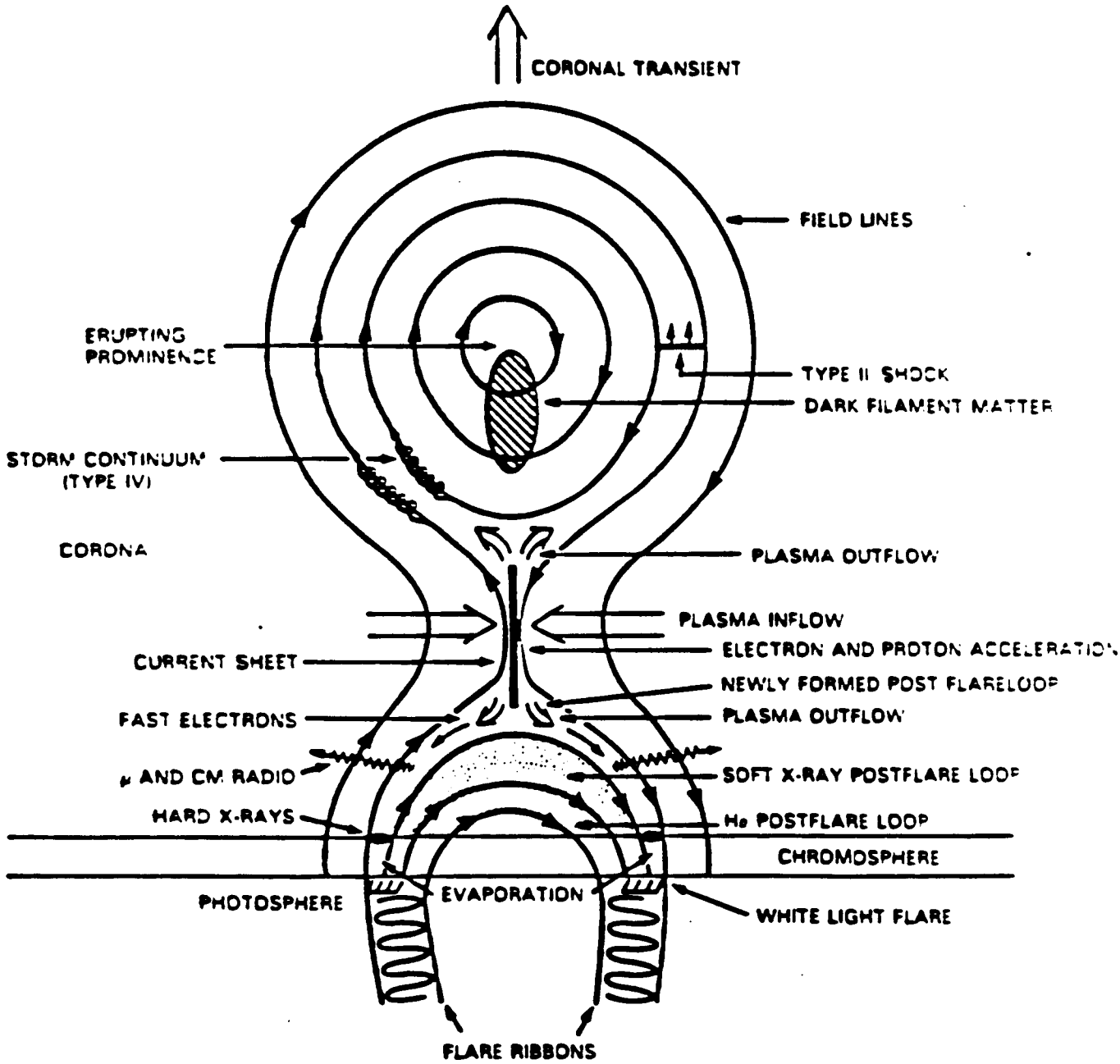
CORONAL TRANSIENT
FIELD LINES
ERUPTING PROMINENCE
TYPE II SHOCK
DARK FILAMENT MATTER
STORM CONTINUUM (TYPE IV)
CORONA
PLASMA OUTFLOW
PLASMA INFLOW
CURRENT SHEET
ELECTRON AND PROTON ACCELERATION
NEWLY FORMED POST FLARELOOP
FAST ELECTRONS
PLASMA OUTFLOW
μ AND CM RADIO
SOFT X-RAY POSTFLARE LOOP
HARD X-RAYS
Hα POSTFLARE LOOP
CHROMOSPHERE
PHOTOSPHERE
EVAPORATION
WHITE LIGHT FLARE
FLARE RIBBONS

Fig. 1

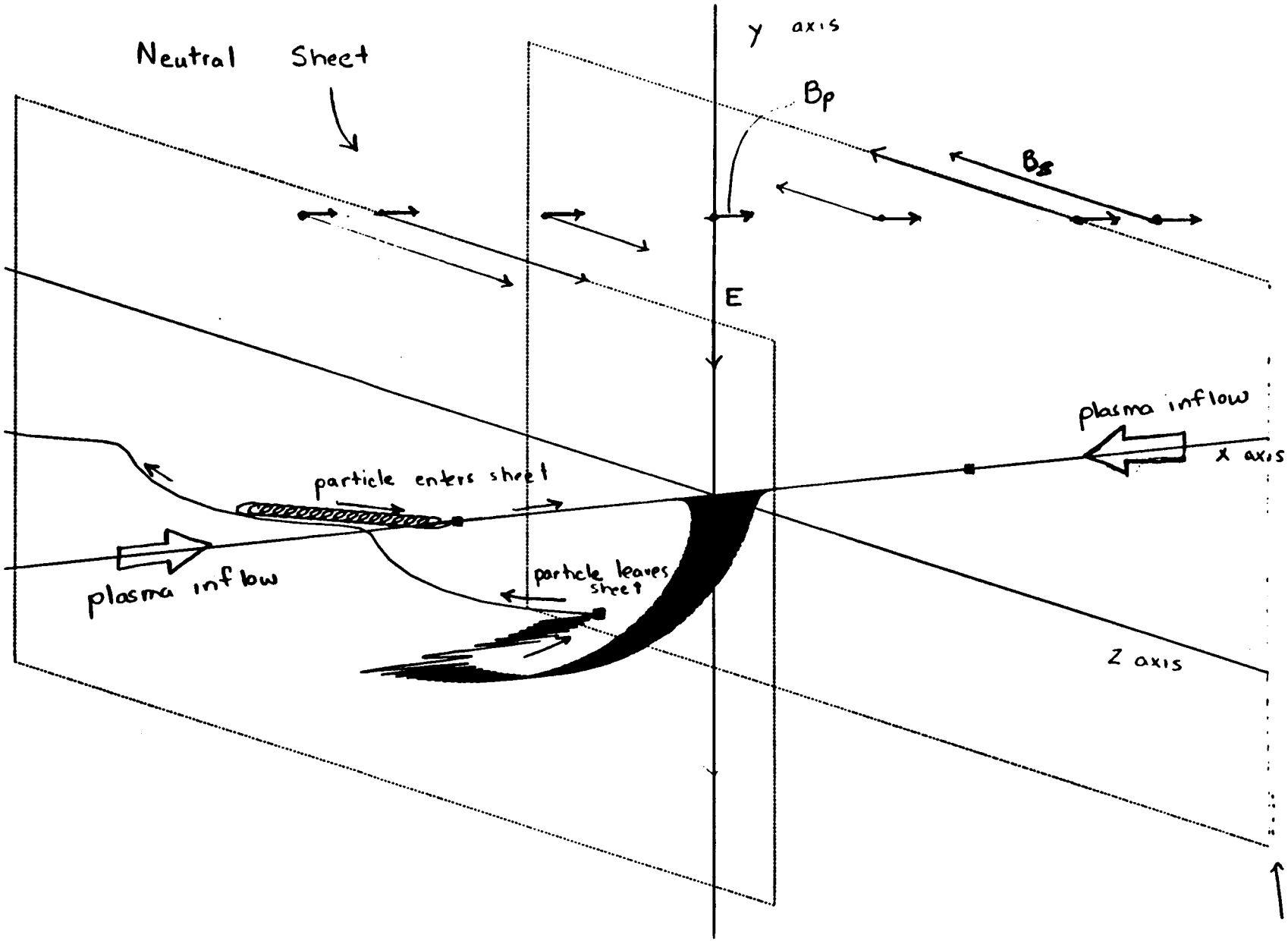

Note to illustrator
the far edge of the
neutral sheet was cut
from the diagram is it
possible to put this back

NAGW-112

Title:

Time-dependent corona models: scaling laws

Authors:

P. Korevaar[1,*] and P.C.H. Martens[2]

Addresses:

[1] Sterrekundig Instituut,
postbus 80000, NL-3508 TA Utrecht, the Netherlands

[2] Harvard-Smithsonian Center for Astrophysics,
60 Garden Street, Cambridge, MA 02138, USA

Running title:

Time-dependent corona models: scaling laws

Send proofs to:

Institut für Theoretische Astrophysik,
Im Neuenheimer Feld 561, D-6900 Heidelberg,
Federal Republic of Germany

Send offprint requests to:

P. Korevaar

Thesaurus code numbers:

07.04.1, 07.06.1, 08.01.1, 14.03.1, 19.29.1, 19.48.1

Section number:

7 (Stellar atmospheres)

To appear in:

The main journal of Astronomy and Astrophysics

* present address:

Institut für Theoretische Astrophysik,
Im Neuenheimer Feld 561, D-6900 Heidelberg,
Federal Republic of Germany

Summary

Scaling laws are derived for the one-dimensional time-dependent Euler equations that describe the evolution of a spherically symmetric stellar atmosphere. With these scaling laws the results of the time-dependent calculations by Korevaar (1989) obtained for one star are applicable over the whole Herzsprung-Russel diagram and even to elliptic galaxies. The scaling is exact for stars with the same M/R-ratio and a good approximation for stars with a different M/R-ratio. The global relaxation oscillation found by Korevaar (1989) is scaled to main sequence stars, a solar coronal hole, cool giants and elliptic galaxies.

key words: galaxies: coronae of — galaxies: elliptical — hydrodynamics — numerical methods — stars: coronae of — stars: mass loss

1 Introduction

If a stellar corona is heated by a mechanical flux greater than a certain limit, it cannot exist as a stationary extended corona. This was found independently by Hearn and Vardavas (1981), Hammer (1982) and Souffrin (1982). Hearn et al. (1983) suggested that a corona heated by a mechanical flux above that limit will undergo a global relaxation oscillation. Time-dependent calculations by Korevaar (1989) have confirmed this. For the one global relaxation oscillation that has been calculated, the corona collapses and rebuilds in about 2 years. It is then quasi-stationary for about 5 years, after which a new collapse occurs. Korevaar (1989) give a detailed description of the relaxation oscillation and explain the physical time scales that dominate the different phases of the global relaxation oscillation.

The corona collapses because thermal conduction, which is independent of the density, is unable to heat the outer layers of the corona sufficiently, when their density surpasses a certain limit. A density pulse is formed at about 50 stellar radii which grows in amplitude as it falls inwards. It hits the photosphere hypersonically with velocities of about Mach 25. Most of the momentum of this infalling pulse is transferred inelastically to the photosphere and much of the kinetic energy is radiated away. The rest of the momentum is reflected in a pulse with an amplitude 2 orders of magnitude lower than the infalling pulse. The rest of the kinetic energy of the infalling density pulse is converted to kinetic energy of the reflected pulse and heats the gas. When sufficient material has moved into the photosphere a new corona is formed by the mechanical heating, and it expands rapidly outwards. During this expansion the photosphere oscillates temporarily at the Brunt-Vaisälä resonance frequency, responding to the momentum transferred by the infalling density pulse. Waves originate from the photosphere and enter the corona. This temporary oscillation is damped by radiation and conduction. The inner corona stabilizes and the remaining waves travel outward until they are damped. The corona then becomes quasi-stationary until a new density pulse is formed in the outer layers and the relaxation oscillation reoccurs.

Korevaar (1989) calculated the relaxation oscillation for the hot supergiant ζ Ori with an effective temperature of $T_{eff} = 31000\ K$, a radius of $R_\star = 27.8\ R_\odot$ and a mass of $M_\star = 44.7\ M_\odot$, reduced to $25.1\ M_\odot$ to include the effective reduction in gravity through electron scattering. One cycle of the global relaxation oscillation requires about 2 hours on a Cyber 205 supercomputer. This makes it impractical to repeat the calculations for a whole range of stars.

Fortunately this is not necessary. The one-dimensional Euler equations that describe the time-dependent behaviour of a spherically symmetric stellar atmosphere can be made dimensionless. In the present paper scaling laws are derived that extend the applicability of the calculations of the global relaxation oscillation over the whole Hertzsprung-Russel diagram and to elliptic galaxies. The scaling is exact between stars with an equal M/R-ratio and a good approximation for stars with a different M/R-ratio.

Hammer (1984) has derived a similar set of scaling laws for the one-dimensional time-independent Euler equations. In the present paper the time dependency is included as well. Hammer's (1984) scaling laws stem from a homologous transformation of the equations, while the scaling laws in the present work are derived by making the flow equations dimensionless. The two methods are essentially the same. Hammer (1984) replaced each physical variable f by $f' \cdot \kappa_f$ and then derived relations between the κ_f's for the various variables. Initially Hammer allows each κ_f to depend on f, but later he requires for a proper scaling that all κ_f's are constant. In the present paper this is required from the beginning.

2 Scaling laws

A set of equations describing the evolution of a given system is expressed in a consistent set of units, usually MKS or Gaussian in astrophysics. The actual choice of units is arbitrary, and one may often employ this freedom to reduce considerably the number of physical parameters in the system. For example, by choosing the unit of mass in stellar evolution calculations as $M_\star$, in stead

of kilograms or grams, the system of equations becomes independent of this parameter. By reducing the number of parameters one also reduces the number of numerical calculations required to investigate the solutions over the range of the parameters.

In most cases it is impossible to eliminate *all* parameters from the equations. The ones that remain lead to scaling laws, so that for a constant value of this parameter one finds identical solutions. The relation between the parameter and the original stellar parameters is the actual scaling law. Two examples are seen in what follows, the expressions for the parameters f and α.

The Euler equations for a one-dimensional time-dependent stellar atmosphere with spherical symmetry are

$$\epsilon_r = \frac{1}{2}\rho_r v_r^2 + \frac{p_r}{\gamma - 1}. \qquad (a)$$

$$p_r = \rho_r \frac{\mathcal{R} T_r}{\mu}, \qquad (b)$$

$$\frac{\partial}{\partial t_r}\rho_r + \frac{1}{x_r^2}\frac{\partial}{\partial x_r}\left(x_r^2 \rho_r v_r\right) = 0. \qquad (c)$$

$$\frac{\partial}{\partial t_r}(\rho_r v_r) + \frac{1}{x_r^2}\frac{\partial}{\partial x_r}\left(x_r^2(\rho_r v_r + p_r)\right) = -\rho_r \frac{\mathcal{G} M_*}{x_r^2} + \frac{2p_r}{x_r}. \qquad (d) \qquad (1)$$

$$\frac{\partial}{\partial t_r}\epsilon_r + \frac{1}{x_r^2}\frac{\partial}{\partial x_r}\left(x_r^2 v_r(\epsilon_r + p_r)\right) = -\rho_r v_r \frac{\mathcal{G} M_*}{r^2} + Q_r^{tot}. \qquad (e)$$

$$Q_r^{tot} = Q_r^{cond} + Q_r^{mech} + Q_r^{rad} + Q_r^{op} \qquad (f)$$

A detailed description of these equations has been given by Korevaar and Van Leer (1988). The dimensionless Euler equations are derived below. Dimensionless quantities are indicated by symbols without a subscript. Real physical quantities have a subscript r and the constant units have a subscript u. The relation between a real quantity q_r, the related dimensionless quantity q and its scale unit q_u is then

$$q_r = q_u q \qquad (2)$$

To enhance the legibility of the equations subscripts of variables that were used in the previous papers have become superscripts. The physical constants used in the present paper are listed in Table 1. The mean molecular weight μ is 0.5 with the assumption that the gas is a fully ionized pure hydrogen gas.

The total energy density e_r is given by

$$e_r = \frac{1}{2}\rho_r v_r^2 + \frac{p_r}{\gamma - 1}, \tag{3}$$

where ρ_r is the mass density, v_r the velocity and p_r the gas pressure. Applying Eq. (2) yields

$$e_u e = \frac{1}{2}\rho_u \rho\, v_u^2 v^2 + \frac{p_u p}{\gamma - 1}. \tag{4}$$

The dimensionless equivalent of Eq. (3) has the same form as Eq. (3) itself,

$$\epsilon = \frac{1}{2}\rho v^2 + \frac{p}{\gamma - 1}. \tag{5}$$

This gives the relation between the units in Eq. (4)

$$\epsilon_u = p_u = \rho_u v_u^2. \tag{6}$$

This simple procedure can now be applied to the other equations. The equation of state is

$$p_r = \rho_r \frac{\mathcal{R} T_r}{\mu}, \tag{7}$$

where T_r is the temperature. This leads to the dimensionless equation

$$p = \rho T. \tag{8}$$

With Eq. (6) the temperature unit must be

$$T_u = \frac{\mu}{\mathcal{R}} v_u^2. \tag{9}$$

The continuity equation in spherical symmetry is

$$\frac{\partial}{\partial t_r}\rho_r + \frac{1}{x_r^2}\frac{\partial}{\partial x_r}\left(x_r^2 \rho_r v_r\right) = 0. \tag{10}$$

where t_r is the time and x_r the distance measured from the stellar centre. With the time unit

$$t_u = \frac{x_u}{v_u} \tag{11}$$

the dimensionless continuity equation becomes

$$\frac{\partial}{\partial t}\rho + \frac{1}{x^2}\frac{\partial}{\partial x}\left(x^2 \rho v\right) = 0. \tag{12}$$

The equation of motion in spherical symmetry is

$$\frac{\partial}{\partial t_r}(\rho_r v_r) + \frac{1}{x_r^2}\frac{\partial}{\partial x_r}\left(x_r^2(\rho_r v_r + p_r)\right) = -\rho_r \frac{\mathcal{G}M_*}{x_r^2} + \frac{2p_r}{x_r}. \tag{13}$$

The term $\mathcal{G}M_*$ is eliminated with the choice

$$v_u = \left(\frac{\mathcal{G}M_*}{x_u}\right)^{\frac{1}{2}}. \tag{14}$$

Then the dimensionless equation of motion becomes

$$\frac{\partial}{\partial t}(\rho v) + \frac{1}{x^2}\frac{\partial}{\partial x}\left(x^2(\rho v^2 + p)\right) = -\frac{\rho}{x^2} + \frac{2p}{x}. \tag{15}$$

The energy equation in spherical symmetry is

$$\frac{\partial}{\partial t_r}\epsilon_r + \frac{1}{x_r^2}\frac{\partial}{\partial x_r}\left(x_r^2 v_r(\epsilon_r + p_r)\right) = -\rho_r v_r \frac{\mathcal{G}M_*}{r^2} + Q_r^{tot}. \tag{16}$$

The quantity Q_r^{tot} represents the sum of all external energy source terms

$$Q_r^{tot} = Q_r^{cond} + Q_r^{mech} + Q_r^{rad} + Q_r^{op} \tag{17}$$

with Q_r^{cond} the thermal conduction, Q_r^{mech} the mechanical heating, Q_r^{rad} the radiation losses and Q_r^{op} the opacity heating. Note that the enthalpy flux is not an external energy source term, but implicitly included in the lefthand side of Eq. (16). The unit for the energy source terms must be

$$Q_u^{tot} = \frac{\rho_u v_u^3}{x_u}. \tag{18}$$

The dimensionless form of the energy equation is then

$$\frac{\partial}{\partial t}e + \frac{1}{x^2}\frac{\partial}{\partial x}\left(x^2 v(e + p)\right) = -\frac{\rho v}{x^2} + Q^{tot}. \tag{19}$$

So far all the dimensionless equations are independent of the stellar parameters. But only if each component of Q^{tot} is independent of the stellar parameters will this also hold for the energy equation.

The thermal conduction is

$$Q_r^{cond} = -\frac{1}{x_r^2}\frac{\partial}{\partial x_r}\left(x_r^2 K_o T_r^{5/2}\frac{\partial T_r}{\partial x_r}\right). \tag{20}$$

Thermal conduction can be defined independently of the stellar parameters only by choosing the density unit

$$\rho_u = K_o(\mu/\mathcal{R})^{7/2} v_u^4/x_u. \tag{21}$$

The dimensionless form of thermal conduction then becomes

$$Q^{cond} = -\frac{1}{x^2}\frac{\partial}{\partial x}\left(x^2 T^{5/2}\frac{\partial T}{\partial x}\right). \tag{22}$$

The mechanical heating is given by

$$Q_r^{mech} = -\frac{1}{x_r^2}\frac{\partial H_r}{\partial x_r}. \tag{23}$$

where $H_r \equiv F_r x_r^2$ is conserved in spherical symmetry if there is no dissipation. and F_r is the local flux of mechanical energy. We choose the unit for H_r in such a way that the flux F^0_{mech} deep in the photosphere—an input parameter for the calculations—is unity. Hence

$$H_u = F_o^{mech} R_*^2. \tag{24}$$

Thus a dimensionless mechanical flux f is introduced. defined by

$$f \equiv \frac{H_u}{\rho_u v_u^3 x_u^2}. \tag{25}$$

With this definition the dimensionless form of the mechanical heating becomes

$$Q^{mech} = -\frac{f}{x^2}\frac{\partial H}{\partial x}. \tag{26}$$

The weak shock-wave dissipation law for the mechanical heating is given by

$$\frac{\partial H_r}{\partial x_r} = -\nu(\gamma+1)\left(\frac{12H_r^3}{\gamma x_r^2 p_r c_r^3}\right)^{\frac{1}{2}}, \tag{27}$$

where ν is the frequency of the sawtooth waves. The adiabatic speed of sound c_r is defined by

$$p_r = \rho_r c_r^2/\gamma, \tag{28}$$

which yields the dimensionless form

$$p = \rho c^2/\gamma \tag{29}$$

if the unit for the adiabatic speed of sound is chosen as

$$c_u = v_u. \tag{30}$$

The dimensionless form of Eq. (27) becomes

$$\frac{\partial}{\partial x} H = -\alpha \left(\frac{H^3}{x^2 p c^3} \right)^{\frac{1}{2}}, \tag{31}$$

where α is given by

$$\alpha = (\gamma + 1) \left(\frac{12 f}{\gamma} \right)^{\frac{1}{2}} \nu \frac{x_u}{v_u}. \tag{32}$$

Both f and α are input parameters because F^0_{mech} and ν are physical parameters. For constant f and α from one star to another an identical solution is found, and hence a scaling law is found for F^0_{mech} and ν.

The radiation losses are

$$Q^{rad}_r = \rho^2 P^{rad}_r(T_r). \tag{33}$$

A good approximation for the radiation loss function P^{rad}_r for a hot tenuous plasma is a $T_r^{-1/2}$-law. This approximation will be discussed further in Sect. 3. A modified radiation loss function $p^{rad}_r(T_r)$ is defined by

$$P^{rad}_r(T_r) = p^{rad}_r(T_r)\, T^{-1/2}. \tag{34}$$

The function p^{rad}_r is a correction term to the $T_r^{-1/2}$-law approximation for the radiation loss function. If its unit is defined as

$$p^{rad}_u = (\mathcal{R}/\mu)^3 K_o^{-1} \tag{35}$$

the dimensionless form of the radiation losses Eq. (33) is

$$Q^{rad} = \rho^2\, T^{-1/2}\, p^{rad}(T_r). \tag{36}$$

Q^{rad} is still dependent on stellar parameters through the dependence of p^{rad} on T_r, but only weakly.

Finally the opacity heating is

$$Q^{op}_r = W_d(x_r)\, \rho^2_r\, P^{op}_r(T_r; T_{eff}). \tag{37}$$

C-2

The dilution factor W_d is a function only of x_τ/R_*, so the equality

$$W_d(x) = W_d(x_\tau) \tag{38}$$

holds when the distance unit x_u is chosen to be proportional to R_*. This is also demanded by the boundary conditions at the photosphere, which can only be defined independently of the stellar radius, if the distance unit is proportional to it[1]. With the definition of the unit for the opacity heating function

$$P_u^{op} = (\mathcal{R}/\mu)^3 \, K_o^{-1} \, T_u^{-1/2} \tag{39}$$

the dimensionless form of the opacity heating becomes

$$Q^{op} = W_d(x)\rho^2 P^{op}(T_\tau; T_{eff}). \tag{40}$$

The opacity heating P^{op} depends on stellar parameters through its dependence on T_τ and T_{eff}. In contrast to the radiation losses this dependence is rather strong. This is discussed in the next section.

The complete set of dimensionless equations that describe a one-dimensional spherically symmetric stellar atmosphere heated by weak shock-wave dissipation is given by

$$e = \frac{1}{2}\rho v^2 + \frac{p}{\gamma - 1} \tag{a}$$

$$p = \rho T \tag{b}$$

$$\frac{\partial}{\partial t}\rho + \frac{1}{x^2}\frac{\partial}{\partial x}\left(x^2 \rho v\right) = 0 \tag{c}$$

$$\frac{\partial}{\partial t}(\rho v) + \frac{1}{x^2}\frac{\partial}{\partial x}\left(x^2(\rho v^2 + p)\right) = -\frac{\rho}{x^2} + \frac{2p}{x} \tag{d}$$

$$\frac{\partial}{\partial t}e + \frac{1}{x^2}\frac{\partial}{\partial x}\left(x^2 v(e + p)\right) = -\frac{\rho v}{x^2} + Q^{tot} \tag{e}$$

$$Q^{tot} = -\frac{1}{x^2}\frac{\partial}{\partial x}\left(x^2 T^{5/2}\frac{\partial T}{\partial x}\right) - \frac{f}{x^2}\frac{\partial H}{\partial x} - \rho^2 T^{-\frac{1}{2}} p^{rad} + W_d(x)\rho^2 P^{op} \tag{f}$$

$$\frac{\partial}{\partial x}H = -\alpha\left(\frac{H^3}{x^2 p c^3}\right)^{\frac{1}{2}} \tag{g}$$

(41)

[1]This is in contrast to Hammer (1984) who choses the distance unit x_u equal to R_*. This is an unnecessary constraint. In the present paper the distance unit x_u is chosen to be 10 R_* rather than R_*, see Table 2

The units, the relation between the units, and the scaling laws for the physical variables are given in Table 2. The unit for the distance is chosen to be $10\,R_\star$ instead of $R_\star$ because this gives typical coronal values for the other units. The scaling laws are given for two cases, firstly for the general case when the results are a good approximation and secondly for a constant M/R-ratio, in which case the results are exact.

3 Discussion

The dimensionless equations (41a-d) are independent of the stellar parameters. As far as those equations are concerned, the results for one star can be scaled exactly to any other star. The energy source equations (41e-g) contain terms dependent on the stellar parameters. These are the parameters f and α, the modified radiation loss function $p^{rad}(T_r)$ and the opacity heating function $P^{op}(T_r; T_{eff})$. When the free parameters f (dimensionless mechanical flux) and α (dimensionless frequency of the sawtooth waves) are constant from one star to another by a proper scaling of the related free parameters F_o^{mech} and ν, the results of a numerical calculation apply to all those stars.

Expressed in terms of stellar parameters the dimensionless mechanical flux f is

$$f = \frac{F_o^{mech} R_\odot}{10 K_o} \left(\frac{10 \mathcal{R} R_\odot}{\mu \mathcal{G} M_\odot} \right)^{7/2} \frac{(R_\star/R_\odot)^{9/2}}{(M_\star/M_\odot)^{7/2}}. \tag{42}$$

The factor 10 is the proportionality constant between x_u and $R_\star$ (cf. Table 2). Numerically f is given by

$$f = 3.91\ 10^{-6}\ F_o^{mech} \frac{(R_\star/R_\odot)^{9/2}}{(M_\star/M_\odot)^{7/2}} \tag{43}$$

which yields $f = 100$ for the hot O-star ζ Ori used by Korevaar (1989). To keep f constant during the scaling from one star to another, the initial mechanical flux F^0_{mech} must scale like any other energy flux (cf. Table 2)

$$F_o^{mech} \sim M^{7/2} R^{-9/2}. \tag{44}$$

The parameter α can be regarded as a dimensionless reciprocal scale length for dissipation. A larger value for α gives a larger dissipation and thus a shorter effective dissipation scale length (cf. Eq. (41f)). Expressed in terms of stellar parameters α is

$$\alpha = (\gamma+1)\frac{12}{\gamma}^{1/2}\frac{10R_\odot}{\mathcal{G}M_\odot}f^{1/2}\nu\frac{(R_*/R_\odot)^{3/2}}{(M_*/M_\odot)^{1/2}}. \tag{45}$$

Numerically this is

$$\alpha = 3.6\ 10^5\ f^{1/2}\nu\frac{(R_*/R_\odot)^{3/2}}{(M_*/M_\odot)^{1/2}}. \tag{46}$$

With $\nu = 1/17000$ Hz for ζ Ori, α is $6.2\ 10^3$. To keep α constant during the scaling from one star to another, the frequency of the waves ν must scale as

$$\nu \sim Mf^{1/2}R^{-3/2}. \tag{47}$$

For the rest of this paper it is assumed that F_o^{mech} and ν scale as in Eqs. (44) and (47). This means that the dimensionless parameters f and α remain constant during the scaling, and the results of Korevaar (1989) can be applied directly to different objects.

Given this assumption only the modified radiation loss function $p^{rad}(T_r)$ (Eq. (34)) and the opacity heating function $P^{op}(T_r;T_{eff})$ (Eq. (37)) depend on the stellar parameters since they cannot be defined as function of the dimensionless temperature T independently of the choice of the temperature unit T_u.

Opacity heating is completely negligible in a typical corona. It is only important for high density—low temperature conditions which are found in the photosphere and inside the density pulse that falls to the star during the collapse phase in the relaxation oscillation. In these cases the gas is in radiative equilibrium. The opacity heating then defines the radiative equilibrium temperature T_{re} in combination with the radiation losses, such that

$$P_r^{op}(T_{re};T_{eff}) \equiv P_r^{rad}(T_{re}). \tag{48}$$

The equilibrium temperature T_{re} is roughly proportional to the effective temperature of the star.

Consider two stars with the same mass and radius, but with different effective temperatures. The photospheres of both stars have different scale heights, but the stationary coronae of both stars are exactly the same. The coronal structure is completely unaffected by small changes in the photospheric temperature at the base of the transition region. During the collapse phase in the relaxation oscillation all the details are the same except that the temperature inside the infalling density pulse is different. This does not influence the relaxation oscillation. Whether the temperature inside the infalling density pulse is 5000 K or 15000 K is unimportant. The collapse occurs because the density pulse is cool and dense compared with the surrounding gas. The density pulse falls almost freely to the star. Consequently the details of the opacity heating do not affect the validity of the scaling laws.

The radiation losses are defined independently of the stellar parameters except for the correction function $p^{rad}(T_r)$ (cf. Eq. (34)). A $T^{-1/2}$-law for the radiation losses has been found to be a good approximation in the range of coronal temperatures from 10^5 to 10^7 K (Rosner et al., 1978; Endler et al., 1979). Therefore the scaling of the results from one star to another will be a good approximation.

There is a class of stars for which the scaling is exact. When two stars have the same M/R-ratio the temperature unit is the same for both stars as Table 2 shows. This means that they have the same modified radiation loss function $p^{rad}(T_r)$. Then the precise form of the radiation loss function is no longer relevant and the scaling is exact.

4 Applications

The global coronal relaxation oscillation calculated by Korevaar (1989) is but one solution carefully selected to obtain a solution lying just above the threshold of instability. The stable solution and the solution showing the global relaxation oscillation can be scaled using the results of the present paper to other stars. No results are available yet of coronae heated by still higher fluxes

of mechanical energy. Tables 3 and 4 show the results for a corona round ζ Ori scaled to an F5-type star, a solar coronal hole, an M0 supergiant and an elliptic galaxy. Table 3 gives the results for the stable stationary extended corona obtained with a mechanical flux a few percent below the limit of stability, Table 4 gives the results for the relaxation oscillation obtained with a mechanical flux a few percent above the limit of stability.

Main sequence stars have nearly the same M/R-ratio when M is reduced for the outward acceleration due to electron scattering. This can be seen immediately from Table 3 for the hot O-star ζ Ori, an F5-star and the sun. Stars earlier than A0 have radiatively driven winds, while stars later than F0 have so much magnetic activity, that acoustic heating becomes relatively unimportant. except perhaps in coronal holes. F-stars are therefore the best candidates for finding the global relaxation oscillations caused by a high flux of mechanical energy. For the F-type star the period of the relaxation oscillation will last about 3 months, during most of which the corona will be semi-stationary. The collapse phase will last about 1 week, during which time the temperature is sufficiently high (about 6 10^6 K) to be easily observable by the X-ray emission.

The solar corona is heated mainly by dissipation of magnetic energy. For a coronal hole it is not clear what the exact heating mechanism is. The dissipation scale length for Alfvén wave heating is much larger than the observed 0.5 solar radii (Withbroe, 1988). Acoustic heating may therefore play a role in the heating of solar coronal holes. Table 3 shows the main properties. The flux of 4.0 10^5 $erg\,cm^{-2}s^{-1}$ at the transition region is close to the flux of 5 ± 1 10^5 $erg\,cm^{-2}s^{-1}$ deduced from the observations by Withbroe (1988). The period of the sawtooth waves of 580 s found from the scaling relation (cf. Table 3) is also not inconsistent with the idea of sound wave heating of coronal holes. The observed dissipation scale length, which is typically 0.5 $R_\odot$ for a coronal hole, (Withbroe, 1988), is roughly 5 times larger than the one deduced here for purely acoustic heating, and the observed mass loss is 7 times smaller than indicated in Table 3. Relaxation oscillations have not been observed in the solar corona. Probably the heating of a solar coronal hole is not purely acoustic, or perhaps the weak shock-wave dissipation used for the calculations of Korevaar

(1989) is not applicable.

Supergiants usually have a large mass loss. The maximum mass loss calculated for the M0-supergiant (cf. Table 3) is extremely low, which confirms that in winds from supergiants other mechanisms must be important. Radiation pressure on the gas itself does not work for cool giants. Radial oscillations and radiation pressure on grains in the outer winds are possible candidates for wind mechanisms in cool giants.

Scaling of stellar results to galaxies is in principle possible, since a galactic corona is often treated like a pure gas, i.e. a Maxwellian velocity distribution is assumed, so that the equation of state for an ideal gas can be used. The geometry is in general non-spherical, but when the scaling is restricted to elliptic galaxies the spherically symmetric geometry is a good approximation. Table 3 shows that for an elliptic galaxy the M/R-ratio is roughly the same as for main sequence stars. The typical coronal temperature of a galactic corona is thus the same as for stellar coronae, about 10^6 K, and so is the velocity. However, the period of the oscillations is far too large (more than the Hubble time) to make them observable. Therefore the coronal thermal instability of Hearn et al. (1983) and Korevaar (1989) is not observable in the coronae of elliptical galaxies and probably not in other galaxies.

We conclude that a (re)examination of the X-ray observations of F-stars is called for at this time to search for the existence of the coronal relaxation oscillation.

Aknowledgements. Part of this work was done during a visit of P. Korevaar to the Harvard Smithsonian Center for Astrophysics. The visit was made possible with financial aid from the Netherlands Organization for Scientific Research (NWO) and the Smithsonian Coronal Studies Visitors Program. Studies of Coronal Plasma Processes at the Harvard Smithsonian Center for Astrophysics are supported by NASA grant NAGW-112.

References

Allen, C.W.: 1973, *Astrophysical Quantities*, Athlone press, London

Endler, F., Hammer, R., Ulmschneider, P.: 1979, *Astron. Astrophys.* **73**, 190

Hammer, R.: 1982, *Astrophys. J.* **259**, 767

Hammer, R.: 1984, *Astrophys. J.* **280**, 780

Hearn, A.G., Vardavas, I.M.: 1981, *Astron. Astrophys.* **98**, 230

Hearn, A.G., Kuin, N.P.M., Martens, P.C.H.: 1983, *Astron. Astrophys.* **125**, 69

Korevaar, P., Van Leer, B.: 1988, *Astron. Astrophys.* **200**, 153

Korevaar, P., Hearn, A.G.: 1989, *submitted to Astron. Astrophys.*

Mulder, W.A., Van Leer, B.: 1985, *J. Comput. Phys.* **59**, 232

Souffrin, P.: 1982, *Astron. Astrophys.* **109**, 205

Rosner, R., Tucker, W.H., Vaiana, G.S.: 1978, *Astrophys. J.* **220**, 643

Withbroe, G.L.: 1988, *Astrophys. J.* **325**, 442

Table 1: Physical constants

physical constant	symbol	value	unit
ratio of specific heats	γ	5/3	—
mean molecular weight	μ	0.5	—
gravitational constant	$\mathcal{G}$	$6.67\ 10^{-8}$	$cm^3s^{-2}g^{-1}$
gas constant	$\mathcal{R}$	$8.31\ 10^{7}$	$cm^2s^{-2}K^{-1}$
conductivity coefficient	K_o	$1.10\ 10^{-6}$	$g\ cm\ s^{-3}K^{-7/2}$
solar mass	$M_\odot$	$1.99\ 10^{33}$	g
solar radius	$R_\odot$	$6.96\ 10^{10}$	cm

Table 2: Scaling laws. M and R are the ratio's between two arbitrary stellar masses and radii respectively.

physical variable			scaling law	
name	unit	relation	general	$M = R$
distance	x_u	$10\,R_*$	R	R
velocity	v_u	$(\mathcal{G}M_*/x_u)^{1/2}$	$M^{1/2}R^{-1/2}$	1
speed of sound	c_u	v_u	$M^{1/2}R^{-1/2}$	1
temperature	T_u	$(\mu/\mathcal{R})\,v_u^2$	$M\,R^{-1}$	1
time	t_u	x_u/v_u	$M^{-1/2}R^{3/2}$	R
density	ρ_u	$K_o\,(\mu/\mathcal{R})^{7/2}\,v_u^4/x_u$	M^2R^{-3}	R^{-1}
pressure	p_u	$\rho_u v_u^2$	M^3R^{-4}	R^{-1}
energy density	e_u	p_u	M^3R^{-4}	R^{-1}
energy flux	F_u	$\rho_u v_u^3$	$M^{7/2}R^{-9/2}$	R^{-1}
mech. flux x^2	H_u	$F^0_{mech}R_*^2$	$M^{7/2}R^{-5/2}$	R
radiation loss f.	p_u^{rad}	$((\mathcal{R}/\mu))^3/K_o$	1	1
opacity heating f.	P_u^{op}	$p_u^{rad}T_u^{-1/2}$	$M^{-1/2}R^{1/2}$	1
mass loss rate	$\dot{M}_u$	$4\pi\rho_u v_u x_u^2$	$M^{5/2}R^{-3/2}$	R^{-1}

Table 3: Scaled properties for maximal stable coronae obtained with a flux of mechanical energy just below the limit of stability. The stellar parameters are taken from Allen (1973). R_* is the radius, M_* the mass reduced for electron scattering, T^{max} the maximum temperature, $\dot{M}$ the maximum mass loss, F_{tr}^{mech} the mechanical flux at the transition region and $P \equiv 1/\nu$ the period of the sawtooth waves that heat the corona by dissipation.

object	R_* $(R_\odot)$	M'_* $(M_\odot)$	T^{max} (K)	$\dot{M}^{max}$ $(M_\odot/yr)$	F_{tr}^{mech} $(erg\,cm^{-2}s^{-1})$	P (s)
ζ Ori (O 9.5)	27.8	25.1	$2.0\ 10^6$	$1.5\ 10^{-12}$	$1.0\ 10^4$	$1.7\ 10^4$
F5-star	1.2	1.3	$2.4\ 10^6$	$1.0\ 10^{-13}$	$4.4\ 10^5$	$6.7\ 10^2$
coronal hole	1	1	$2.2\ 10^6$	$7.0\ 10^{-14}$	$4.0\ 10^5$	$5.8\ 10^2$
M0-supergiant	12.4	500	$5.5\ 10^4$	$3.4\ 10^{-15}$	$1.9\ 10^{-3}$	$1.8\ 10^6$
Elliptic galaxy	$\sim 10^{11}$	$\sim 10^{11}$	$1.1\ 10^6$	$2.5\ 10^{-3}$	$1.8\ 10^{-7}$	$1.6\ 10^{14}$

Table 4: Scaled properties for the global relaxation oscillation obtained with a flux of mechanical energy just above the limit of stability. t_{osc} is the averaged global oscillation period, T_{col}^{max} is the maximum temperature measured during the collapse of the corona, T_{reb}^{max} is the maximum temperature measured during the rebuilding of the corona, v_{col}^{max} is the maximum inward velocity measured during the collapse and v_{reb}^{max} is the maximum outward velocity measured during the rebuilding of the corona.

object	t_{osc} (yr)	T_{col}^{max} (K)	T_{reb}^{max} (K)	v_{col}^{max} (km/s)	v_{reb}^{max} (km/s)
ζ Ori (O 9.5)	7.0	$5.0\ 10^6$	$7.0\ 10^6$	-500	700
F5-star	0.28	$6.0\ 10^6$	$8.4\ 10^6$	-550	770
solar coronal hole	0.24	$5.5\ 10^6$	$7.7\ 10^6$	-525	735
M0-supergiant	760	$1.4\ 10^5$	$1.9\ 10^5$	-85	115
Elliptic galaxy	$2.2\ 10^{12}$	$2.8\ 10^6$	$3.9\ 10^6$	-370	520

In Proceedings of the 6th Cargese Workshop on Nonlinear Effects in Vlasov Plasmas, (1988), Ed. F. Doveil.

Proton Acceleration in Solar Flares and in the Geomagnetic Tail: A Comparison

P.C.H. Martens and A. Young
Harvard-Smithsonian Center for Astrophysics

Abstract

The current sheet at the top of the postflare loops in a solar two-ribbon flare is shown to bear a strong resemblance to the geomagnetic tail. Consequently, in analogy with the geomagnetic tail, the generation of high energy neutral particle beams is expected, that leave the sheet with a very small pitch angle. The collisionless direct electric field acceleration of the protons and electrons is limited only by the gyromotion of the particles along the magnetic field component *perpendicular* to the sheet.

Approximately 10^{35} protons s^{-1} are produced, and numerical results show a typical energy of about 200 KeV, and a power law energy distribution up to 20 GeV. This population is capable of generating the observed Hard X-rays and γ-rays upon impact on the chromosphere.

Introduction

Two-ribbon flares are the largest flares observed on the sun, and filament eruptions are often considered as their physical cause (Carmichael 1964, Van Tend and Kuperus 1978). Observations (Dennis 1985, Cliver *et al.* 1986), as well as numerical models (Kuin and Martens 1986, Mikic *et al.* 1988), and theoretical considerations (Pneumann 1980, Kaastra 1985) demonstrate the origin of a current sheet below the erupting filament, where the postflare loops are formed, and where most of the conversion of magnetic energy to particle kinetic energy takes place. This current sheet will be considered here in detail.

During a large two-ribbon flare about 10^{32} erg of magnetic energy is dissipated and eventually radiated away over the whole electromagnetic spectrum, with the bulk of the emission in X-rays. The peak conversion rate, in the impulsive phase of the flare, is about 10^{29} erg s^{-1}. The kinetic energy of the ejected filament is of the same order as the emission, underscoring the physical connection between the flare and the filament eruption. A synopsis of the major physical processes during a two-ribbon flare is given in Fig. 1 (from Martens and Kuin, 1988). The electric field in the sheet is perpendicular to the plane of the figure below the filament. The *width* of the sheet is in the vertical direction, and the sheet's *thickness* (negligible compared with the dimensions of the flare) is in the horizontal direction.

The Particle Acceleration Mechanism

To explain the observed Hard X-ray emission from flares as the result of the impact of a particle beam on the dense chromosphere, the mean energy of the particles has to be about 30 KeV if the

beam is composed of electrons (Lin and Schwartz 1987), and 200 KeV if protons are the carriers of the beam energy (Simnett 1986). After acceleration in the current sheet, the mean free path (m.f.p.) of electrons as well as protons would be about 10^{11} cm, larger than the whole erupting structure. (Explicit expressions for the calculation of the m.f.p., number of accelerated particles. and other quantities discussed below are given in Martens 1988, and shall not be repeated here.)

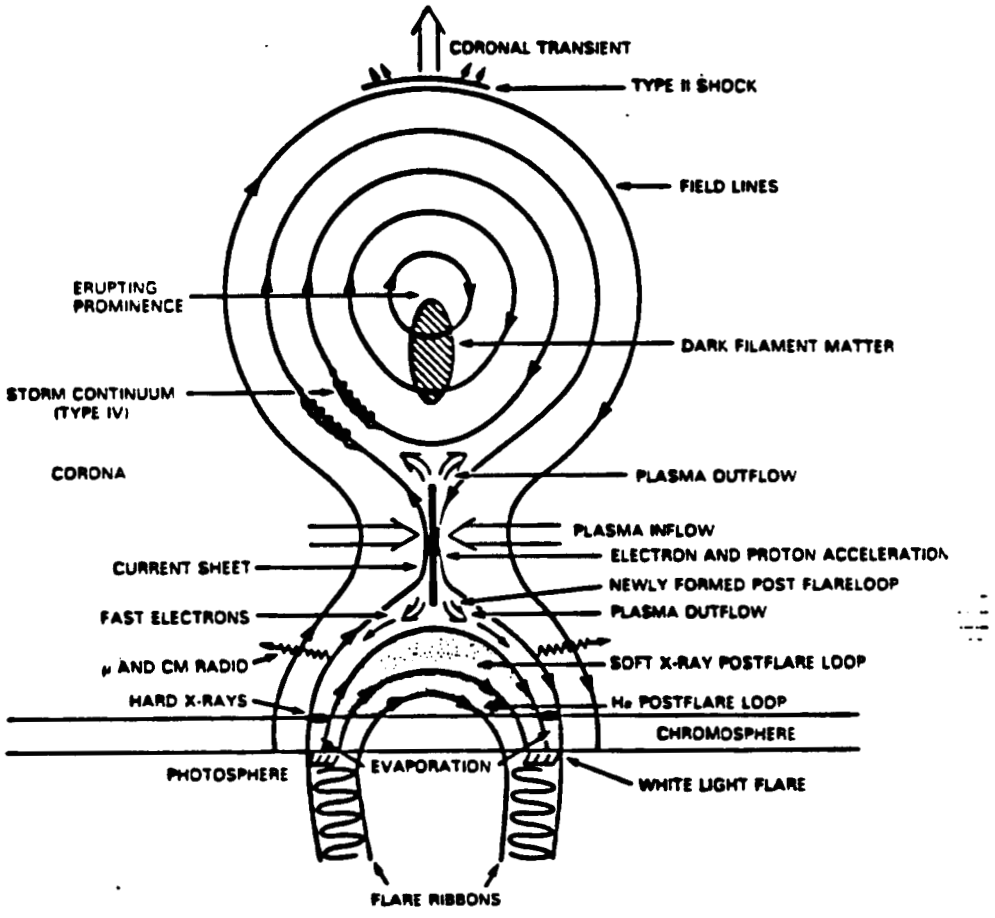

Figure 1. The structure of a two-ribbon flare and the location of the major energy conversion processes, viewed in a cross section perpendicular to the filament axis.

Given the particle energies, and an estimate of the electric field strength in the sheet of 2 Volt/cm, found from the observed photospheric field strength and ribbon velocities with the use of flux conservation (Kopp and Poletto 1986), one can easily calculate the acceleration length of the particles in the sheet, by equating the required particle energy to the potential drop in the sheet over an acceleration length. The result for the solar sheet is an acceleration length of the order of 10^5 cm, 6 orders of magnitude smaller than the m.f.p.! The actual m.f.p. of the

particles may be 2 or 3 orders of magnitude smaller than 10^{11} cm, because of collective (e.g. wave-particle) interactions, giving rise to anomalous resistivity, but an increase of 6 orders is unlikely for anomalous processes.

Clearly then, particles do not interact during their acceleration process, and one has to consider a different way to limit the acceleration path to about 10^5 cm. This situation is quite similar to that in the geomagnetic tail, where also the m.f.p.'s for protons and electrons are many orders of magnitude larger than the tail's dimensions (see Lyons and Williams 1984 for a review). Early model calculations (Speiser 1965, 1967) prompted by in-situ satellite measurements of electric and magnetic fields have shown that in the geotail the orbits of individual particles are determined by the component of the magnetic field perpendicular to the sheet (B_p): after about one gyration about this component the particles are ejected from the sheet with a very small pitch angle. Protons and electrons acquire the same velocity, and the beams emanating from the sheet are consequently neutral. This neutrality, and the small pitch angle, alleviate most of the problems connected to the propagation of pure electron beams (see Dennis 1988 for a recent review), making proton beams an acceptable candidate. Since the protons and electrons in the beam have the same velocity, the protons carry the bulk of the kinetic energy, and the term proton beams is appropriate.

It was shown by Martens (1987, 1988) that the results of the numerical calculations of Speiser (1965), and in particular the approximate analytical expressions derived there, can be applied to the solar case. The results of this analysis are:
1. The convection of plasma into the sheet continuously supplies the needed $4x10^{35}$ protons/sec.
2. The sheet magnetic field (about 200 Gauss) is acceptable despite the large number of accelerated protons, in contrast with Spicer's (1983) conclusion.
3. Neutral particle beams are injected at the top of the postflare loops with almost zero pitch angle.
4. The generation, timing, and spatial distribution of γ-rays and Hard X-rays, can be explained from a single power law proton spectrum, with cut-offs at 100 KeV and 20 GeV.
5. The *effective* resistivity in the current sheet is over 6 orders of magnitude larger than the classical Spitzer resistivity, making the total sheet resistance derived required by observations consistent with the microscopic physics.

Recently we have derived some new results that strengthen the conclusions above. The thickness of the current sheet (δ) may be estimated from the induction law with the assumption of a quasistationary sheet, which is based on the observation that the duration of a flare is much longer than the Alfven travel time through the sheet. The result is

$$\delta = \frac{\eta c^2}{2\pi V_d} \approx 430cm. \tag{1}$$

With the effective resistivity and the plasma drift velocity from Table 1 we find the result of Eq. (1). The net energy conversion in the sheet (P) can be derived in the same manner as in Kaastra (1985). The result is

$$P = IEL \approx 6x10^{28} erg/sec, \tag{2}$$

where I is the current in the sheet, E the electric field, and L the length of the sheet. This result

is in excellent agreement with the observed Hard X-ray emission in the impulsive phase in large flares. Note that the result of Eq. (2) is independent of the effective resistivity or the sheet thickness. Finally, from magnetic flux conservation we derive an estimate for the perpendicular magnetic field component. Equating the inflow of magnetic flux to the outflow, one finds

$$V_{in}B_{sheet} = V_{out}B_p. \tag{3}$$

The inflow velocity is equal to the drift velocity, but the outflow velocity is not known a priori. Its maximum value is the local Alfven speed. For the geomagnetic tail all the quantities in Eq. (3), except V_{out} have been measured (Lyons and Williams 1984), and V_{out} is found to be equal to the Alfven speed. This corresponds to maximum energy conversion in the sheet. We *assume* that the same situation holds for the flare current sheet, and the result is $B_p \approx 0.7$ Gauss. Given this value the average energy of the accelerated protons can be calculated with the approximate formula given by Speiser (1965),

$$U_p \approx 2m_pc^2(E/B_p)^2 \approx 174KeV. \tag{4}$$

This result is in excellent agreement with the average energy of 200 KeV inferred from observations (Simnett 1986), indicating that the assumption $V_A = V_{out}$ is correct. Note that the B_p calculated is the one at the edge of the sheet. Near the center B_p is much smaller, even reversing sign at the axis. Consequently the protons accelerated near the center of the sheet can acquire much higher energies, theoretically up to the full potential drop along the sheet of 20 GeV.

Numerical Simulations

The current sheets of the geotail and a two-ribbon flare are similar, but not identical. So far we have used the results of the numerical calculations for the geomagnetic tail done by Speiser (1965), and extrapolated them for the solar current sheet. The validity of this approach was checked by numerically calculating the orbits of the particles for the flare current sheet. The parameters used in these calculations are given in Table 1. The numerical code evaluates the orbit of a particle in a stationary electric and magnetic field. The equation of motion for the protons is

$$m_p\frac{d\vec{V}}{dt} = e(\vec{E} + \frac{\vec{V}x\vec{B}}{c}). \tag{5}$$

The integration procedure was tested by a comparison with Speiser's (1965) results (see Table 1 for the parameters) and the correspondence was found to be excellent. For the flare sheet we find results that are indeed qualitatively very similar to those for the geotail. A typical proton orbit is shown in Fig. 2. The particle initially gyrates along a field line. As it reaches the sheet it is accelerated and at the same time is slowly deflected by the perpendicular component of the sheet magnetic field. The particle leaves the sheet in a direction almost parallel to the magnetic field. The approximation formula for the particle energy (Eq. (4)) was found to be correct within 30%. It was also found that the initial energy distribution of the protons is of little importance for the final results, in accordance with Speiser's results. In future calculations we intend to take into account the presence of a magnetic field component parallel to the sheet, and the variation of B_p along the width of the sheet.

Table 1: A Comparison between the Plasma Physics of the Geomagnetic Tail and the Current Sheet in a Two-Ribbon Flare

Physical Quantity	Geomagnetic Tail	Two-Ribbon Flare
Observations		
Sheet Magnetic field	$2x10^{-4}$ Gauss (1,2)	200 Gauss (3) (typical for active region)
Sheet Electrical Field	$2.5x10^{-6}$ Volt/cm (1)	2 Volt/cm (4,5)
Energy of Accelerated Protons	2-100 KeV (1,6) (power law)	200 Kev - MeV range (7) (inferred from Hard X-Rays)
Sheet Length	$2.6x10^{10}$ cm (8)	$1.2x10^{10}$ cm (9) (inferred from filament length)
Sheet Width ($\neq$ thickness!)	$1.3 - 13x10^{10}$ cm (8)	10^{9} cm (9,10) (inferred from width ribbons)
Density of Ambient Plasma	0.02 - 5 cm^{-3} (11)	10^{10} cm^{-3} (12) (typical for active region)
Temperature of Ambient Plasma	$1.5x10^{6}$ K (13)	$2.0 - 3.0x10^{6}$ K (12) (typical for active region)
Calculated		
Plasma Drift Velocity	12.5 km/sec	15 km/sec
Mean Free Path Protons: before Acceleration after Acceleration	$3.2x10^{15}$ cm $7.6x10^{17}$ cm	$5.2x10^{5}$ cm $3.0x10^{11}$ cm
Debye Length	$1.3x10^{4}$ cm	$9.8x10^{-2}$ cm
Acceleration Length	$5.2x10^{8}$ cm	$1.0x10^{5}$ cm
Effective Resistivity	$1.7x10^{-6}$ sec	$4.5x10^{-12}$ sec
Sheet Thickness (Eq. (1))	$2.0x10^{8}$ cm	430 cm
Number of Accelerated Protons	$1.1x10^{27}$ sec^{-1}	$3.6x10^{35}$ sec^{-1} (consistent with observational requirements)
Net Current	$3.7x10^{16}$ Statamp	$1.4x10^{21}$ Statamp (consistent with field strength around the sheet)
Net Energy Conversion (Eq. (2))	$8.1x10^{18}$ erg/sec	$1.1x10^{29}$ erg/sec (excellent agreement with observations)
Alfven Velocity	$4.9x10^{7}$ cm/sec	$4.4x10^{8}$ cm/sec
Perpendicular Magnetic Field Component (Eq. (3))	$1.0x10^{-5}$ Gauss	0.69 Gauss
Mean Proton Energy after Acceleration (Eq. (4))	1.3 KeV	174 KeV (excellent agreement with observations)
Dreicer Electrical Field	$2.1x10^{-14}$ Volt/cm	$3.0x10^{-4}$ Volt/cm
Spitzer Collisional Resistivity	$1.2x10^{-15}$ sec	$1.5x10^{-18}$ sec
Larmor Radius upon entering: Protons Electrons	$5.8x10^{6}$ cm $1.4x10^{5}$ cm	8.2 cm 0.19 cm
Proton Velocity after Acceleration	$4.8x10^{7}$ cm/sec	$6.2x10^{8}$ cm/sec
Gyrofrequency: Protons Electrons	0.31 Hz 560 Hz	$3.0x10^{5}$ Hz $5.6x10^{8}$ Hz
Plasma Frequency	$5.1x10^{3}$ Hz	$9.0x10^{8}$ Hz

Table 1 (continued)

Physical Quantity	Geomagnetic Tail	Two-Ribbon Flare
Dimensionless Quantities		
Number of Particles in Debye Sphere	$4.0x10^{12}$	$3.9x10^{7}$
Plasma Beta (outside sheet)	$5.2x10^{-3}$	$4.3x10^{-3}$
Plasma Freq. /Gyrofreq.	9	1.6
Sheet Thickness/Proton Gyroradius before Acceleration	34	52
Sheet Thickness/Proton Gyroradius after Acceleration	0.88	1.9
Electric Field/Dreicer Field	$1.2x10^{8}$	$6.7x10^{3}$
Parallel/Perpendicular Compononent Magnetic Field	20	290
Effective Resistivity/ Spitzer Resistivity	$1.4x10^{9}$	$3.0x10^{6}$
Observed/Calculated Proton Energy after Acceleration	1.5	1.2

References for Table 1

(1) Lyons, L.R., Williams, D.J. 1984, *"Quantitative Aspects of Magnetospheric Physics"*, Reidel, Dordrecht.

(2) Ness, N.F. *J. Geophys. Res.* **70**, 2989.

(3) Poletto, G., Vaiana, G.S., Zombeck, M.V., Krieger, A.S., Timothy, A.F. 1975, *Solar Phys.* **44**, 83.

(4) Kopp, R.A., Poletto, G. 1986, *"Coronal and Prominence Plasmas"*, NASA-CP 2442, p. 469. A. Poland (ed.).

(5) Foukal, P., Little, R., Gilliam, L. 1987, *Solar Phys.* submitted.

(6) Lundin, R., Hultqvist, B., Pissarenko, N., Zackarov, A. 1981, *Kiruna Geophysical Institute*, Preprint # 81:1. Kiruna, Sweden.

(7) Simnett, G.M. 1986, *Solar Phys.* **106**, 165.

(8) Speiser, T.W., Ness, N.F. 1967, *J. Geophys. Res.* **72**, 131.

(9) Kaastra, J.S. 1985, *"Solar Flares : an Electrodynamic Model"*, Thesis, University of Utrecht.

(10) Martens, P.C.H., Kuin, N.P.M. 1988, submitted to *Solar Phys.*

(11) Akasofu, S.-I., Hones Jr., E.W., Bame, S.J., Asbridge, J.R., Lui, A.T.Y. 1973, *J. Geophys. Res.* **78**, 7257.

(12) Rosner, R., Tucker, W.H., Vaiana, G.S. 1978, *Ap. J.* **220**, 643.

(13) Rosenbauer, H.A., Grunwaldt, M.D., Montgomery, G., Paschmann, G., Sckopke, *J. Geophys. Res.* **80**, 2723.

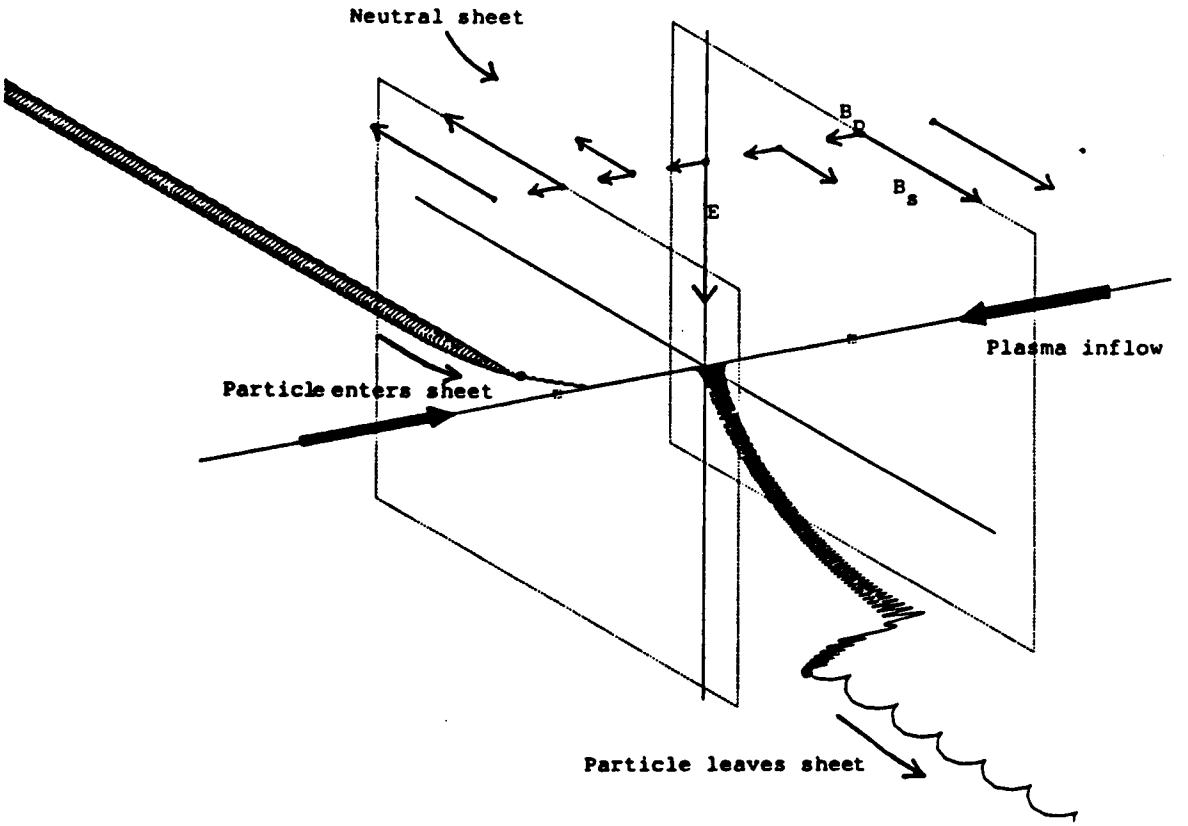

Figure 2. A Typical Proton Orbit in the Current Sheet of a Two-Ribbon Flare. Inside the sheet the perpendicular coordinate has been scaled up by a factor 100.

Conclusions

The comparison of Table 1 shows clearly that the plasma physical parameters of the sheets considered in this paper differ widely. However, the dimensionless quantities calculated in the last part of Table 1 demonstrate that the physical character of the current sheets may be very similar. In particular the electric field in both sheets is many orders of magnitude larger than the Dreicer field, in sharp contrast the situation in the much denser laboratory plasmas (cf. Stenzel *et al.* 1985). Further, the effective resistivity caused by the ejection of highly energetic particles from the sheet, due to the presence of a perpendicular component of the magnetic field, is many orders of magnitude larger than the classical Spitzer resistivity, and also much larger than the resistivities that can be obtained through anomalous processes. Note that such a perpendicular component of the field is necessary in any reconnecting sheet (cf. Petscheck 1964).

We conclude that a direct observational test to discriminate between electron and proton beams in a flare is highly desirable. So far such a direct test has not been proposed.

Studies of coronal plasma processes at the Harvard-Smithsonian Center for Astrophysics are supported by NASA grant NAGW-112.

References

Carmichael, H. 1964, *"AAS-NASA Symposium on the Physics of Solar Flares"*, NASA SP-50, W.N. Hess (ed.) p. 451.

Cliver, E.W., Dennis, B.R., Kiplinger, A.L., Kane, S.R., Neidig, D.F., Sheely, N.R., and Koomen, M.J. 1986, *Ap. J.* **305**, 920.

Dennis, B.R. 1985, *Solar Phys.* **100**, 465.

Dennis, B.R. 1988, *Solar Phys.* in press.

Kaastra, J.S. 1985, *"Solar Flares : an Electrodynamic Model"*, Thesis, University of Utrecht.

Kopp, R.A., Poletto, G. 1986, *"Coronal and Prominence Plasmas"*, NASA-CP 2442, p. 469. A. Poland (ed.).

Kuin, N.P.M., Martens, P.C.H. 1986, *"Coronal and Prominence Plasmas"*, NASA-CP 2442, p. 241.

Lin, R.P., Schwartz, R.A. 1987, *Ap. J.* **312**, 462.

Lyons, L.R., Williams, D.J. 1984, *"Quantitative Aspects of Magnetospheric Physics"*, Reidel, Dordrecht.

Martens, P.C.H. 1987, in: *Proceedings of the* 11^{th} *NSO/SMM summer workshop*, Sac Peak, Aug. 1987. D. Altrock (ed.), in press.

Martens, P.C.H. 1988, *Ap. J. Letters*, **330**, in press.

Martens, P.C.H., Kuin, N.P.M. 1988, submitted to *Solar Phys.*

Mikic, Z., Barnes, D.C., Schnack, D.D. 1988, *Ap. J.* **328**, 830.

Petscheck, H.E. 1964, *"AAS-NASA Symposium on the Physics of Solar Flares"*, NASA SP-50, W.N. Hess (ed.) p. 425.

Pneumann, G.W. 1980, in: *"Solar and Interplanetary Dynamics"*, IAU Symp. **91**, p. 317. Eds. M. Dryer and E. Tanberg-Hanssen.

Simnett, G.M. 1986, *Solar Phys.* **106**, 165.

Speiser, T.W. 1965, *J. Geophys. Res.* **70**, 4219.

Speiser, T.W. 1967, *J. Geophys. Res.* **72**, 3919.

Spicer, D.S. 1983, *Adv. Space Res.*, Vol. **2**, No. 11, p. 135.

Stenzel, R.L., Gekelman, W., Urrutia, J.M. 1985, in: *"Magnetic Reconnection & Turbulence"*, p. 63. Eds. M.A. Dubois, D. Gresillon, M.N. Bussac. Editions de Physique, Orsay.

Van Tend, W., Kuperus, M. 1978, *Solar Phys.* **59**, 115.

THE MAGNETIC FIELDS ON COOL STARS AND THEIR CORRELATION WITH CHROMOSPHERIC AND CORONAL EMISSION

Steven H. Saar
Smithsonian Astrophysical Observatory
60 Garden St., Cambridge, MA 02138, USA

ABSTRACT. I discuss the results of recent measurements of magnetic fields on cool stars and how these measurements relate to stellar "activity". Special emphasis is given to the correlations between the magnetic field strength, surface filling factor, and the non-thermal emission from the hot outer atmospheres of these stars.

1 INTRODUCTION

One of the major lessons we have learned from solar research is the critical role of magnetic fields in governing the structure and energy balance of the solar atmosphere. Evidence for the importance of magnetic fields is widespread. A wide variety of phenomena on the Sun, including spots, plages, granules, flares, and loops, are closely associated with magnetic fields. These inhomogeneities grow and decay in a repeating 11 year cycle, suggesting the continual regeneration of magnetic fields through the operation of a magnetic dynamo. And, directly pertinent to this conference, magnetic fields are crucial for the existence and stability of the million degree solar corona through their role in the heating and confinement of the hot plasma. The dominant heating mechanism for the hot plasmas of the chromosphere and transition region (TR) is also likely magnetic in nature.

By analogy with the Sun, magnetic fields should also be important for other cool stars. Indeed, the fraction of the solar surface covered by magnetic structures is relatively small (at most, 2% of the Sun is covered by magnetic fields); many stars show evidence for considerably more extensive magnetic "activity". The fraction of the surfaces of RS CVn variables covered by spots, can frequently be 100 times larger than the corresponding filling factor of solar umbrae (Vogt 1983). The 11 year cycle of magnetic structures on the Sun is also observed in stars: at present some 60% of cool dwarfs have well determined cycles based on the modulation of chromospheric Ca II emission (Baliunas 1986). The levels of emission from hot plasma in stellar chromospheres and coronae, however, is often orders of magnitude larger than the Sun (e.g., Linsky 1985). A thorough study of stellar magnetic properties would seem to be in order.

Unfortunately, the measurement of magnetic fields on solar-like stars is not trivial.

The most direct means of detecting magnetic fields is through observation of their effect on spectral lines. The presence of a magnetic field will, in general, lift the degeneracy of certain quantum levels in an atom, separating them slightly in energy (the Zeeman effect). The exact number and spacing of the "new" levels (and corresponding allowed transitions) depend on the detailed quantum mechanics of the configuration, but for simple triplet splitting, the shift in wavelength of the two "new" permitted lines from old one is given by $\Delta\lambda_B(\text{Å}) = 4.667\times10^{-13} g_{eff}\lambda^2 B$, where B is the magnetic field strength (in gauss) and g_{eff} is the effective Landé value of the transition. For typical fields of a few kilogauss or less, the Zeeman shift is smaller than the Doppler width of the line and the Zeeman transitions overlap, making them difficult to detect. Clever use of the contrasting polarization properties of the Zeeman components (the $\Delta m = \pm1$ transitions, called σ components, are circularly polarized, and the $\Delta m = 0$ transitions, or π components, are linearly polarized), unfortunately, is thwarted by the bipolar nature of solar and stellar active regions. If mixed polarities exist within the observed region, a proportionate part of the magnetic signal is cancelled, lowering the inferred magnetic flux. In solar work, this is not always an important effect, since the distance separating regions of opposite polarity is often spatially resolvable. For the completely unresolved surfaces of stars, on the other hand, the effect of mixed polarities is ruinous. Almost complete cancellation of the circular polarization signal results when the complex, mixed polarities typical on the Sun were observed as a point source. It is not suprising then, that very few cool stars show *any* net circular polarization (e.g., Borra, Landstreet, and Mayor 1984).

2 TECHNIQUES AND PRELIMINARY RESULTS

So how *does* the intrepid astronomer directly measure stellar magnetic fields? Linear polarization does not cancel completely in integrated light, but is a second order effect and difficult to interpret (Landi Degl'Innocenti 1982). We are left with the unpolarized line profile, with its complex blending of not only σ and π components from magnetic regions, but contributions from non-magnetic portions of the stellar surface as well. The analysis of these various contributions is a difficult problem. Robinson (1980) devised a scheme to deconvolve magnetically sensitive (large Landé g) lines from low g lines. The ratio of the Fourier transforms of the line profiles is modeled; the period of the ratio is proportional to B and the amplitude of the ratio indicates the fraction (f) of the stellar surface occupied by magnetic regions. Several improvements on this basic technique have since been developed (Marcy 1982; Gray 1984; Saar 1988; Basri and Marcy 1988).

Preliminary results of stellar magnetic measurements are beginning to emerge. Marcy (1984) found that the magnetic parameters change as one moves down the main sequence. Gray (1984) found similar magnetic parameters, but did not detect fields on any F dwarfs. The most rapidly rotating star in his sample, π^1 UMa, showed substantially larger surface averaged field (i.e., the product fB) than the others. Marcy and Bruning (1984) could not detect fields on active giants, a fact they ascribe to lower field strengths in these stars with lower surface gravities (see also Gondoin, Giampapa, and Bookbinder 1985). Consistent with this idea, Saar and Linsky (1986) and Saar, Linsky, and Giampapa (1987) reported that among dwarf stars, B increased towards later spectral types and higher surface gravities. They also found an increase in magnetic flux with rotation rate (see also

Linsky and Saar 1987) as first suggested by Gray (1985). Finally, f appears to decrease with stellar age (Linsky and Saar 1987), implying that changes in the filling factor dominate the time evolution of activity.

3 MAGNETIC FIELDS AND UPPER ATMOSPHERIC EMISSION

The apparent connection between magnetic fields and rotation is not surprising, for many authors have demonstrated evidence for a connection between rotation and (presumably) magnetic-related emission from hot plasmas in stellar chromospheres and coronae (e.g., Pallavicini *et al.* 1981; Mangeney and Praderie 1983; Vilhu 1984; Simon and Fekel 1987). The age dependence of chromospheric activity has also been extensively studied (Skumanich 1972; Soderblom 1983; Hartmann and Noyes 1987), and thus the observed decrease
neters with age is not unexpected. It is important, however, to deter-
ctions between the magnetic fields and the outer atmospheric activity
d the underlying physics of the heating.

eported correlations between magnetic parameters, X-ray, and Ca
ıd Schrijver (1987) have combined preliminary magnetic field mea-
ising the methods of Saar 1988) with X-ray and Ca II H+K fluxes.
inear dependence between F_x and fB (Fig. 1), independent of color:
ı in isolation, this result might only indicate that more active re-
ger the surface averaged field or, equivalently, magnetic flux density)
flux, without giving any real information on the heating mecha-
lual active regions on the Sun show a similar relation between X-ray
Schrijver 1987b), suggesting that the coronal heating mechanism is
ıetic flux density. Note that since the magnetic analyses methods
h considerable magnetic flux, the Sun is an important calibration
levels. The strong relationship between B and gravity (Saar and
ıat f is the primary parameter affecting the level of stellar activity.

chromospheric Ca II H+K emission lines is more complex, due to
al photospheric component to the measured flux. Schrijver (1987a)
relations between chromospheric and TR or coronal radiative losses
t "basal" flux (probably acoustic in origin) is subtracted from the
ielding the excess Ca II flux, ΔF_{CaII}. With the relation $F_x \propto$
a), the F_x – fB relation can be rewritten as $\Delta F_{CaII} \propto (fB)^{0.62}$.
solar and stellar data provided fB $\leq$ 300 Gauss (Figure 2). The Ca
sity appears to saturate for values of fB above this level (i.e., at f
f); a similar saturation may be seen in the $F_x - \Delta F_{CaII}$ relation for
er 1987a). The large body of existing Ca II observations indicate
$_{aII} \sim 3$ for G dwarfs, which also coincides with the maximum
ve region (Schrijver and Coté 1987, corresponding to an average
$\sim$ 300 Gauss). The similarity of the solar and stellar saturation
saturation is real (not a selection effect), perhaps the result of a
echanism. X-rays show no such saturation, however, suggesting a
ism operates in stellar coronae.

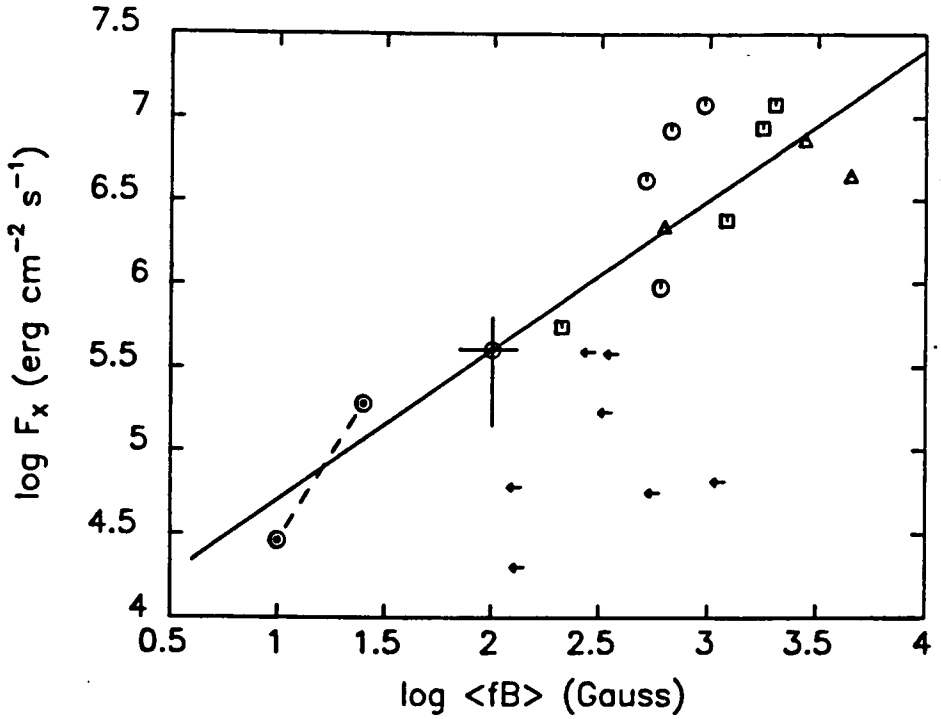

Figure 1: Soft X-ray flux density F_x vs. the mean magnetic flux density fB. The solid line is $F_x \propto (fB)^{0.93}$. Magnetic and X-ray fluxes at solar activity minimum and maximum are connected with a dotted line. For comparison, the mean value of solar active regions (symbol at fB = 100 G) is shown (Schrijver 1987b). Symbols: circles, squares and triangles mark G-, K- and M-type dwarfs respectively.

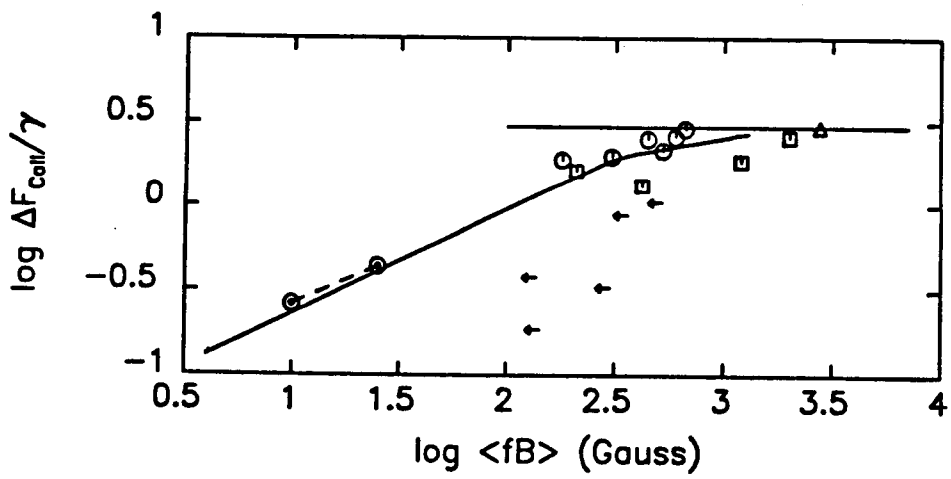

Figure 2: Ca II H+K excess flux density ΔF_{CaII} vs. fB. Symbols as in Fig. 1. The left segment of the solid line is $\Delta F_{CaII} \propto (fB)^{0.62}$, while the right segment is an approximation to the $F_x - \Delta F_{CaII}$ saturation seen in active stars (Schrijver 1987a). The horizontal line segment shows the maximum value observed in solar active regions (Schrijver and Coté 1987) and G dwarfs. The color-dependent decrease in chromospheric emission from M dwarfs has been corrected for by the deficiency factor γ (see Schrijver and Rutten 1987).

I have also studied correlations between the preliminary magnetic parameters and other diagnostics of chromospheric and TR plasma. Stellar surface fluxes in O I (1304 Å), C II (1335 Å), C IV (1550 Å), and Si II (1808 Å) measured with the IUE satellite and analogous solar measurements were gathered from Oranje (1983) and a number of other sources. The preliminary results (based on a small sample of stars) are: $F_{CIV} \propto (fB)^{0.55}$; $F_{CII} \propto (fB)^{0.44}$; $F_{SiII} \propto (fB)^{0.40}$; $F_{OI} \propto (fB)^{0.36}$ (see Figure 3). The cooler chromospheric lines (e.g., O I, with $T_{form} \approx 6 \times 10^3$ °K) show a reduced dependence on fB relative to lines formed higher in the atmosphere (C II, $T_{form} \approx 2 \times 10^4$ °K, and C IV, $T_{form} \approx 10^5$ °K), consistent with the F_x and F_{CaII} results. Note, however, that no "basal" correction has been applied to the O I and Si II data.

Once a larger set of magnetic measurements has been made, it should eventually be possible to begin to test various atmospheric MHD wave heating models for chromospheres, TR and coronae (e.g., Ulmschneider and Stein 1982), test empirical activity theories (Vilhu 1984) and predictions of the range of dynamo time behavior (e.g., Noyes, Weiss and Vaughan 1984) and guide the development of more detailed theories.

4 ROTATIONAL MODULATION OF MAGNETIC AND RADIATIVE FLUXES

Observations of magnetic fields and a wide range of other activity-related diagnostics (Ca II, IUE line emission, He I D3, broaadband linear polarization) on the active G8 dwarf, ξ Boo A, were made in June of 1986. Once again, as no compensation for weak blends was made, the resulting magnetic fluxes should be regarded as preliminary.

Figure 4 shows the normalized magnetic ($\propto$ fB) and ultraviolet fluxes for ξ Boo A plotted versus rotational phase (P = 6.2 days, Noyes *et al.* 1984; $\phi \equiv 0$ defined as the phase of maximum Ca II emission). Rotational modulation of the emission line and magnetic fluxes, in phase with one another, is clearly visible. Lines formed at higher temperatures (C IV, Si IV, He II, C II) appear to show greater modulation than the cooler lines formed in the chromosphere (Ca II, Mg II, Si II, C I, O I). The greater sensitivity of hotter lines to magnetic flux in rotationally modulated *plages* is consistent with the results in §3 for *entire stars*, suggesting that perhaps the main difference between active and quiet stars is the *number* or *size* of plages, and not a major difference in their physical properties. The reduced sensitivity of the chromospheric lines to changes in magnetic flux suggests once more that for stars as active as ξ Boo A (fB $\approx$ 600 Gauss), the heating mechanism for the chromosphere "saturates", while the heating mechanisms operating higher in the atmosphere still are strongly affected by the variable magnetic flux.

Further information on the nature of the magnetic regions on ξ Boo A can be derived from the contemporaneous measurements of broadband linear polarization (P_L). While the polarization amplitude varied by a factor of 3, the angle which the linear polarization vector made with respect to the N-S axis never varied from the 0 – 180 degree line by more than about 10 degrees. The simplest configuration that can reproduce this result (for fields normal to the surface) is a series of active regions which cross the stellar disk near disk center. Since $\sin i \approx 0.6$ for ξ Boo A, the active regions would then be located at intermediate latitudes on the average. The line perpendicular to the polarization angle (i.e., at $\approx 90°$) then corresponds to the stellar rotation axis, entirely consistent with the

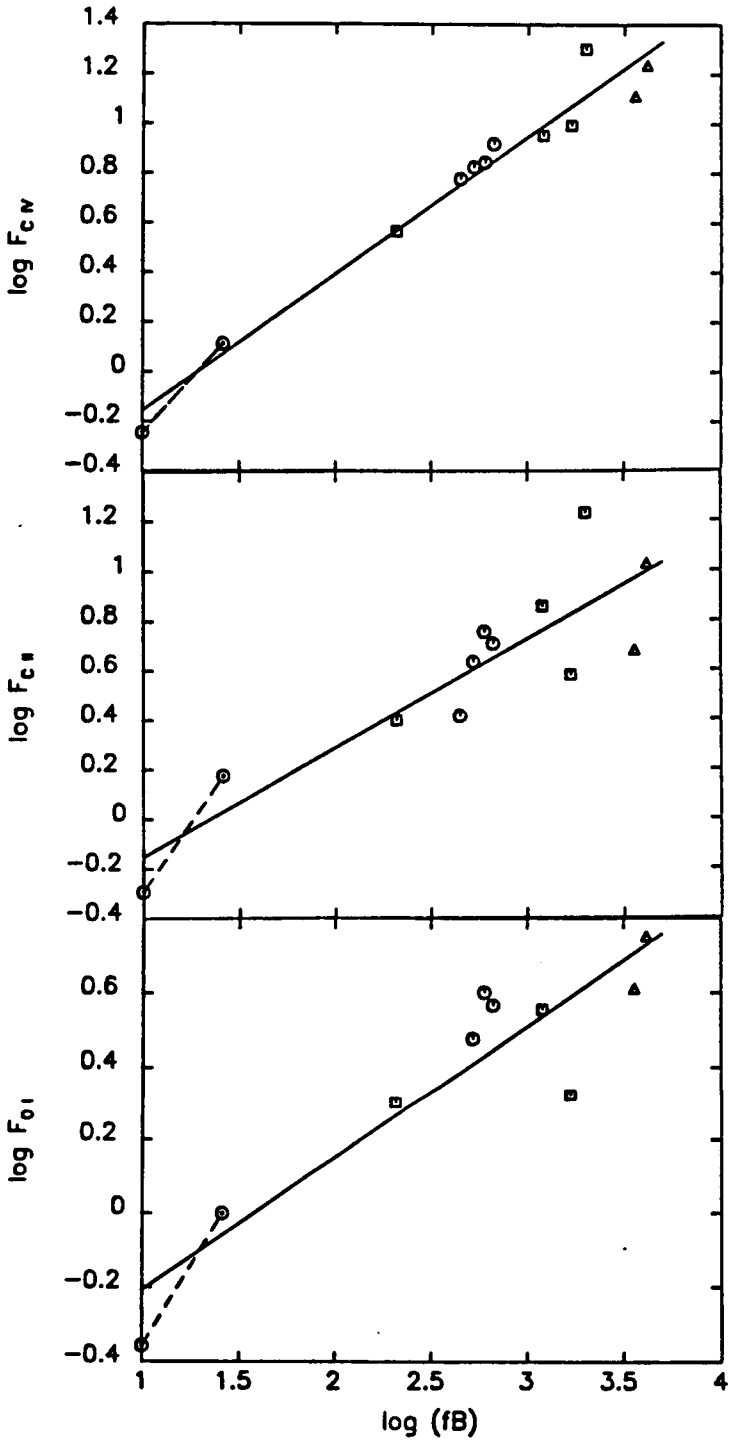

Figure 3: IUE emission line surface flux densities vs. magnetic flux density. The solid lines are the power law fits $F_{CIV} \propto (fB)^{0.55}$, $F_{CII} \propto (fB)^{0.44}$, and $F_{OI} \propto (fB)^{0.36}$. Data for the quiet and active Sun are connected by dashed lines. Symbols as in Figure 1.

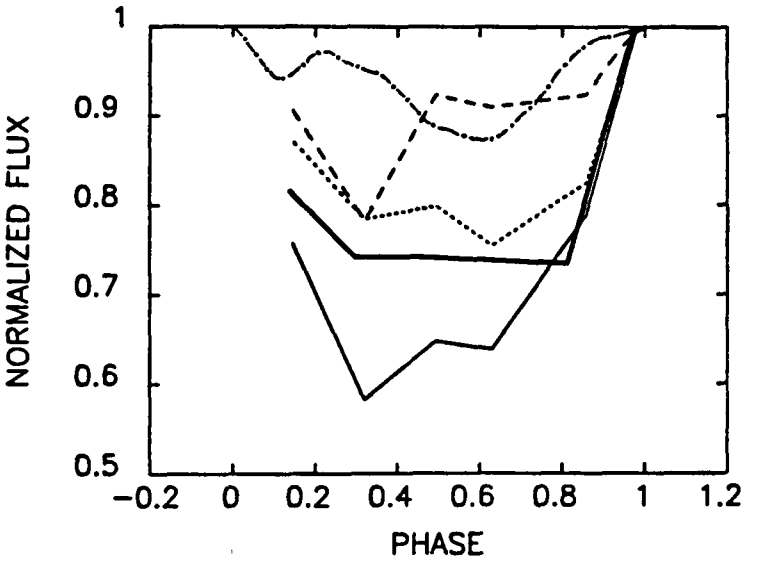

Figure 4: The magnetic flux ($\propto$ fB, heavy solid), various ultraviolet emission line fluxes (C IV, solid; C II, dashed; O I, long dashed) and the smoothed, Ca II excess flux (dash-dotted) of ξ Bootis A, normalized and plotted versus rotational phase.

known orbital axis (at 78°) of the ξ Boo A+B system.

The amplitude of P_L measures the *net* tangential component of the magnetic field and is maximized when significant magnetic flux is distributed asymmetrically, near the stellar limb (e.g., Landi Degl'Innocenti 1982). The combination of the variation of fB (weighted towards *disk-center* regions because of projection and limb-darkening effects) with the amplitude of P_L therefore contains positional information, which Saar *et al.* (1987) used to construct a crude "magnetic image" of ξ Boo A. Using more sophisticated modeling, we hope to map the active region geometry of ξ Boo, which, when combined with the radiative and magnetic fluxes as a function of phase, will allow us for the first time to derive realistic, two-component (quiet + active) models for an outer atmosphere of a solar-like star.

This research was funded in part by the Smithsonian Institution Center Fellowship program and by NASA grant NAGW-112. Much of the research described was done while the author was a Postdoctoral Research Associate at the Joint Institute for Laboratory Astrophysics in Boulder, Colorado. Work there was supported by NASA grant NGL-06-003-057 to the University of Colorado. It is a pleasure to thank the National Optical Astronomy Observatories for ample telescope time and travel support.

REFERENCES

Baliunas, S. L. 1986, in *The Fourth Cambridge Workshop on Cool Stars, Stellar Systems, and the Sun*, eds. M. Zeilik and D. M. Gibson (New York: Springer-Verlag), p. 3.

Basri, G. S., and Marcy, G. W. 1988, *Ap. J.*, submitted.

Borra, E. F., Edwards, G., and Mayor, M. 1984, *Ap. J.*, 284, 211.

Durney, B. R., and Robinson, R. D. 1982, *Ap. J.*, **253**, 290.
Gondoin, Ph., Giampapa, M. S., and Bookbinder, J. 1985, *Ap. J.*, **297**, 710.
Gray, D. F. 1984, *Ap. J.*, **277**, 640.
Gray, D. F. 1985, *Pub. A. S. P.*, **97**, 719.
Hartmann, L. W., and Noyes, R. W. 1987, *Ann. Rev. Astr. Ap.*, **25**, 271.
Landi Degl' Innocenti, E. 1982, *Astr. Ap.*, **110**, 25.
Linsky, J. L. 1985, *Solar Phys.*, **100**, 333.
Linsky, J. L., and Saar, S. H. 1987, in *The Fifth Cambridge Workshop on Cool Stars, Stellar Systems, and the Sun*, in press.
Mangeney, A., and Praderie, F. 1984, *Astr. Ap.*, **130**, 143.
Marcy, G. W. 1982, *Pub. A. S. P.*, **94**, 989.
Marcy, G. W. 1984, *Ap. J.*, **276**, 286.
Marcy, G. W., and Bruning, D. H. 1984, *Ap. J.*, **281**, 286.
Noyes, R. W., Hartmann, L., Baliunas, S. L., Duncan, D. K., and Vaughan, A. H. 1984, *Ap. J.*, **279**, 793.
Noyes, R. W., Weiss, N. O., and Vaughan, A. H. 1984, *Ap. J.*, **287**, 769.
Oranje, B. J. 1983, *Astr. Ap.*, **124**, 43.
Pallavicini, R., Golub, L., Rosner, R., Vaiana, G. S., Ayres, T., and Linsky, J. L. 1981, *Ap. J.*, **248**, 279.
Robinson, R. D. 1980, *Ap. J.*, **239**, 961.
Saar, S. H. 1988, *Ap. J.*, Jan. 1.
Saar, S. H., Huovelin, J., Giampapa, M. S., Linsky, J. L., and Jordan, C., 1987, in *Activity in Cool Star Envelopes*, in press.
Saar, S. H., and Linsky, J. L. 1986, *Advances in Space Physics*, **6**, No. 8, 235.
Saar, S. H., Linsky, J. L., and Giampapa, M. S. 1987, in Proc. of *27th Liegé International Astrophysics Colloquium on Observational Astrophysics with High Precision Data*, in press.
Saar, S. H., and Schrijver, C. J. 1987, in *The Fifth Cambridge Workshop on Cool Stars, Stellar Systems, and the Sun*, in press.
Schrijver, C. J. 1983, *Astr. Ap.*, **127**, 289.
Schrijver, C. J. 1987a, *Astr. Ap.*, **172**, 111.
Schrijver, C. J. 1987b, in press.
Schrijver, C. J., and Coté, J. 1987, in *The Fifth Cambridge Workshop on Cool Stars, Stellar Systems, and the Sun*, in press.
Schrijver, C. J., and Rutten, R. G. M. 1987 *Astr. Ap.*, **177**, 143.
Simon, T., and Fekel, F. 1987, *Ap. J.*, **316**, 434.
Skumanich, A. 1972, *Ap. J.*, **171**, 565.
Soderblom, D. R. 1983, *Ap. J. Suppl.*, **53**, 1.
Ulmschneider, P., and Stein, R. F. 1982, *Astr. Ap.*, **106**, 9.
Vilhu, O. 1984, *Astr. Ap.*, **133**, 117.
Vogt, S. S. 1983, in *Activity in Red Dwarf Stars*, eds. P. B. Byrne and M. Rodonó (Dordrecht: Reidel), p. 137.

Theoretical Analysis of the Polarization and Harmonic Structure of Solar Radio Spikes

Guangli Huang
Harvard-Smithsonian Center for Astrophysics

November 1988

Abstract

In this paper the effects of the parameter ω_{pe}/Ω_e on the electron cyclotron maser instabilities are calculated. The range of this parameter is divided into several parts to discuss the polarization sense and degree of the solar radio spikes. Five possibilities for the harmonic structure of radio spikes are predicted (the frequency ratio is about 1:2 or 2:3). The conclusions of this paper are compared with the relevant observations.

1. Introduction

As a fine structure of solar activity and a direct signature of energetic particles in solar flares the observations of solar radio spikes have been studied by many scientists (Melrose, 1984; Sharma *et al.*, 1984; Vlahos *et al.*, 1985; Li, 1986, 1987; Huang, 1987, 1988a,b). The theory of the electron cyclotron maser instability seems to be a reasonable model for explaining the millisecond radio spikes in the decimetric range (Benz, 1986). Many observational characteristics of radio spikes are consistent with the predictions of this theory. For instance, the high brightness temperature of the radio spikes is connected with the high growth rates of the electron cyclotron maser instability , and because the electron cyclotron maser instability is a resonant wave-particle interaction in velocity space, the band-width of the radio spikes is very narrow, and the directionality of spike emissions is very strong.

Some aspects need further theoretical consideration, such as the polarization and the harmonic structure of radio spikes. The purpose of this paper is to explain these important properties by the electron cyclotron maser instability theory.

In Section 2, the effects of ω_{pe}/Ω_e on the electron cyclotron maser instability are discussed and calculated. The polarization of the electron cyclotron maser instability is discussed in Section 3. The possibilities for the harmonic structure in the radio spikes are predicted in Section 4. Section 5 is a summary.

2.The Effects of the Parameter ω_{pe}/Ω_e on the electron cyclotron maser instability

The formula for the growth rates of the electron cyclotron maser instability was given by Wu (1985) for the hollow beam distribution of the non-thermal electrons

$$\omega_i = \sum_{n=1}^{\infty} \Gamma_n, \tag{1}$$

$$\Gamma_n = -4\pi^2 \frac{\omega_{pe}^2}{G\omega_r^2} \frac{n\Omega_e}{N\cos\theta} \frac{c^4}{\alpha_\perp^2} \int_{u_-^{(n)}}^{u_+^{(n)}} du_\parallel \Big(\frac{n\Omega_e}{\omega_r} \frac{u_n - u_{0\perp}}{c} +$$

$$+ \frac{u_n}{c} \frac{\alpha_\perp^2}{\alpha_\parallel^2} N\cos\theta \frac{u_\parallel - u_{0\parallel}}{c}\Big) F_s(u_n, u_\parallel)\Big[(\psi_{xx} + \psi_{xy} + \psi_{yy}) +$$

$$+ \frac{k_\perp^2 u_\parallel^2}{n^2\Omega_e^2}\psi_{zz} + \frac{k_\perp u_\parallel}{n\Omega_e}(\psi_{xz} - \psi_{yz})\Big] \frac{n}{b_n} J_n^2(b_n) - (2\psi_{yy} + \psi_{xy} -$$

$$- \frac{k_\perp u_\parallel}{n\Omega_e}\psi_{yz}) J_n(b_n) J_{n+1}(b_n) + \frac{b_n}{n}\psi_{yy} J_{n+1}^2(b_n)\Big], \tag{2}$$

$$\frac{u_\pm^{(n)}}{c} = \frac{N\cos\theta}{1 - N^2\cos^2\theta}\Big\{\frac{n\Omega_e}{\omega_r} \pm \Big[1 + \frac{1}{N^2\cos^2\theta}\Big(\frac{n^2\Omega_e^2}{\omega_r^2} - 1\Big)\Big]^{1/2}\Big\}, \tag{3}$$

$$F_s(u_\perp, u_\parallel) = \frac{\exp(-\xi_0^2)}{1 + \xi_0 Z(\xi_0)} (\pi\alpha_\perp^2)^{-1} (\pi\alpha_\parallel^2)^{-1/2} \times$$

$$\times \exp\Big[-\frac{(u_\parallel - u_{0\parallel})^2}{\alpha_\parallel^2} - \frac{(u_\perp - u_{0\perp})^2}{\alpha_\perp^2}\Big]. \tag{4}$$

Here, ω_i and ω_r are the imaginary and the real parts of the frequency, where it is assumed that $\omega_i \ll \omega_r$. ω_{pe} and Ω_e are the electron plasma and cyclotron frequencies, respectively. N is the refractive index, $k_\perp$ and $k_\parallel$ are the vertical and horizontal wave-vectors, θ is the angle between the propagation vector and the magnetic field. $J_n(b_n)$ is the usual Bessel function of order n. $\xi_0 = -iu_{0\perp}/\alpha_\perp$, Z is the plasma dispersion function, $u_{0\parallel}$ and $u_{0\perp}$ are the bulk flow momentum parallel and vertical to the magnetic field, $\alpha_\parallel$ and $\alpha_\perp$ denote the characteristic momentum spreads. In addition,

$$\frac{u_n}{c} = [-(1 - N^2\cos^2\theta)\frac{u_\parallel^2}{c^2} + 2\frac{n\Omega_e}{\omega_r}\frac{u_\parallel}{c}N\cos\theta + (\frac{n^2\Omega_e^2}{\omega_r^2} - 1)]^{1/2},$$

$$\psi_{xx} = N^4\sin^4\theta - N^2(\varepsilon\sin^2\theta + \eta) + \varepsilon\eta,$$

$$\psi_{yy} = -N^2(\varepsilon\sin^2\theta + \eta\cos^2\theta) + \varepsilon\eta,$$

$$\psi_{zz} = N^4\cos^2 - N^2\varepsilon(1 + \cos^2\theta) + \varepsilon^2 - g^2,$$

$$\psi_{xz} = 2N^2(N^2 - \varepsilon)\sin\theta\cos\theta,$$

$$\psi_{xy} = 2g(\eta - N^2\sin^2\theta),$$

$$\psi_{yz} = 2N^2 g\sin\theta\cos\theta,$$

$$G = 2N^4[(1-\varepsilon)^2\frac{\sin^2\theta}{1-\eta} + (1-\eta)\cos^2\theta] +$$

$$+ 4N^2[(1-\varepsilon)^2 - 1 - (1 + 0.5\sin^2\theta)\frac{g^2}{1-\eta}] +$$

$$+ 2[(1+\eta)\varepsilon^2 - g^2 + 2\eta^2\frac{(1-\varepsilon)^2}{1-\eta}],$$

$$\varepsilon = 1 - \frac{\omega_{pe}^2}{\omega_r^2 - \Omega_e^2},$$

$$g = \frac{\omega_{pe}^2\Omega_e}{\omega_r^3 - \omega_r\Omega_e^2},$$

$$\eta = 1 - \frac{\omega_{pe}^2}{\omega_r^2}.$$

It is noted that there are two basic parameters of the ambient magnetized plasma: the electron density n_e and the intensity of the magnetic field B_0. It is easy to show that the growth rates of electron cyclotron maser instability depend only on the ratio of ω_{pe} and Ω_e, or the ratio of $n_e^{1/2}$ and B_0.

From the formula for the cut-off frequencies in a "cold" plasma (Kong *et al.*, 1982),

$$\frac{\omega_0^{(1)}}{\Omega_e} = (\frac{\omega_{pe}^2}{\Omega_e^2} + 0.25)^{1/2} + 0.5 \quad (Fast\ Extraordinary\ Modes), \tag{5}$$

$$\frac{\omega_0^{(2)}}{\Omega_e} = \frac{\omega_{pe}}{\Omega_e} \quad (Ordinary\ Modes), \tag{6}$$

it is evident, that the lower harmonics will be suppressed gradually with increasing ω_{pe}/Ω_e.

The question is how to choose the range of ω_{pe}/Ω_e for the calculation of the growth rates of the electron cyclotron maser instability . It is supposed that solar spikes are mainly composed of the second harmonics of Ω_e. And the intensity of the ambient magnetic field is estimated as 50-500 Gauss corresponding to the decimetric range (300-3000 MHz). The average value of n_e in a solar active region is about $10^9\ cm^{-3}$ (Mclean, 1986) so the value of ω_{pe}/Ω_e should be in the range of 0.2-2.

On the other hand, the value of the plasma β in the low corona is about 10^{-4} (Dulk et al., 1978) and

$$\beta = \frac{2n_e kT_e}{B_0^2/2\mu},$$

$$= \frac{\omega_{pe}^2}{\Omega_e^2}\frac{4kT_e}{m_e c^2}. \tag{7}$$

Here k is the Bolzhman constant, T_e is the electron temperature, μ is the magnetic permeability, and c is the velocity of light.

With $T_e \simeq 10^6 K$, $4kT_e/m_e c^2 \sim 10^{-4}$, and $\omega_{pe}/\Omega_e \sim 1$, this value is consistent with the estimates in the above paragraph. The calculations for the growth rates of the electron cyclotron maser instability at the first and second harmonics of the fast extraordinary and ordinary modes are shown in Figures 1-4. It is evident from these figures that:

1. All harmonics of all modes can only be excited in a respective range of ω_{pe}/Ω_e. With increasing ω_{pe}/Ω_e, the growth rates of the electron cyclotron maser instability vary non-monotonically (there is one maximum of the growth rates for each curved line).

2. The range of ω_{pe}/Ω_e for the fundamentals of the fast extraordinary modes is from 0.2 to 0.5 (Fig.1); for the second harmonics of the extraordinary modes this range is from 0.5 to 1.3 (Fig.2); for the fundamentals of the ordinary modes from 0.4 to 0.95 (Fig.3); for the second harmonics of the ordinary modes from 0.5 to 1.7 (Fig.4).

3. The range of ω_{pe}/Ω_e can be divided into several parts: For the values between 0.2 and 0.5, there are only the fundamentals of the fast extraordinary modes to be excited; for the values between 0.5 and 0.9, the fundamentals of ordinary modes and the second harmonics of the fast extraordinary modes are both excited; for the values between 0.9 and 1.2, the growth rates of the second harmonics of the fast extraordinary modes are one order of magnitude higher than that of the second harmonics of the ordinary modes; for the values between 1.2 and 1.7, there are only the second harmonics of the ordinary modes to be excited; beyond that, the third harmonics of the fast extraordinary modes and the ordinary modes will be excited gradually.

These results are very useful for the discussion of the polarization and the harmonic structure of solar radio spikes.

3. Polarization

The polarization of solar radio spikes is observed by Benz (1982, 1987), but it is not discussed in theoretical detail. In fact this property can be explained directly by the electron cyclotron maser instability theory.

According to Mclean (1986) the polarization degree is defined as:

$$p = \frac{T_{BR} - T_{BL}}{T_{BR} + T_{BL}}. \tag{8}$$

Here, p is the polarization degree (%), T_{BR} is the brightness temperature of the right-hand circular components, T_{BL} is the brightness temperature of the left-hand circular components.

On the other hand, the solutions of the "cold" plasma dispersion equation (Wu, 1985) are:

$$\Lambda_0(\vec{k},\omega) = AN^4 + BN^2 + C = 0, \tag{9}$$

$$N_{\pm}^2 = \frac{-B \pm \sqrt{B^2 - 4AC}}{2A}, \tag{10}$$

$$A = \varepsilon \sin^2\theta + \eta \cos^2\theta, \tag{11}$$

$$B = -\varepsilon\eta(1+\cos^2\theta) - (\varepsilon^2 - g^2)\sin^2\theta, \tag{12}$$

$$C = \eta(\varepsilon^2 - g^2). \tag{13}$$

Here N_+ and N_- are the refractive index of the ordinary and the extraordinary waves respectively. It is easy to show that the left-hand circular (right-hand circular) waves and the ordinary modes (the fast extraordinary modes) correspond to the same refractive index. This result is consistent with the 'Leading Spot Rule' (Benz, 1987). If the growth rate of electron cyclotron maser instability is constant during the rise-time of a single spike, then the formula for the polarization degree can be written as

$$p = \frac{T_{BX} - T_{BO}}{T_{BX} + T_{BO}},$$

$$= \frac{e^{\omega_{ix}\Delta\tau} - e^{\omega_{io}\Delta\tau}}{e^{\omega_{ix}\Delta\tau} + e^{\omega_{io}\Delta\tau}}. \tag{14}$$

Here, T_{BX}, T_{BO} are the brightness temperature of the extraordinary and the ordinary waves, respectively, $\Delta\tau$ is the duration of the rise time of a single spike, and the resonance absorption is neglected in this formula. Because the growth rates of the electron cyclotron maser instability are different for different values of ω_{pe}/Ω_e, on the basis of the calculation in Section 2, the range of ω_{pe}/Ω_e can be divided into several parts to analyze the polarization degree.

When the value of ω_{pe}/Ω_e is from 0.2 to 0.5, there are only the fundamentals of the fast extraordinary modes with right-hand circular polarization and the polarization degree p is very high (up to 100%). But, when ω_{pe}/Ω_e is larger than 0.4, the growth rates of the fundamentals of the ordinary modes will increase gradually, which will result in a decreasing p.

When the value of ω_{pe}/Ω_e is from 0.5 to 0.95, there are only the fundamentals of the ordinary modes with the left-hand circular polarization and the p-value is up to 100%.

When the value of ω_{pe}/Ω_e is from 0.5 to 1.3, both the fast extraordinary and the ordinary modes at the second harmonic may be excited, but the growth rates of the former are four to five times larger than that of the latter. If the value of ω_{pe}/Ω_e is larger than 1.1, the differences between these two modes decrease gradually, and the polarization degree of the right-hand circular will vary from 75% to 15%.

When the value of ω_{pe}/Ω_e is from 1.3 to 1.7, the second harmonics of the fast extraordinary modes will be suppressed rapidly, and the second harmonics of the ordinary modes decay slowly. Hence, the polarization sense will be changed into the left-hand circular, and the polarization degree will increase from 0 to 100% with the decrease of intensity of the ambient magnetic field.

The high circular polarization in some observations of solar radio spikes (Benz, 1986) can be explained by the fundamental emmisions of the fast extraordinary modes, which propagate at a small angle θ and the resonant absorptions are very weak (Huang, 1987). More recent measurements (Benz *et al.*, 1982; Stähli *et al.*, 1986; Nomino *et al.*, 1986) agree that the polarization of solar radio spikes can vary from 0 to 100% with left-hand or right-hand circular senses at different frequencies, which may be correspond to different values of ω_{pe}/Ω_e in the sources of radio spikes. It is interesting to find the polarization sense sometimes changing from left circular to right circular (Benz *et al.*, 1982). A possible explanation is that when the electron beam propagates along the open magnetic field lines, with the decrease of the value of ω_{pe}/Ω_e, the fast extraordinary modes will be suppressed gradually instead of the ordinary modes (Figures 1-4).

On the other hand, from the measurements of the polarization sense and degree of the radio spikes, the value of ω_{pe}/Ω_e (also the plasma density) in the sources of spikes can be estimated directly.

4. Harmonic Structure

The harmonic events of solar radio spikes have been observed by Benz (1987), Stähli *et al.* (1986), and Yun Nan Observatory of the Academia Sinica (Xie *et al.*, 1987). However, the theory of the harmonic structure is still unsolved. The author indicated (1987), that the first and the second harmonics of the fast extraordinary modes cannot be observed in the same direction, because their θ-values are quite different (Fig.5). From the calculations in Section 2, the harmonic structures of radio spikes can be excited in several regions of ω_{pe}/Ω_e:

When the value of ω_{pe}/Ω_e is from 0.53 to 0.92, and the θ-value is about 70°, the growth rates of the ordinary modes at the first harmonic and the fast extraordinary modes at the second harmonic have similar magnitude. So it is possible to observe the harmonic structure of the frequency ratio 1:2. Their

polarization senses are opposite, and the amplitude of the fundamentals is larger than that of the second harmonics. But, when the value ω_{pe}/Ω_e is larger than 0.8, the amplitude of the second harmonics will exceed that of the fundamentals (Fig.6).

When the value of ω_{pe}/Ω_e is from 0.91 to 0.97, and the angle θ is about 80°, it is possible to receive both the fundamentals and the second harmonics of the ordinary modes with the same polarization sense (left-hand circular), and the frequency ratio is about 1:2 (Fig. 7).

When the value of ω_{pe}/Ω_e is from 1.3 to 1.35, the extraordinary modes at the second and the third harmonics may be observed in the same direction (θ is about 80°) with the frequency ratio 2:3 and right-hand circular polarization (Fig. 8).

When the value of ω_{pe}/Ω_e is between 1.7 and 1.9, the second and third harmonics of the ordinary modes also can be received at an angle θ of about 70° (2:3 and left-hand) (Fig. 9).

When the value of ω_{pe}/Ω_e is between 1.5 and 2.0, the ordinary modes at the second harmonic and the extraordinary modes at the third harmonic may be observed with the opposite polarization sense and the directional angle θ is about 70° (Fig.10).

There are three reasons why it is not very easy to observe the harmonic structure of the solar radio spikes: 1. The range of ω_{pe}/Ω_e is very narrow for the harmonic events. 2. The range of the directional angle θ is also very narrow (often much smaller than ten degrees). 3. Because the harmonic events can only be received at a large value of the angle θ, the resonance absorptions are very strong.

The properties of the harmonic structures of radio spikes observed by the Yun Nan Observatory can be explained by the emissions of the fundamentals of the ordinary modes and the second harmonics of the fast extraordinary modes, whose frequency ratio, amplitude ratio and directional angle are consistent with the observations (Xie, *et al.* 1987). The harmonic structures with the frequency ratio of 1 : 1.39 and left circular polarization (Benz, 1987) can be explained by the emmisions of the second and third harmonics of the ordinary modes (Figure 9).

5. Summary

In this paper, the effects of the parameter ω_{pe}/Ω_e on the electron cyclotron maser instability are emphasized and calculated, which is the basis of the discussion of the polarization and the harmonic structure of the solar radio spikes. The polarization properties (including the sense and the degree) are analyzed in several regions of ω_{pe}/Ω_e. A high right-hand circular polarization (up to 100%) exists in the range from 0.2 to 0.5 (the fundamendals of the fast extraordinary modes). A high left-hand circular polarization (up to 100%) exists in the range from 0.5 to 0.95 (the fundamentals of the ordinary modes). A middle right-hand circular polarization (75% to 15%) exists in the range from 0.5 to 1.3 (the fast extraordinary and the ordinary modes at the second harmonics). A middle left-hand circular polarization (0 to 100%) exists in the range from 1.3 to 1.7 (the second harmonics of the ordinary modes).

Finally the possibilities for the harmonic structure are predicted in five separate regions of ω_{pe}/Ω_e: The harmonic events of the frequency ratio 1:2 may be observed between 0.53 to 0.92 at $\theta \approx 70°$ with the opposite polarization (the left-hand circular for the fundamentals, and the right-hand circular for the second harmonics), and between 0.91 and 0.97 with the same left- hand circular polarization at $\theta \approx 80°$. There are three possibilities for the frequency ratio 2:3, the first is 1.3 to 1.35 at $\theta \approx 70°$ with the same right-hand circular polarization; the second is from 1.7 to 1.9 at $\theta \approx 70°$ with the same left-hand circular polarization; the third is from 1.5 to 2.0 at $\theta \approx 70°$ with the opposite polarization sense (the left-hand circular polarization for the second harmonics, the right-hand circular polarization is for the third harmonics). But, because the ranges of ω_{pe}/Ω_e and θ are both limited and the resonance absorptions are very strong, the harmonic structures are not often observed.

Acknowledgements

I would like to thank the Smithsonian Astrophysical Observatory for awarding me a Predoctoral grant, and Dr. P. Martens for helpful discussions and language editing, I also thank Dr. H.D. Tananbaum and Dr. H.W. Li for the useful comments. Studies of coronal plasma processes at the Harvard-Smithsonian Center for Astrophysics are supported by NASA grant NAGW-112.

References

Benz, A.O.: 1986, *Solar Physics* 101, 99.

Benz, A.O. and Güdel, M.: 1987, *Solar Physics* 111, 175.

Benz, A.O.: 1982; *Astron. Astrophs.* 109, 305.

Dulk, G.A. and Mclean, D.J.: 1978, *Solar Physics* 57, 279.

Huang, G.L.: 1987, *Solar Physics* 114, 363.

Huang, G.L.: 1988a, *Advances in Space Research* (in press).

Huang, G.L.: 1988b, *Publications of Purple Mountain Obs.* (in press).

Kong, S.W. and Chen, Y.P.: 1982, *"Handbook of Plasma Physics"*, Academia Sinica Press.

Li, H.W.: 1986, *Solar Physics* 104, 131.

Li, H.W.: 1987, *Solar Physics* 111, 167.

Mclean, D.J. (ed): 1986, *"Solar Radiophysics"*, Oxford press, London.

Melrose, D.B.: 1982, *Astrophys. J.* 259, 844.

Nomino, M., Abrami,A., Comari, M., Messerrotti, M. and Zlobec, P.: 1986, Solar Physics 104, 111.

Sharma, A.R. and Vlahos, L.: 1984, *Astrophys. J.* 280, 405.

Stähli, M. and Magun, A.: 1986, *Solar Physics* 104, 117.

Vlahos, L. and Sharma. A.R.: 1984, *Astrophys. J.* 290, 347.

Wu, C.S.: 1985, *Space Science Rew.* 41, 215.

Xie, R.X., Yang K.P., Li W.H., Chen G.Q., Ji, S.C., Ma Y., Zhang F. and Zao R.S.: 1987, *Chinese Solar-Geophysical Data* 7, 33.

Figure Captions

Figure 1: The relation of growth rates of the fundamentals of the fast extraordinary modes and ω_{pe}/Ω_e , θ. ($u_0/c = 0.5$, $\alpha = 40°$, $\alpha_\perp = \alpha_{||} = 0.2$, α is a pitch angle between the beam and magnetic field.In the following figures these beam parameters are the same)

Figure 2: The relation of growth rates of the second harmonics of the fast extraordinary modes and ω_{pe}/Ω_e , θ.

Figure 3: The relation of growth rates of the fundamentals of the ordinary modes and ω_{pe}/Ω_e , θ.

Figure 4: The relation of growth rates of the second harmonics of the ordinary modes and ω_{pe}/Ω_e , θ.

Figure 5: The comparison of growth rates of the fundamentals and second harmonics of the fast extraordinary modes.

Figure 6: The comparison of growth rates of the fundamentals of the ordinary modes and the second harmonics of the fast extraordinary modes ($\theta \approx 70°$).

Figure 7: The comparison of growth rates of the fundamentals and second harmonics of the ordinary modes ($\theta \approx 80°$).

Figure 8: The comparison of growth rates of the second harmonics and third harmonics of the fast extraordinary modes ($\theta \approx 70°$).

Figure 9: The comparison of growth rates of the second harmonics and third harmonics of the ordinary modes ($\theta \approx 70°$).

Figure 10: The comparison of growth rates of the second harmonics of the ordinary modes and the third harmonics of the fast extraordinary modes ($\theta \approx 70°$).

fig 1

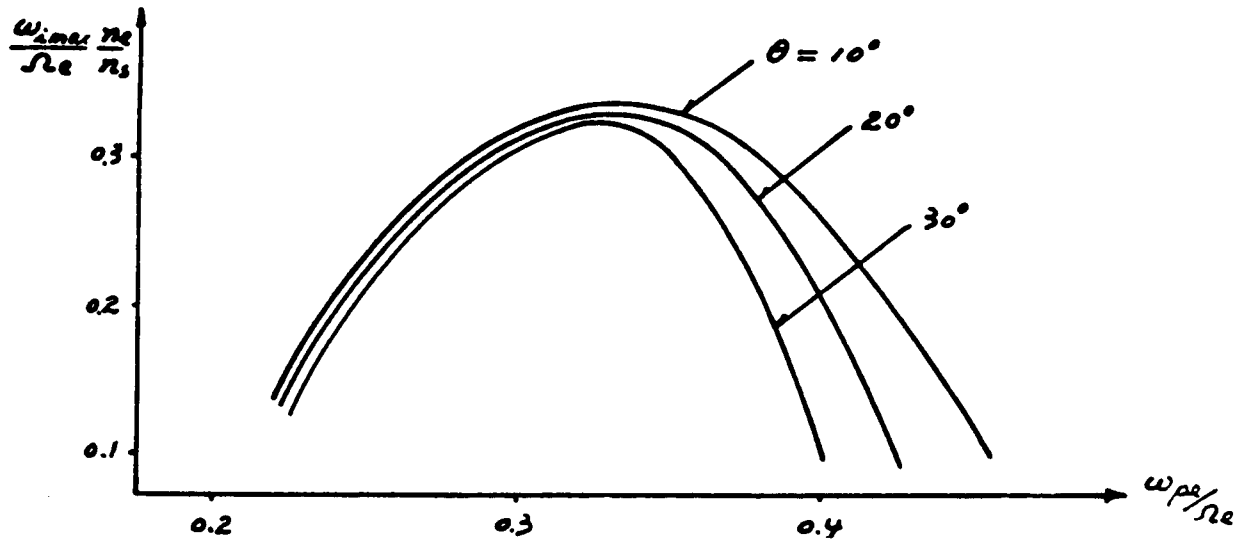
$\frac{\omega_{imag}}{\Omega_e}\frac{n_e}{n_s}$
0.3
0.2
0.1
θ = 10°
20°
30°
0.2
0.3
0.4
ω_{pe}/Ω_e

fig 2

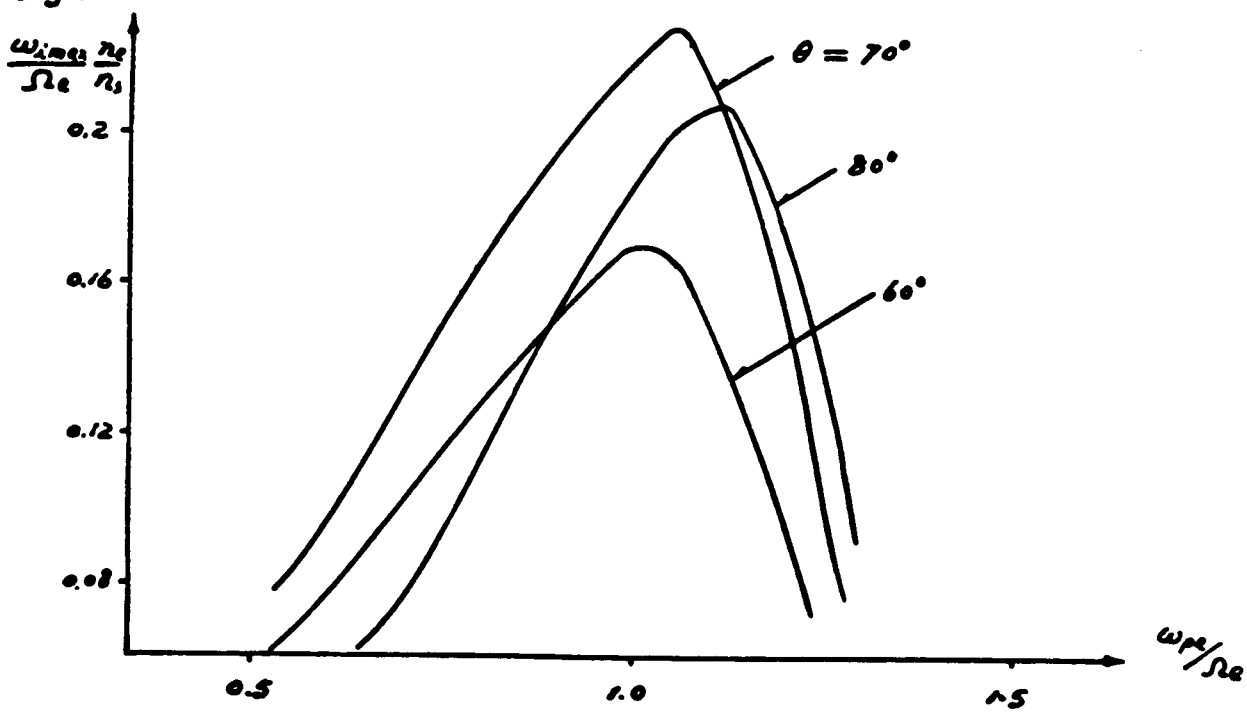
$\frac{\omega_{imag}}{\Omega_e}\frac{n_e}{n_s}$
0.2
0.16
0.12
0.08
θ = 70°
80°
60°
0.5
1.0
1.5
ω_{pe}/Ω_e

fig 3

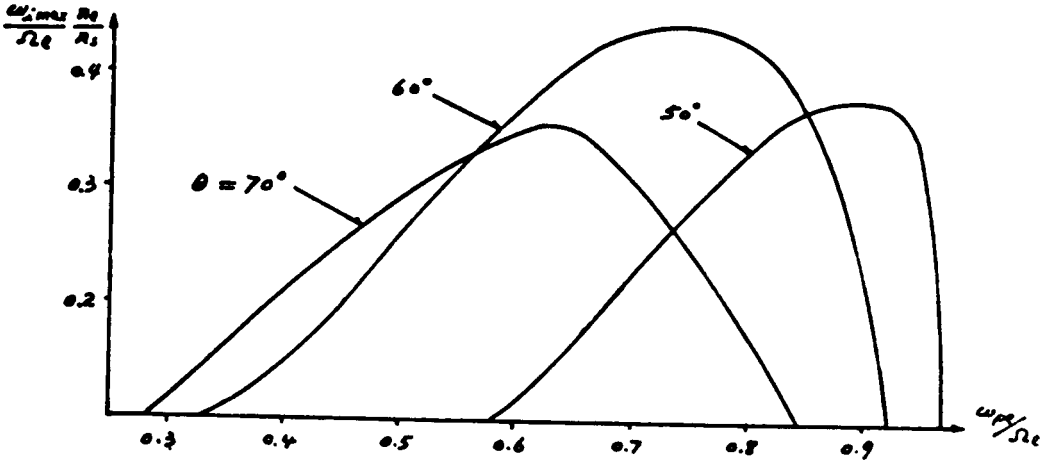

fig 4

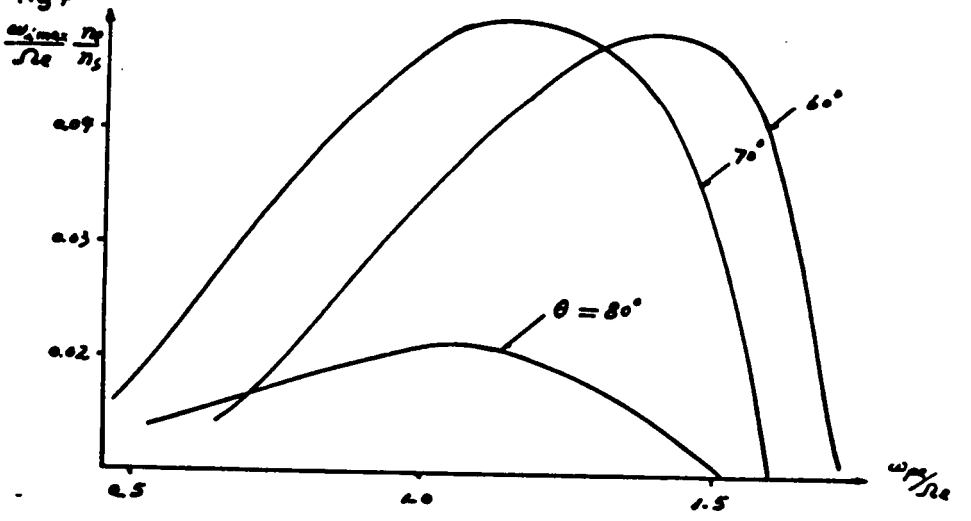

fig 5

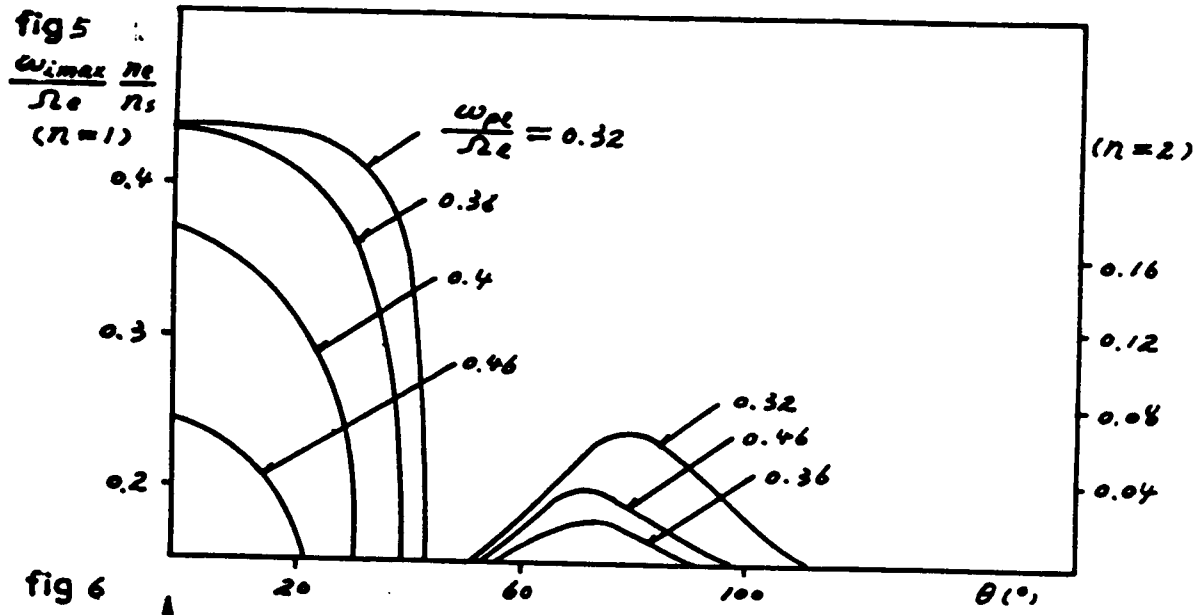

fig 6

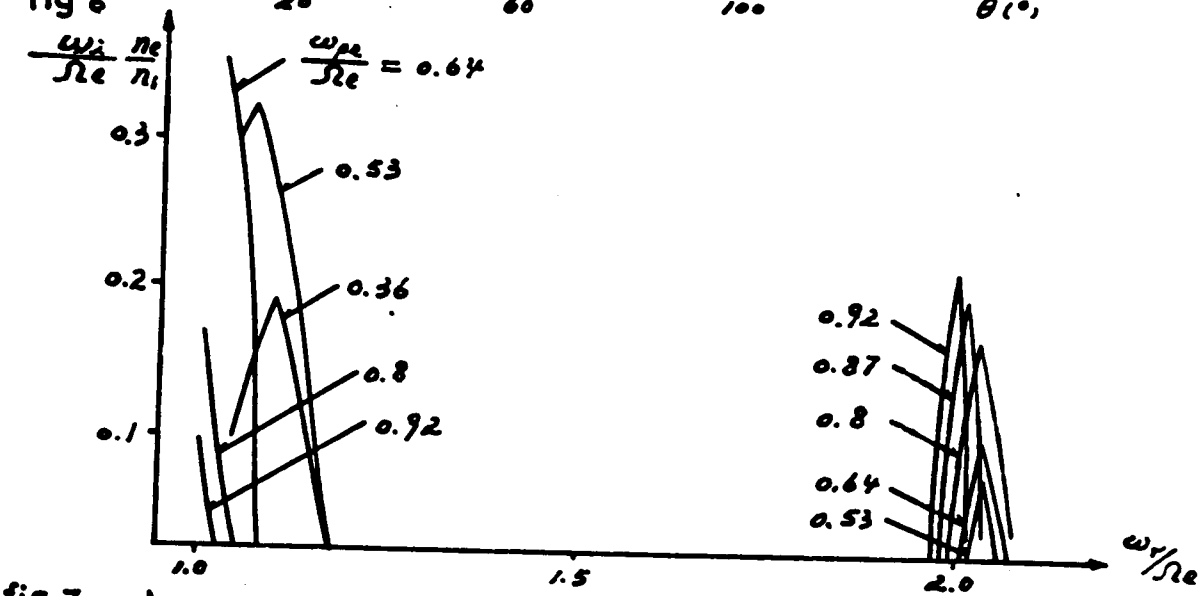

fig 7

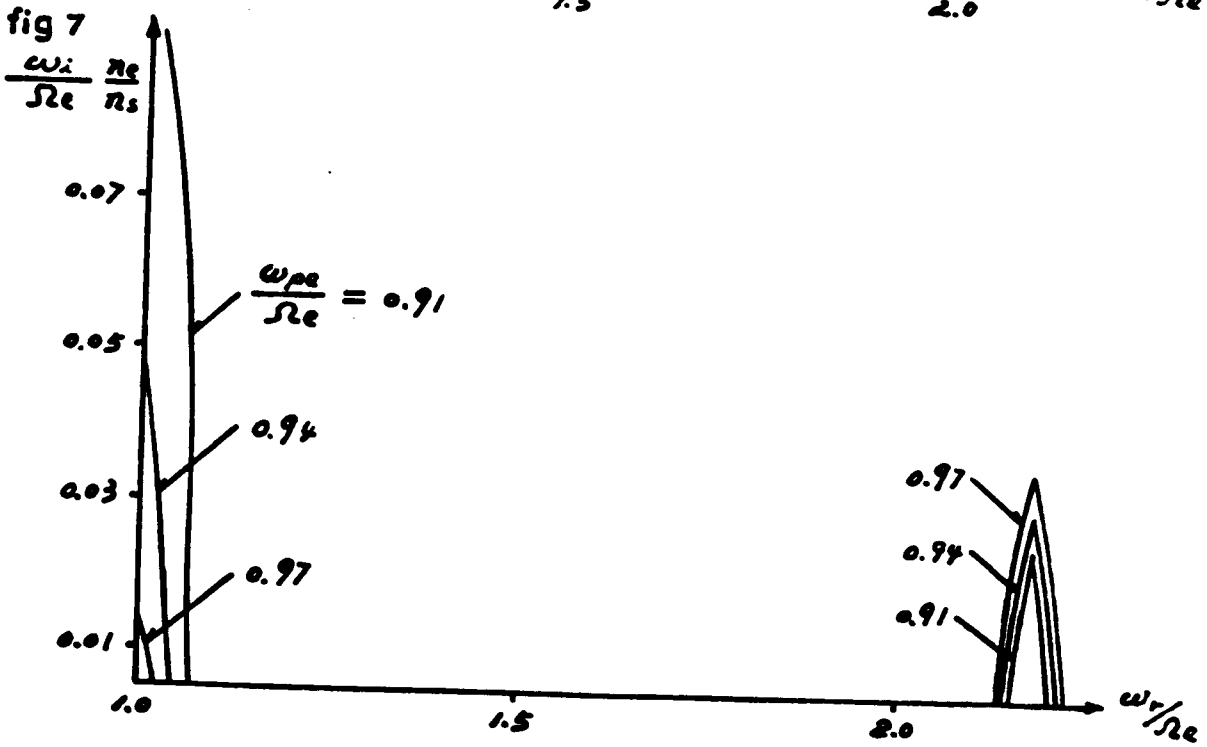

fig 8

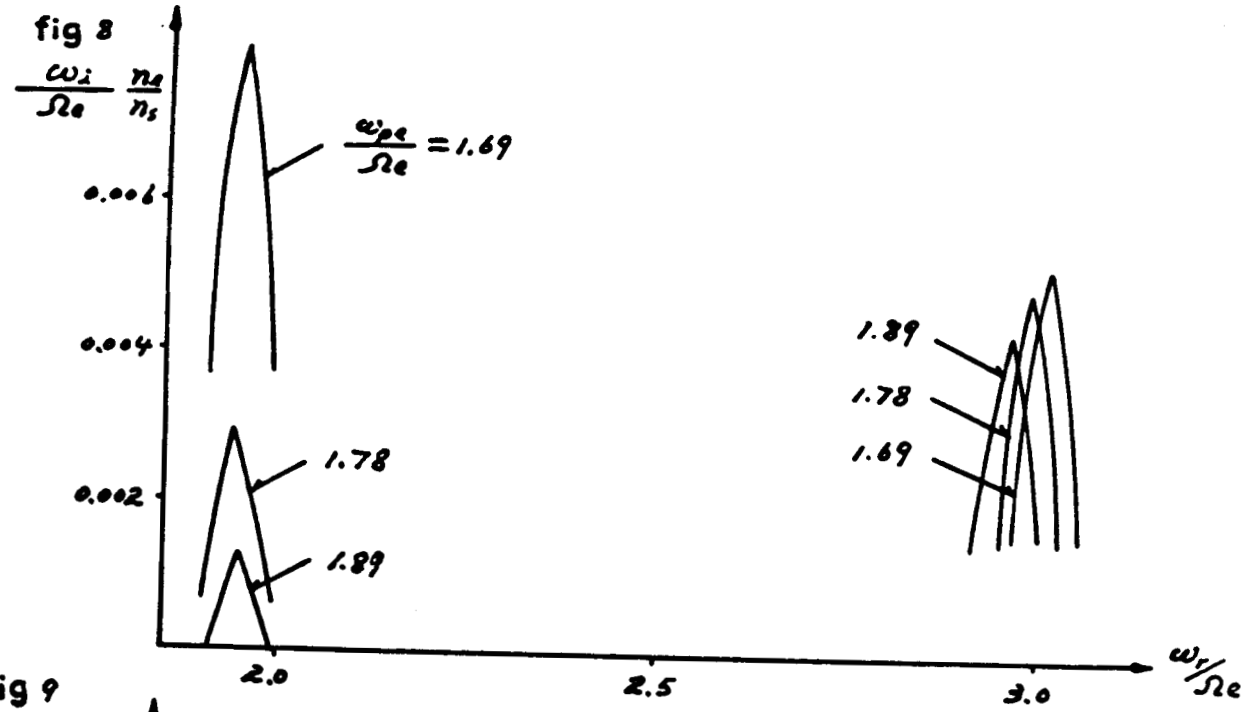

fig 9

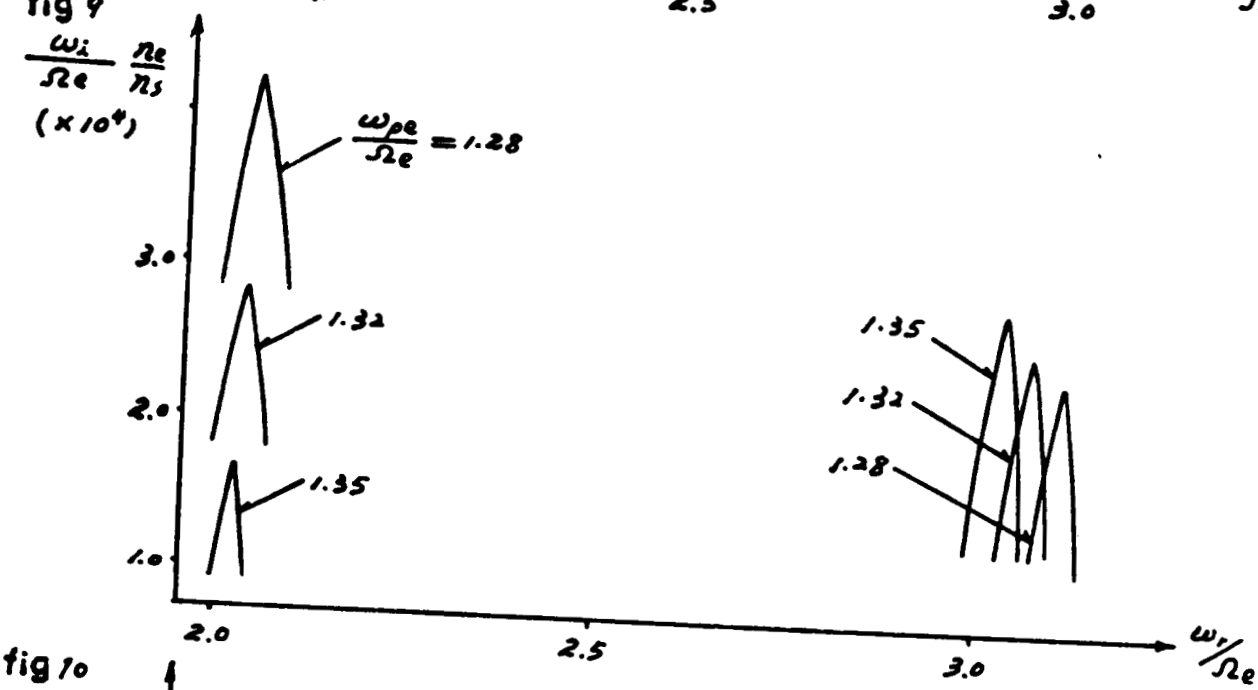

fig 10

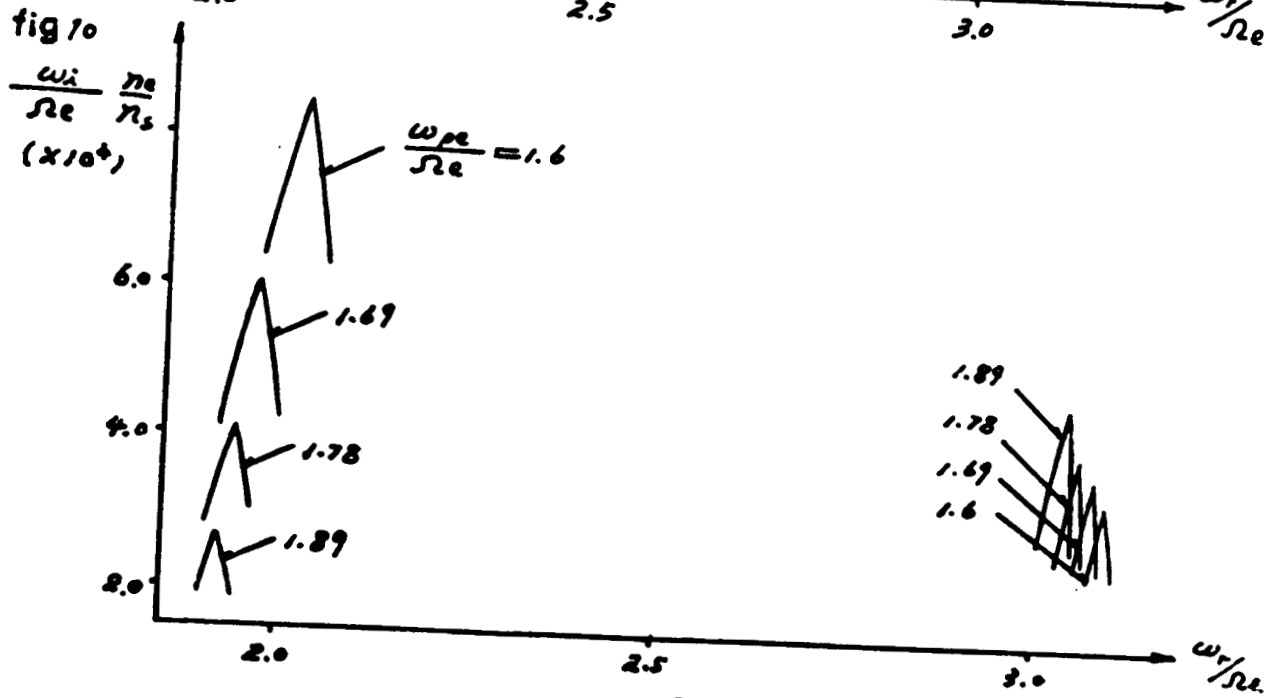

The Growth of Alfven Waves in a Current-Driven Instability and a Comparison with the Tearing Mode Instability

Guangli Huang
Harvard-Smithsonian Center for Astrophysics

November 1988

Abstract

The classical theory of the tearing mode instability is discussed and a formula for the growth rate of Alfven waves is derived from the dispersion relation for a magnetized plasma, in which the plasma resistivity and the electric current along the ambient magnetic field are both considered. The growth rates are directly proportional to the plasma resistivity, the electric current density and a parameter ω_{pe}/Ω_e. Moreover, the growth of Alfven waves can only be excited in a direction nearly parallel to the ambient magnetic field, and the velocity of the electron fluid (related to the electric current) should be larger than the Alfven velocity. Therefore Alfven waves and tearing modes are similar physical phenomena.

1. Introduction

The tearing mode instability is one of the most important large-scale MHD instabilities. As the prime phenomenon and exciting mechanism in the disruptive instabilities in tokamaks, the tearing modes have attracted wide attention (Kadomtsev, 1984). In plasma astrophysics, the tearing mode may also play an important role in the magnetic energy conversion and particle acceleration in solar flares (Priest, 1983).

The classical theory of the tearing mode instabilities was established by

Furth *et al.* in 1963. Because of the shear in the magnetic field and the periodic boundary condition, the tearing modes can be excited only in a narrow boundary layer of the corresponding rational magnetic surface. So the WKB approximation is used: the resistivity of plasma is considered only in the boundary layer and the ideal MHD equations remain valid in the other regions. Hence the growth rates of the tearing modes are derived from the continuity boundary condition.

The classical theory has been developed further over the years: from the plane slab to the cylindrical and toroidal coordinates, from the linear theory to the non-linear theory, from the analytical model to numerical calculations. However, some questions remain open:

1) Bateman (1982) derived the same result for the growth rates of the tearing modes as in the classical theory (Furth *et al.*, 1963) using a very simple model without solving any boundary problem.

2) In the classical theory, the imaginary parts of the eigenvalues are neglected. However, the imaginary parts of eigenvalues describe a periodic oscillation of the tearing modes, and the real parts of the eigenvalues describe the exponential growth of the amplitude of the oscillation. The periodicity of the tearing modes is proven by the author (1987, 1988) from the imaginary parts of the eigenvalues in MHD equations and the real parts of the eigenvalues are consistent with the exponential growth rates in the classical theory of tearing modes (Furth *et al.*, 1963).

The quasi-periodicity of the tearing modes was shown directly in the disruptions in tokamak plasma (Shunji Tsuji, 1983). The evolution of solar radio spikes is also explained by the quasi-periodicity of the induced electric field of the tearing modes (Huang, 1988).

3) The source of free energy for the growth of tearing modes in a toroidal plasma is the toroidal electric current along the ambient magnetic field. However, this relation is not shown in the formula for the growth rates of the tearing modes in the classical theory.

4) In fact, the resistive boundary layer is not a clear physical boundary and its width depends on the properties of tearing modes, which makes the growth rates of tearing modes vary with the evolution of the tearing modes themselves, so the growth rates in the classical theory of tearing modes are not the strict eigenvalues (a strict eigenvalue is a constant without any dependence on the solutions).

5) The anomalous growth of the tearing modes has not been explained very satisfactorily and it is often considered to be the result of the interaction between different modes. However, the author has shown that the anomalous growth of tearing modes is an inevitable result of the growth of normal tearing modes, even for a single mode (Huang, 1987).

In this paper the author is concerned in the questions 1-4. Question 5 will be discussed in a forthcoming paper. In Section 2 the growth rates of the Alfven waves in a current-driven instability are derived from the plasma dispersion relation. In Section 3 the growth rates of the Alfven waves are compared with the classical theory of the tearing mode instability. Section 4 is a summary.

2. Growth Rates of the Alfven Waves

2.1 Physical Analysis

Because of the periodicity of the tearing modes, there must be a corresponding electromagnetic wave in the dispersion relation of the plasma. Note that tearing modes have a long wavelength or a low frequency and their phase velocity is of the same order of magnitude as the Alfven velocity (Huang, 1987, 1988). Therefore the growth of the tearing modes may be related to the excitation of the Alfven waves, which attract the free energy of the electric current of a magnetized plasma. Moreover, the growth of the tearing modes only takes place in a boundary layer, which is much smaller than the characteristic length of non-uniformity of plasma and much larger than the Debye length of plasma. So it is possible to use the method of solving the dispersion equation of a uniform plasma.

Note that there is no dissipation mechanism in the "cold" plasma dispersion relation, so its dispersion tensor is a complex symmetric tensor and its eigenvalues will be real. When the resistivity and the electric current of the plasma are both considered in the MHD equations, the dispersion tensor of the plasma will have an antisymmetric part and its eigenvalues will have an imaginary part.

2.2 Derivation of Growth Rates

Initially the effect of ion motions is neglected, and the momentum equation for the electron fluid is:

$$n_e m_e \frac{d\vec{V}}{dt} = -en_e(\vec{E} + \frac{\vec{V} \times \vec{B}}{c}) + \vec{R}. \tag{1}$$

Here $\vec{V}$ is the velocity of the electron fluid related the background ions, n_e is the density of electrons and m_e is the mass of an electron. The collisional term $\vec{R}$ is defined as

$$\vec{R} = en_e\eta_0\vec{J} \quad (\vec{J} = -en_e\vec{V}). \tag{2}$$

Here η_0 is the resistivity of plasma.

Let $\vec{V} = \vec{V_0} + \vec{V_1}$, $\vec{B} = \vec{B_0} + \vec{B_1}$ and $\vec{E} = \vec{E_0} + \vec{E_1}$ and it is easy to write down the expansion of Equation (1)

$$\vec{E_0} + \frac{\vec{V_0} \times \vec{B_0}}{c} = \eta_0\vec{J_0}, \tag{3}$$

$$m_e \frac{d\vec{V_1}}{dt} = -e(\vec{E_1} + \frac{\vec{V_1} \times \vec{B_0}}{c} + \frac{\vec{V_0} \times \vec{B_1}}{c}) - e^2 n_e \eta_0 \vec{V_1}. \tag{4}$$

Equation (3) is simply the generalized Ohm's law. Working out Eq. (4) yields

$$\frac{\vec{V_0} \times \vec{B_1}}{c} = \vec{V_0} \times \frac{c\vec{k}}{\omega_r} \times \vec{E_1}$$

$$= \mathbf{A} \cdot \frac{\vec{E_1}}{\omega_r}, \tag{5}$$

$$\mathbf{A} = \begin{pmatrix} 0 & -V_{0z} & V_{0y} \\ V_{0z} & 0 & -V_{0x} \\ -V_{0y} & -V_{0x} & 0 \end{pmatrix} \begin{pmatrix} 0 & -k_z & k_y \\ k_z & 0 & -k_x \\ -k_y & k_x & 0 \end{pmatrix}. \tag{6}$$

When $\vec{V_0} = V_0\hat{z}$ and $\vec{k} = k_x\hat{x} + k_z\hat{z}$, the tensor $\mathbf{A}$ can be divided into two parts, a symmetric tensor and an antisymmetric tensor

$$\mathbf{A} = \mathbf{A_1} + \mathbf{A_2}$$

$$= \begin{pmatrix} -k_{\|}V_0 & 0 & k_{\perp}V_0/2 \\ 0 & -k_{\|}V_0 & 0 \\ k_{\perp}V_0/2 & 0 & 0 \end{pmatrix} + \begin{pmatrix} 0 & 0 & k_{\perp}V_0/2 \\ 0 & 0 & 0 \\ -k_{\perp}V_0/2 & 0 & 0 \end{pmatrix}. \tag{7}$$

Take the Fourier transform of Equation (4) (Melrose, 1982):

$$(\omega\delta_{ij} + i\Omega_e\varepsilon_{ijk}b_k)V_{1j} = -ie/m_e(\delta_{ij} + A_{ij})E_{1j}. \tag{8}$$

Here, $\omega = \omega_r + i\omega_0$, $\omega_0 = e^2 n_e \eta_0/m_e$, $\Omega_e = \frac{eB_0}{m_e c}$, $\vec{B_0} = B_0\hat{b}$, the Levi-Civita symbol ε_{ijk} is defined as:

$$\varepsilon_{ijk} = \begin{cases} 1 & \text{when } (i,j,k) \text{ is an even permutation} \\ -1 & \text{when } (i,j,k) \text{ is an odd permutation} \\ 0 & \text{when two of } i,j,k \text{ are of the same value} \end{cases}$$

Let

$$(\omega\delta_{ij} + i\Omega_e\varepsilon_{ijk}b_k)C_{jl} = \omega_r\delta_{il},$$

the dielectric tensor of the plasma can be derived from (7)

$$D_{ij} = \delta_{ij} - \frac{\omega_{pe}^2}{\omega_r^2}C_{il}(\delta_{lj} + A_{lj}), \tag{9}$$

$$\omega_{pe}^2 = \frac{4\pi n_e e^2}{m_e},$$

$$\mathbf{C} = \begin{pmatrix} \frac{\omega^2}{\omega^2-\Omega_e^2} & \frac{-i\omega\Omega_e}{\omega^2-\Omega_e^2} & 0 \\ \frac{i\omega\Omega_e}{\omega^2-\Omega_e^2} & \frac{\omega^2}{\omega^2-\Omega_e^2} & 0 \\ 0 & 0 & 1 \end{pmatrix}. \tag{10}$$

The tensor $\mathbf{C}$ can also be divided into a symmetric and an antisymmetric part,

$$\mathbf{C} = \mathbf{C}_1 + \mathbf{C}_2$$

$$= \begin{pmatrix} \frac{\omega_r^2}{\omega_r^2-\Omega_e^2} & \frac{-i\omega_r\Omega_e}{\omega_r^2-\Omega_e^2} & 0 \\ \frac{i\omega_r^2\Omega_e^2}{\omega_r^2-\Omega_e^2} & \frac{\omega_r^2}{\omega_r^2-\Omega_e^2} & 0 \\ 0 & 0 & 1 \end{pmatrix} +$$

$$+ \frac{i2\omega_r\omega_0}{\omega_r^2 - \Omega_e^2}\begin{pmatrix} 1 & 0 & 0 \\ 0 & 1 & 0 \\ 0 & 0 & 0 \end{pmatrix}. \tag{11}$$

Under the approximations $\omega_i \ll \omega_r$, $D_{ij}^a \ll D_{ij}^h$ (ω_i and ω_r are the real and the imaginary parts of the frequency, D_{ij}^a and D_{ij}^h are the antisymmetric

and the symmetric components of the dielectric tensor, respectively), it can be proven (Melrose, 1982)

$$\frac{\omega_i}{\omega_r} = \frac{-Im(\Psi \cdot \mathbf{D})}{G}, \tag{12}$$

$$G = \omega_r \frac{\partial \Lambda_0}{\partial \omega_r}. \tag{13}$$

Here $\Lambda_0 = det(\mathbf{D})$, and $\Psi \cdot \mathbf{D} = \Lambda_0 \mathbf{I}$, $\mathbf{I}$ is the unit tensor. For the "cold" plasma model (Wu, 1985)

$$\Psi_{xx} = N^4 \sin^2\theta - N^2(\varepsilon \sin^2\theta + \eta) + \varepsilon\eta,$$

$$\Psi_{yy} = -N^2(\varepsilon \sin^2\theta + \eta\cos^2\theta) + \varepsilon\eta,$$

$$\Psi_{zz} = N^4 \cos^2\theta - N^2\varepsilon(1 + \cos^2\theta) + \varepsilon^2 - g^2,$$

$$\Psi_{xz} = 2N^2(N^2 - \varepsilon)\sin\theta\cos\theta = \Psi_{zx},$$

$$\Psi_{yz} = i2N^2 g \sin\theta\cos\theta = -\Psi_{zy},$$

$$\Psi_{xy} = i2g(\eta - N^2\sin^2\theta) = -\Psi_{yx},$$

$$G = 2N^4[(1-\varepsilon)^2\frac{\sin^2\theta}{1-\eta} + (1-\eta)\cos^2\theta] +$$

$$4N^2[(1-\varepsilon)^2 - \frac{g^2(1+0.5\sin^2\theta)}{1-\eta} - 1] +$$

$$2[\varepsilon^2(1+\eta) - g^2 + \frac{2\eta^2(1-\varepsilon)^2}{1-\eta}].$$

Here, $\varepsilon = 1 - \frac{\omega_{pe}^2}{\omega_r^2 - \Omega_e^2}$, $g = \frac{\omega_{pe}^2\Omega_e}{\omega_r(\omega_r^2 - \Omega_e^2)}$, $\eta = 1 - \frac{\omega_{pe}^2}{\omega_r^2}$, N is the refractive index, θ is the angle between the magnetic field and the wave-vector.

From (9), (7) and (11), it is evident, that $\mathbf{C}_1 \cdot \mathbf{A}_2$ has no effect on the antisymmetric part of the dielectric tensor, so

$$\mathbf{D}^a = -\frac{\omega_{pe}^2}{\omega_r^3}\mathbf{C}_2 \cdot (\mathbf{I} + \mathbf{A}_1),$$

$$= i\lambda \begin{pmatrix} 1 - \frac{k_z V_0}{\omega_r} & 0 & \frac{k_z V_0}{2\omega_r} \\ 0 & 1 - \frac{k_z V_0}{\omega_r} & 0 \\ 0 & 0 & 0 \end{pmatrix}, \tag{14}$$

$$\lambda = -\frac{2\omega_r\omega_0}{\omega_r^2 - \Omega_e^2}\frac{\omega_{pe}^2}{\Omega_e^2}. \tag{15}$$

Then with (14) and (15) the formula for the growth rates can be written as

$$\frac{\omega_i}{\omega_r} = \frac{\lambda}{G}[(\Psi_{xx} + \Psi_{yy})(\frac{k_z V_0}{\omega_r} - 1) - o.5\frac{k_x V_0}{\omega_r}\Psi_{xz}]. \tag{16}$$

For Alfven waves $N = \frac{c}{V_A \cos\theta}$, and $\omega_r \ll \Omega_e$, Ω_i. When $\theta = 0$ the wave-vector is parallel to the magnetic field, and formula (14) can be simplified to

$$\frac{\omega_i}{\omega_r} = \frac{e^2 n_e \eta_0}{m_e \omega_r}\frac{\omega_{pe}^2}{\Omega_e^2}\frac{1}{N^2}(\frac{k_z V_0}{\omega_r} - 1), \tag{17}$$

$$= \frac{e\eta_0 J_0}{m_e \omega_r V_A}\frac{\omega_{pe}^2}{\Omega_e^2}\frac{V_A^2}{c^2}(1 - \frac{V_A}{V_0}). \tag{18}$$

When $\theta = \pi/2$, or $k_{||} = 0$

$$\frac{\omega_i}{\omega_r} = -\frac{e^2 n_e \eta_0}{m_e \omega_r}\frac{\omega_{pe}^2}{\Omega_e^2}\frac{1}{N_2} < 0. \tag{19}$$

It can be proven that ω_i is a monotonic function of the angle θ between $0 - \pi/2$.

3. Conclusions

1) From Equation (17), when $\eta_0 = 0$, it follows that $\omega_i = 0$, which means that the growth rate of the Alfven waves depends on the resistivity of plasma. This result is consistent with the theory of tearing mode instabilities.

2) From Equation (17), when $V_0 = 0$ or $J_0 = 0$, the growth rates will be negative, hence an electric current along the magnetic field is a basic condition of the growth for the Alfven waves. The tearing mode instabilities also depend on the electric current.

3) From Equation (16) or (18), the growth rate is positive only when Alfven waves propagate nearly parallel to the magnetic field.

4) From Equation (17), $\omega_i \propto \frac{\omega_{pe}}{\Omega_e}$, which means that the growth of the Alfven waves is suppressed gradually with increasing magnetic field or decreasing plasma density.

5) From Equation (17), the Alfven waves of the lower frequencies are most easily excited.

6) The criterion for the growth of the Alfven waves can be derived from (16) or (17)

$$V_0 > \frac{\omega_r}{k_z} \approx V_A, \tag{20}$$

which means that the velocity of the electron fluid (corresponding to the electric current) should be larger than the phase velocity of the Alfven waves along the direction of the magnetic field. Otherwise the background plasma will attract the free energy of eletromagnetic waves, which is similar to Landau damping. In the classical theory for the tearing modes (Furth *et al.*, 1963) this criterion is the following

$$\Delta' = \frac{J_{z1} k \varepsilon}{B_{x1}} > 0. \tag{21}$$

Here ε is the width of boundary layer. In fact this criterion means that the direction of perturbed electric current should be opposite to the direction of the toroidal electric current.

Note that Δ' is related to the perturbed parameters, hence it cannot be determined by the basic parameters of the plasma.

7) For the typical parameters of a tokamak plasma, ω_i can be estimated from Equation (17): if $B_0 \sim 1T$, $n_e \sim 10^{19}\ m^{-3}$ ($\omega_{pe}/\Omega_e \sim 1$), $T_e \sim 1Kev$, $V_A \sim 10^6\ m/sec$, $J_0 \sim 10^6\ A/m^2$, then, $\omega_i \sim 10^1 - 10^2/sec$. This order of magnitude is comparable with the experiments in tokamaks. In the corona the intensity of electric current can not be measured directly. In typical solar coronal conditions, $n_e \sim 10^{15} m^{-3}$, $B_0 \sim 10^{-2} T$, $T_e \sim 10^6 K$, so $V_A \sim 10^6\ m/sec$ and $\omega_{pe}/\Omega_e \sim 1$ (the similar order as in a typical tokamak plasma). The intensity of the electric current in a model coronal current sheet is about $10^3 A/m^2$ (Martens, 1988), so the value of ω_i is from 10^0 to 10^1. The resistivity of the plasma is estimated by the Spitzer's formula.

8) Because the Alfven time is an important time scale, the growth of Alfven waves may be used to explain many phenomena, such as the quasi-periodic oscillations of the solar radio spikes. The author will study this subject in a forthcoming paper.

A Kinetic Formula for Cyclotron Resonance Absorption Coefficients

Guangli Huang

Harvard-Smithsonian Center for Astrophysics

February 8, 1989

Abstract

The classical theory of cyclotron resonance absorption is discussed in this paper. An approximate formula for the cyclotron resonance absorption coefficients is derived from plasma kinetic theory. Finally, the main properties of resonance absorption are calculated: the absorption coefficients increase rapidly with increasing θ, the directional angle between the magnetic field and the wave-vector, and their values are directly proportional to the electron temperature T_e and ω_{pe}/Ω_e.

1. Introduction

The theory of cyclotron resonance absorption is an important part of solar radiophysics. Especially solar radio spikes have attracted wide attention these years and the electron cyclotron maser instabilities are today's most favoured mechanism for explaining millisecond radio spikes (Benz, 1986; Melrose, 1984; Vlahos et al., 1985; Li, 1986; Huang, 1987). But the question remains, which modes of the electromagnetic waves can penetrate through the corona and will be observed by us? This depends mainly on the magnitude of cyclotron resonance absorption, and there are some different opinions on this problem (Melrose, 1984; Sharma et al., 1984; Huang, 1987).

The classical theory of cyclotron resonance absorption has been established by Stepanov (1958), Gershman (1959, 1960), Zheleznyakov (1973), and Ginzburg (1978). The formula that is often used in astrophysics is derived by Zheleznyakov (1973), using the single-particle model and Kirchhoff's Law.

As Ginzburg pointed out (1978), Kirchhoff's Law can only be used when matter and radiation are in complete thermal equilibruim. When a system is unstable (or the waves are amplified), Kirchhoff's Law may be used under the condition of weak absorption or amplification of the waves, in fact it

is only proper for the states in which the emission equals the sum of the emissions of all particles.

But cyclotron resonance absorption is a strong collective plasma effect, so the proper treatment is to solve the the kinetic equations (Vlasov's and Maxwell's equations). Stepanov (1958) and Gershman (1959, 1960) derived the kinetic-theory formulae, which can only be used near the regions of resonance. The deviation of the frequency should be smaller than the Doppler shift by the thermal motions of the electrons, so this is not absorption under the strict resonant condition. In their derivations, the frequency is always assumed to be real, and the wave-vector a complex vector, the imaginary part of the wave-vector is derived from the plasma dispersion relation and is defined as the absorption coefficient.

In practice the cyclotron resonance absorption is a wave-particle resonant interaction in the velocity space, the dimension of which is characterized by the Debye Length of the plasma, and it is often much smaller than the characteristic length of the plasma uniformity. So the dissipative process of electromagnetic waves in a uniform plasma system can only be discussed by the imaginary part of the frequency and the group velocity. In a very non-uniform plasma, it is difficult to define the group velocity, and the resonance

absorption should be studied by solving a boundary value problem for the kinetic equations (Ginzburg, 1978).

On the other hand, when the wave-vector is assumed be a real vector and the frequency is complex, for given wave-vector (including the wavelength and directional angle), the real and imaginary parts of the frequency will be found self-consistently from the dispersion equation. In the opposite case (Stepanov, 1958; Gershman, 1959, 1960), the real and imaginary parts of the wave-vector should be assumed in the same direction, but this condition is not reasonable for an anisotropic plasma.

The author has derived a formula for cyclotron resonance absorption, using the theory of cyclotron maser instability, to explain millisecond radio spikes (Huang, 1987). This formula will be simplified further to discuss the properties of the cyclotron resonance absorption systematically. In Section 2 the kinetic-theory formula for absorption coefficients is derived and simplified. The properties of resonance absorption are discussed in Section 3. Section 4 is a summary.

2. Derivation

2.1 Physical Analysis

Cyclotron resonance absorption is a non-collisional absorption mechanism, it means a dissipative process of electromagnetic waves under a resonant condition. The free energy of the electromagnetic waves is absorbed by the ambient electrons, which often have a Maxwellian distribution in the velocity space. If the ambient electrons have an anisotropic distribution, it will result in the opposite process, the electron cyclotron maser instability.

Therefore, if the Maxwellian distribution function is used in the formula for the growth rates of the electron cyclotron maser instabilities (Wu, 1985), instead of the non-thermal distribution of the electrons, the imaginary part of the frequency will be negative, which corresponds to the resonance absorption coefficient.

2.2 Derivation

With the approximations $\omega_i \ll \omega_r$ and $D^a_{ij} \ll D^h_{ij}$ (ω_i and ω_r are the imaginary and real parts of the frequency, D^a_{ij} and D^h_{ij} are the symmetric and anti-symmetric components of the plasma dielectric tensor), the exponen-

tial decay rates of different modes of the electromagnetic waves in a 'cold' plasma dispersion relation by cyclotron resonance absorption can be found directly from the formula of Wu (1985):

$$\omega_i = \sum_{n=1}^{\infty} \Gamma_n, \tag{1}$$

$$\frac{\Gamma_n}{\Omega_e} = -\frac{4\pi^2}{G}\frac{\omega_{pe}^2}{\omega_\tau^2}\frac{c^4}{\alpha^5}\int_{u_-^{(n)}}^{u_+^{(n)}} du_{||}\frac{u_n^2}{c^2}(n + \frac{k_{||}u_{||}}{\Omega_e}) \times \exp(-\frac{u_n^2}{\alpha^2})\exp(-\frac{u_{||}^2}{\alpha^2})$$

$$\{[(\psi_{xx} + \psi_{yy} + \psi_{xy})n^2 + (\psi_{xz} - \psi_{yz})nb_{||} + \psi_{zz}b_{||}^2]\frac{J_n^2(b_n)}{b_n^2} -$$

$$- [(2\psi_{yy} + \psi_{xy})n - \psi_{yz}b_{||}]\frac{J_n(b_n)}{b_n}J_{n+1}(b_n) + \psi_{yy}J_{n+1}^2(b_n)\}. \tag{2}$$

Here $b_n = \frac{k_\perp u_n}{\Omega_e}$, $b_{||} = \frac{k_\perp u_{||}}{\Omega_e}$, $\alpha^2 = \frac{2T_e}{m_e}$, ω_{pe} and Ω_e are the electron plasma and cyclotron frequencies respectively, c is the velocity of light, T_e is the average electron temperature, m_e is the mass of a single electron, $k_\perp$ and $k_{||}$ are the vertical and horizental wave-vector. In addition,

$$\frac{u_n}{c} = [-(1 - N^2\cos^2\theta)\frac{u_{||}^2}{c^2} + 2n\frac{\Omega_e}{\omega_\tau}\frac{u_{||}}{c}N\cos\theta + (\frac{n^2\Omega_e^2}{\omega_\tau^2} - 1)]^{1/2},$$

$$\frac{u_\pm^{(n)}}{c} = \frac{N\cos\theta}{1 - N^2\cos^2\theta}\{\frac{n^2\Omega_e^2}{\omega_\tau^2} \pm [1 + \frac{1}{N^2\cos^2\theta}(\frac{n^2\Omega_e^2}{\omega_\tau^2} - 1)]^{1/2}\},$$

$$\psi_{xx} = N^4\sin^4\theta - N^2(\varepsilon\sin^2\theta + \eta) + \varepsilon\eta,$$

$$\psi_{yy} = -N^2(\varepsilon\sin^2\theta + \eta\cos^2\theta) + \varepsilon\eta,$$

$$\psi_{zz} = N^4\cos^2\theta - N^2\varepsilon(1 + \cos^2\theta) + \varepsilon^2 - g^2,$$

$$\psi_{xz} = 2N^2(N^2 - \varepsilon)\sin\theta\cos\theta,$$

$$\psi_{xy} = 2g(\eta - N^2\sin^2\theta),$$

$$\psi_{yz} = 2N^2 g\sin\theta\cos\theta,$$

$$G = 2N^4[(1-\varepsilon)^2\frac{\sin^2\theta}{1-\eta} + (1-\eta)\cos^2\theta] +$$

$$+4N^2[(1-\varepsilon)^2 - 1 - (1 + 0.5\sin^2\theta\frac{g^2}{1-\eta}] +$$

$$+2[(1+\eta)\varepsilon^2 - g^2 + 2\eta^2\frac{(1-\varepsilon)^2}{1-\eta}].$$

Here $\varepsilon = 1 - \frac{\omega_{pe}^2}{\omega_r^2 - \Omega_e^2}$, $g = \frac{\omega_{pe}^2\Omega_e}{\omega_r^2 - \omega_r\Omega_e^2}$, $\eta = 1 - \frac{\omega_{pe}^2}{\omega_r^2}$, N is the refractive index and θ is an angle between the propagation vector and the magnetic field.

3.3 Non-relativistic approximation

In the corona a typical value of T_e is $10^6 K$, hence the thermal velocity $V_e \sim 0.01c$, and the relativistic factor $\gamma \sim 1$. So the resonant condition is simplified to

$$\frac{u_{\|}}{c} = \frac{\omega_r - n\Omega_e}{\omega_r N\cos\theta}. \tag{3}$$

From the intgral formula (Wang et al., 1979)

$$\int_0^\infty \exp(-p^2t^2)J_k(at)J_l(bt)t^{i+1}dt =$$

$$= \frac{a^{k+l}}{2^{k+l}p^{i+k+l}}\frac{\Gamma(\frac{i+k+l}{2})}{\Gamma(k+1)\Gamma(l+1)}\times$$

$$\times\, {}_3F_3\left(\frac{k+l+1}{2}, \frac{k+l+2}{2}, \frac{i+k+l}{2}; k+1, l+1, k+l+1; -\frac{a^2}{p^2}\right).$$

(4)

Therefore, Equation (2) can be written as

$$\frac{\Gamma_n}{\Omega_e} = -\frac{4\pi^{1/2}}{G}\frac{\omega_{pe}^2}{\omega_r^2}\frac{c^2}{\alpha^5}\left(n + \frac{k_{||}u_{||}}{\Omega_e}\right)\exp\left(-\frac{u_{||}^2}{\alpha^2}\right)\times$$

$$\times\{[(\psi_{xx} + \psi_{yy} + \psi_{xy})n^2 + (\psi_{xz} - \psi_{yz})nb_{||} + \psi_{zz}b_{||}^2]I_n^{(1)} -$$

$$- [(2\psi_{yy} + \psi_{xy})n - \psi_{yz}b_{||}]I_n^{(2)} + \psi_{yy}I_n^{(3)}\}. \qquad (5)$$

Here, $a = \frac{k_\perp}{\Omega_e}$, $p = 1/\alpha$, and

$$I_n^{(1)} = \frac{a^{2n-2}}{2^{2n}p^{2n+1}}\frac{\Gamma(n+1/2)}{[\Gamma(n+1)]^2}\times$$

$$\times {}_3F_3\left(n+1/2, n+1, n+1/2; n+1, n+1, 2n+1; -\frac{a^2}{p^2}\right),$$

$$I_n^{(2)} = \frac{a^{2n}}{2^{2n+1}p^{2n+3}}\frac{\Gamma(n+3/2)}{\Gamma(n+1)\Gamma(n+2)}\times$$

$$\times {}_3F_3\left(n+3/2, n+2, n+5/2; n+2, n+2, 2n+3; -\frac{a^2}{p^2}\right),$$

$$I_n^{(3)} = \frac{a^{2n+2}}{2^{2n+2}p^{2n+5}}\frac{\Gamma(n+5/2)}{[\Gamma(n+2)]^2}\times$$

$$\times {}_3F_3\left(n+3/2, n+2, n+5/2; n+2, n+2, 2n+3; -\frac{a^2}{p^2}\right),$$

$${}_3F_3(\alpha_1, \alpha_2, \alpha_3; \gamma_1, \gamma_2, \gamma_3; z) =$$

$$= \sum_{m=0}^{\infty}\frac{(\alpha_1)_m(\alpha_2)_m(\alpha_3)_m z^m}{m!(\gamma_1)_m(\gamma_2)_m(\gamma_3)_m}.$$

2.4 Further Simplification

With the non-relativistic condition, it is easy to prove that $\frac{a^2}{p^2} \ll 1$ (when $T_e = 10^6 k$, $\frac{a^2}{p^2} \sim 10^{-4}$). If we consider only the lowest power of $\frac{a^2}{p^2}$, Equation (4) can be simplified to

$$\frac{\Gamma_n}{\Omega_e} = -\frac{\pi}{G}\frac{\omega_{pe}^2}{\omega_r^2}(\frac{ck\sin\theta}{\Omega_e})^{4n-1}(\frac{2T_e}{m_e c^2})^{2n-3/2}\times$$
$$\times\frac{(2n-1)!!}{(n!)^2}\frac{1}{2^{3n}}\exp(-\frac{a^2}{p^2})[(\psi_{xx}+\psi_{yy}+\psi_{xy})n^3+$$
$$+\frac{k_\perp u_\parallel}{\Omega_e}(\psi_{xz}-\psi_{yz}+\psi_{xx}+\psi_{yy}+\psi_{xy})n^2+$$
$$+\frac{k_\perp^2 u_\parallel^2}{\Omega_e^2}(\psi_{xx}-\psi_{yz}+\psi_{zz})n+\frac{k_\perp^3 u_\parallel^3}{\Omega_e^3}\psi_{zz}], \qquad (6)$$

and $\Gamma(n+1/2) = (2n+1)!!\pi^{1/2}/2^n$, $\Gamma(n+1) = n!$.

3. Discussion

3.1 Directionality

From Equation (5) we find

$$\omega_i \sim (\sin\theta)^{4n-1},$$

so the magnitude of cyclotron resonance absorption is very sensitive to the propagation angle θ of the elctromagnetic waves: the value decreases rapidly

with decreasing θ. The same conclusion can also be derived from the classical formula (Zheleznyakov, 1973).

Note that the directionality of the electron cyclotron maser instability is quite different for different plasma parameters and different modes of the electromagnetic wave, which means that the electromagnetic waves excited by the cyclotron maser instability are not always propagating in the direction near the vertical to the magnetic field. For example, the directional angle of the fundamentals of the fast extraordinary modes is small for typical coronal parameters (Huang, 1987).

On the other hand, the frequencies of the peak values of the cyclotron resonance absorption are always in $n\Omega_e$ (n is an integer). But the frequencies of the peak values of cyclotron maser instability vary with different modes and θ (Huang, 1987).

The calculations of the directionality are summarized in Figures 1a,b.

3.2 Effect of T_e

From Equation (5) the absorption coefficients decrease with T_e, because

$$\omega_i \sim T_e^{2n-3/2} \exp(-\frac{m_e u_\parallel^2}{2T_e}),$$

which means that the lower the electron temperature, the larger the propability of the Maxwellian distribution near the origin of the velocity space, so the growth rates (depending on an integral along the resonant ellipse) decrease.

In addition, from Equation (3) when $u_{||} = 0$ or $\exp(\frac{-m_e u_{||}^2}{2T_e}) = 1$, and at the peak values ($\omega_r = n\Omega_e$),

$$\omega_{i,max} \sim T_e^{2n-3/2}.$$

The results of the relevant calculations are given in Figures 2a,b.

3.3 Effect of ω_{pe}/Ω_e

It is easy to find from Equation (5)

$$\omega_i \sim \frac{\omega_{pe}^2}{\Omega_e^2}.$$

So for given cyclotron frequency (or given magnetic field strentgh), ω_i increases with the ambient plasma density, because the more particles are in the wave-particle interaction, the stronger the cyclotron resonant absorption is (Figures 3a,b).

3.4 Absorption of $n = 1$

There are some special properties of cyclotron resonant absorption in the fast extraordinary modes at $n = 1$:

1. When $\omega_{pe}/\Omega_e < 1$, the refractive index of the peak value of the absorption at $n = 1$ is found to be in the range of the Slow extraordinary modes ($N > 1$), so the fast extraordinary modes deviate far from the peak value of the resonant absorption at $n = 1$.

2. Because $\omega_i \sim \sin^3\theta$ at $n = 1$ from Equation (5), and several terms in the brackets of (5) are related to θ, ω_i does not vary monotonically with θ. The highest peak value is near $\theta = 70°$, but the efffect of $\omega_i \sim \sin^3\theta$ is still important for the smaller values of θ (Figure 4)

3. In Figure 5, the relation of ω_i and T_e is similar to that in the Section 3.2, but the peak value of the absorption at $n = 1$ does not increase measurably with increasing T_e, because $\omega_{i,max} \sim T_e^{1/2}$.

4. It is interesting that at higher temperatures, the peak value of absorption at $n = 1$ decreases abruptly to the regions of $\omega_i > 0$ and a very narrow positive peak is found. This means that the high temperature plasma may excite the slow extraordinary modes directly (Figure 6).

4. Conclusion

The main point of this paper is that cyclotron resonance absorption is the opposite process of the electron cyclotron maser instability, so they can be described by the same model (Wu, 1985). This model is more strict than the classical single-particle theory, because the single-particle model can not be used to explain the strong plasma collective property, such as the resonant absorption; and the wave-particle interaction in the velocity space can not describe large-scale decay process of the electromagnetic waves directly. Also the imaginary and real parts of the wave-vector are not always in the same direction.

A formula for the resonant absorption coefficients is derived from plasma kinetic theory under the approximation of $\omega_i \ll \omega_r$ and $D_{ij}^a \ll D_{ij}^h$, and the main properties of the cyclotron resonant absorption are: 1. ω_i increases rapidly with increasing θ, 2. the peak value of ω_i increases rapidly with increasing T_e, 3. ω_i is directly proportional to the parameter ω_{pe}/Ω_e. 4. There are some special properties for the absorption of the extraordinary modes at $n = 1$, which will be studied further by the author. The formula is also valid for the absorption of the ordinary modes and Cerenkov absorption at $n = 0$.

Note that cyclotron resonance absorption will result in anisotropy of a Maxwellian distribution, which is the basic difference with collisional absorption. So it is a possible mechanism for the secondary acceleration, and to exite a new electromagnetic emmision. The average kinetic energy and density of the accelerated particles can be estimated by the theory in this paper. This subject will be discussed in a forthcoming paper.

I would like to thank the Smithsonian Astrophysical Observatory for awarding me a Predoctoral Grant. I also thank Dr. P. Martens for helpful comments and language editing. Studies of Coronal Plasma Processes at the Harvard-Smithsonian Center for Astraphysics are supported by NASA Grant of NAGW-112.

5. References

Benz, A.O.: 1986, Solar Physics 104, 99-110.

Gershman, B.N.: 1959, Zh. Eksp. i Teoret. Fiz., 37, 695.

Gershman, B.N.: 1960, Zh. Eksp. i Teoret. Fiz., 38, 912.

Ginzburg, V.L.: 1978, "Propagation of Electromagnetic Waves in Plasma". Academia Sinica Press, Beijing.

Huang, G.: 1987, Solar Physics 114, 363-373.

Li, H.W.: 1986, Solar Physics 104, 131.

Melrose, D.B.: 1984, Ap. J. 259, 844.

Sharma, A.R. and Vlahos, L.: 1984, Ap. J. 280, 405.

Stepanov, K.N.: 1958, Zh. Eksp. i Teoret. Fiz., 35, 283.

Vlahos, L. and Sharma, A.R.: 1985, Ap. J. 290, 347.

Wang, Z.X. and Guo, D.R.: 1979, "Theory of Special Functions", Academia Sinica Press, Beijing.

Wu, C.S.: 1985, Space Science Rev. 41, 215.

Figure Captions

Fig. 1a,b: The relation of the second and third absorptions of the fast extraordinary modes with the angle θ ($B = 200\ Gauss$, $n_e = 10^8 cm^{-3}$, $T_e = 10^6 k$).

Fig. 2a,b: The relation of the second and third absorptions of the extraordinary modes with T_e ($B = 200\ Gauss$, $n_e = 10^8 cm^{-3}$, $\theta = 60°$).

Fig. 3a,b: The relation of the second and third absorptions of the extraordinary modes with ω_{pe}/Ω_e ($B = 200\ Gauss$, $\theta = 60°$, $T_e = 10^6 K$).

Fig. 4: The relation of the absorptions of the extraordinary modes at

$n = 1$ with θ ($B = 200\ Gauss$, $n_e = 10^8 cm^{-3}$, $T_e = 10^6 K$).

Fig. 5: The relation of the absorptions of the extraordinary modes at $n = 1$ with T_e ($B = 200\ Gauss$, $\theta = 80°$, $n_e = 10^8 cm^{-3}$).

Fig. 6: The relation of the absorptions of the extraordinary modes at $n = 1$ with ω_{pe}/Ω_e ($B = 200\ Gauss$, $\theta = 80°$, $T_e = 10^6 K$).

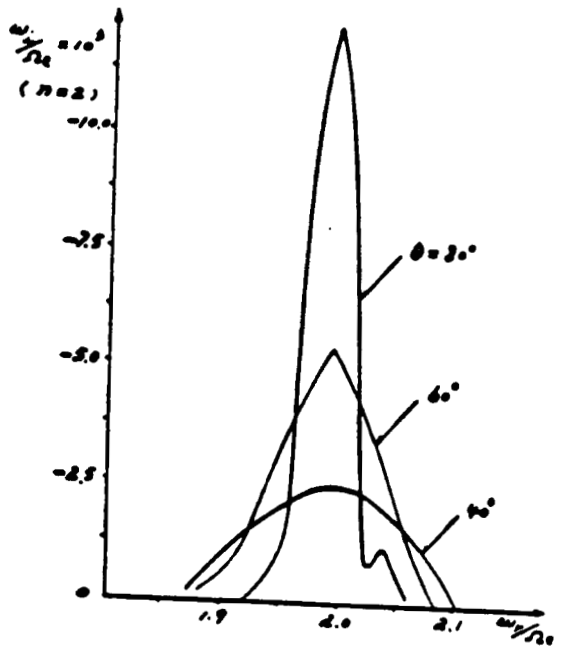
θ = 30°
60°
90°
1.9
2.0
2.1

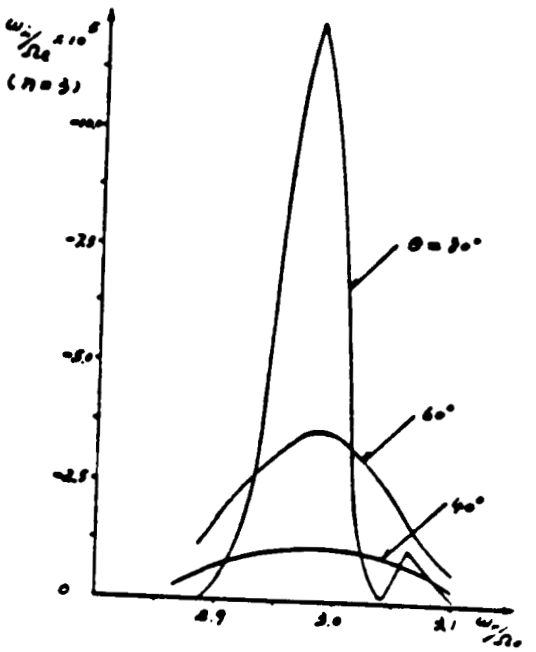
θ = 30°
60°
90°
2.9
3.0
3.1

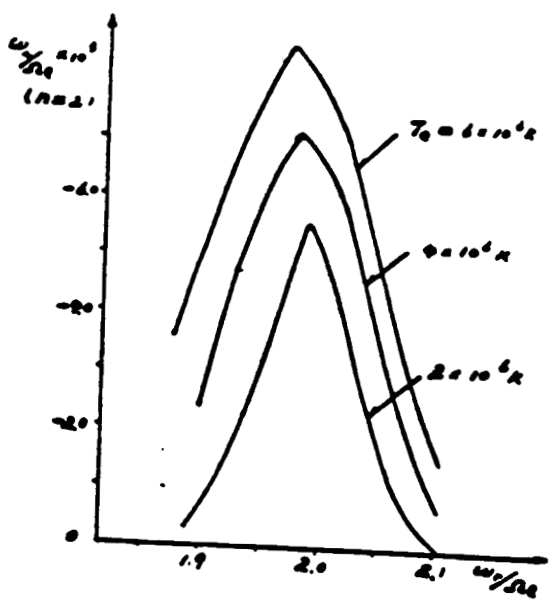
$T_0 = 6 \times 10^6$ K
4×10^6 K
2×10^6 K
1.9
2.0
2.1

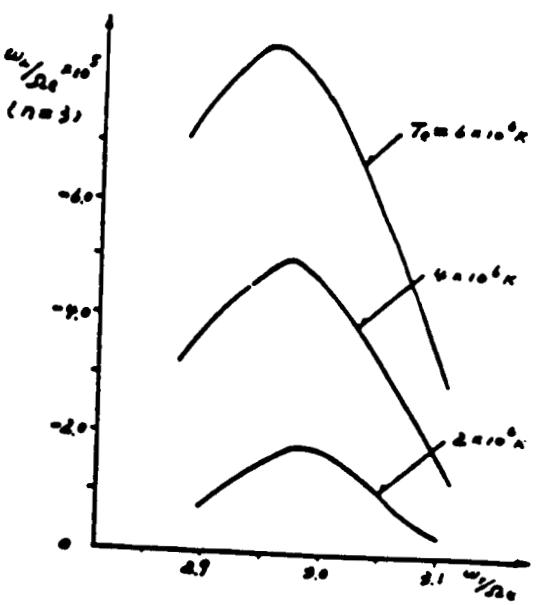
$T_0 = 6 \times 10^6$ K
4×10^6 K
2×10^6 K
2.9
3.0
3.1

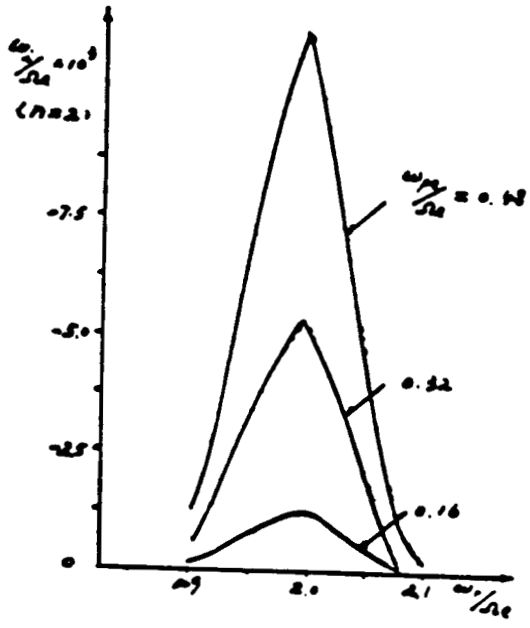
(n=2)
-7.5
-5.0
-2.5
0
0.32
0.16
2.0
2.1

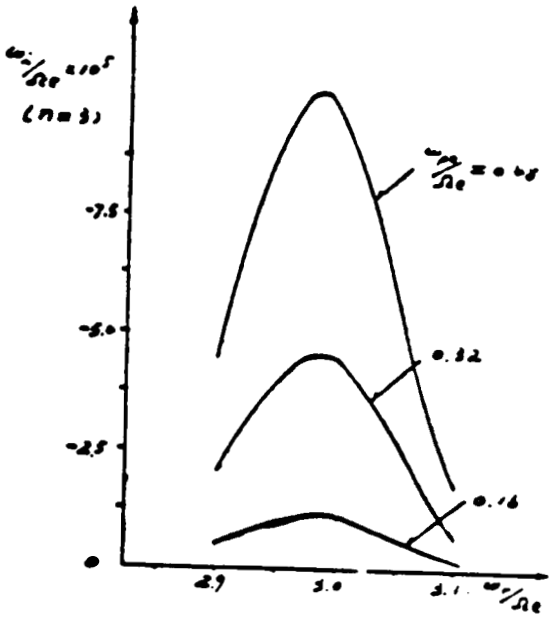
(n=3)
-7.5
-5.0
-2.5
0
0.32
0.16
2.9
3.0
3.1

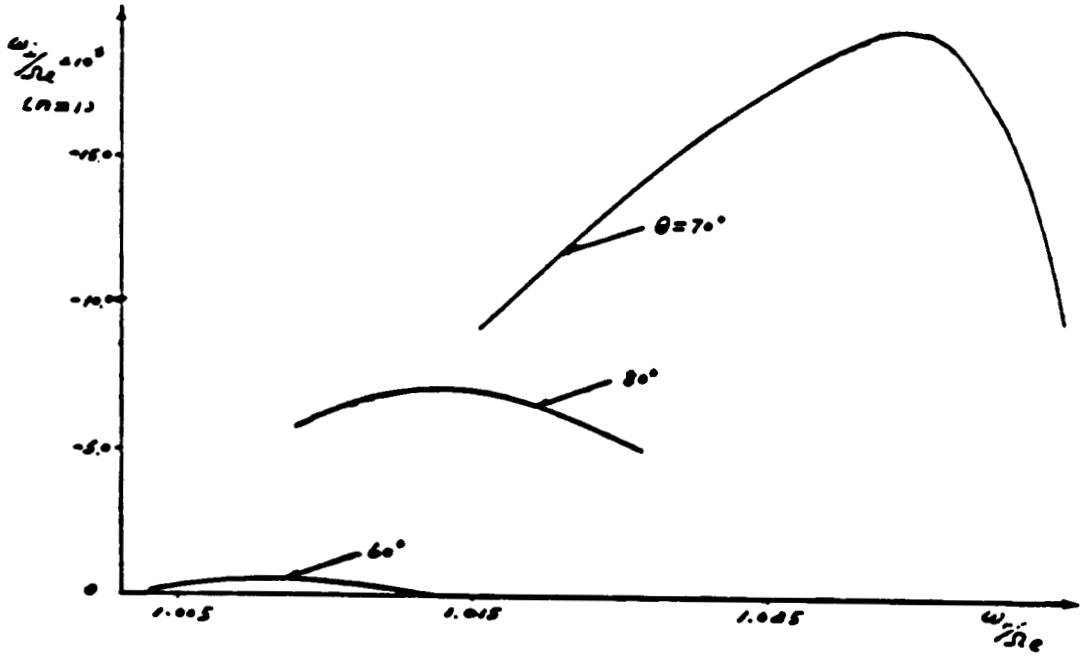
(n=1)
-15.0
-10.0
-5.0
0
θ=70°
80°
60°
1.005
1.015
1.025

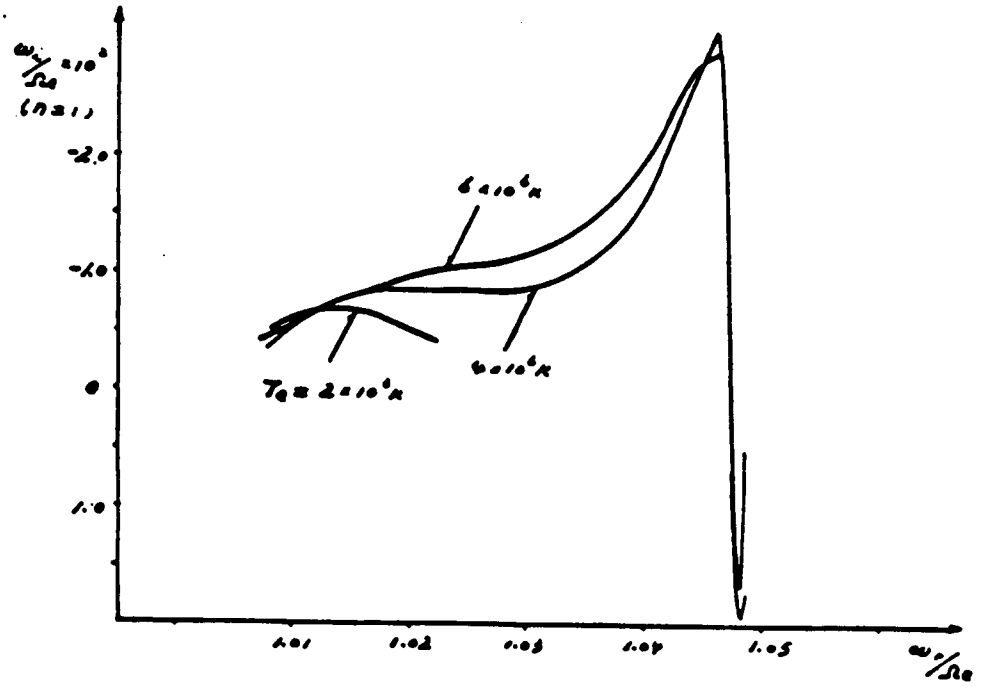
-2.0
-1.0
0
1.0
1.01
1.02
1.03
1.04
1.05

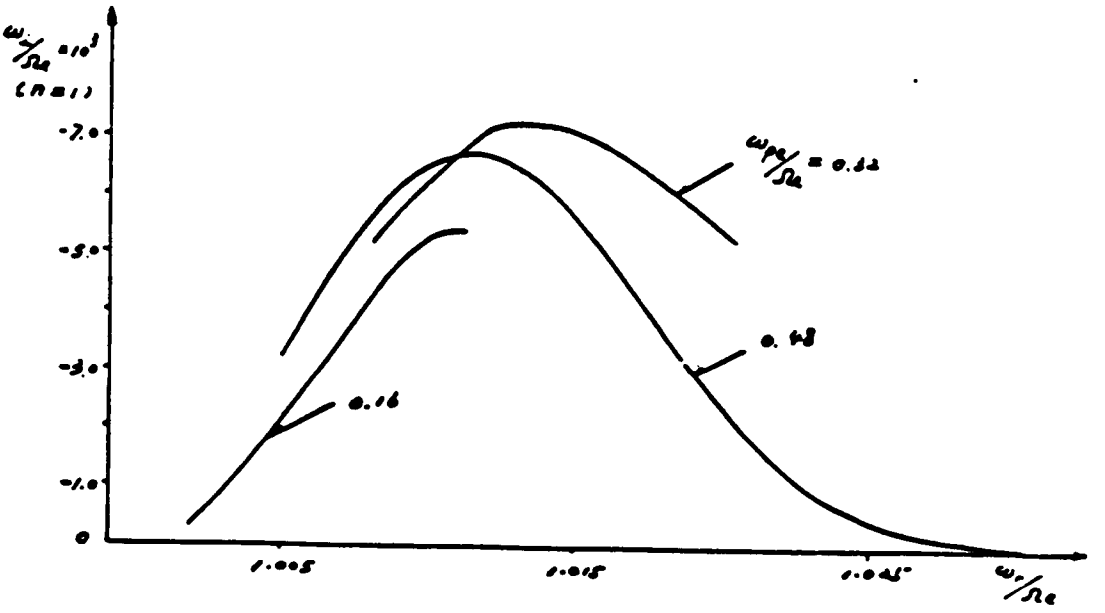
-7.0
-5.0
-3.0
-1.0
0
1.005
1.015
0.16
0.48

ACCELERATION MECHANISM OF THE PERIODIC TEARING MODES AND TIME SCALE OF THE SOLAR RADIO SPIKES

Huang Guang-Li

Purple Mountain Observatory, Academia Sinica, Nanjing, P.R. China
and
Harvard-Smithsonian Center for Astrophysics, Cambridge, MA 02138, USA

ABSTRACT

In this paper an extension of the classical theory of the tearing mode instabilities is discussed. It is suggested that the periodicity of the tearing modes should be considered, and that the induced electric field will be available to accelerate the energetic particles to excite the millisecond radio spikes in solar flares. Moreover, the period of the tearing modes agrees with the timescale of a single spike, and the characteristic time of the exponential growth of the tearing modes is comparable with the timescale of a group of spikes. So the evolution of the millisecond radio spikes may be explained by the quasi-periodicity of the accelerating electric field or the energetic particles.

INTRODUCTION

The particle acceleration mechanism is an important subject of solar flare physics; it deals with the process of magnetic energy conversion into the kinetic energy of particles, then to excite various electromagnetic radiations, including hard X-rays, Type III bursts, millisecond radio spikes, microwave radiation, etc.

It is noted that the source of radio spikes is close to the primary acceleration region; that is to say, the radio spike is a direct signature of the energetic particles /1/. On the other hand, the research of acceleration mechanism may deepen the understanding of emission mechanism of the radio spikes. As de Jager /2/ pointed out in his recent review, there are many kinds of acceleration mechanisms, but for an impulsive process (such as the radio spikes), the acceleration by electric field is the only possible mechanism. Solar radio spikes have attracted wide attention these years, and the electron cyclotron maser instabilities are today's most favored mechanism for the millisecond radio spikes in decimetric range /1/, many characters of which are explained by this theory: high bright temperature, narrow bandwidth, directionality, polarization, harmonic structure, etc. /3,4,5,6,7,8/.

However, many problems are still unclear, including the evolution of spike emission or the fine structure of a single spike and a group of spikes. This problem may be related to the properties of energetic particles or acceleration electric field /9,10,11/. So the question is to find a particle acceleration mechanism, which could accelerate the energetic particles needed to excite the millisecond radio spikes and explain the evolution of radio spikes.

Tearing Mode Instabilities and their Induced Electric Field

Restriction of the classical theory. The resistive tearing mode instability is one of the most important large-scale MHD instabilities. It may result in the disruption of plasma in tokamaks, so the tearing mode instability is studied intensively in laboratories and in theories of plasma physics.

In plasma astrophysics, Heyvaerts /12/ and Spicer /13/ also discussed the acceleration

mechanism of tearing modes. It is known that when resistivity is considered in the MHD equations, the hypothesis of frozen-in field line is no longer correct, and then the resistive MHD instabilities may be excited by the electric current (the free energy of magnetic field). Because of the shear of the magnetic field and the periodic boundary conditions, these instabilities can only be excited near some spatial magnetic surfaces, which are often called "rational surfaces". Therefore, in the classical theory of tearing mode instabilities /14/, a WKB approximation is used: the resistivity is considered only in a boundary layer, and the ideal MHD equations are still valid in other regions. Then the growth rates of the tearing modes (the real parts of eigenvalues) are derived from the continuity boundary condition.

But in the classical theory, the imaginary parts of eigenvalues are not taken into consideration. In fact the imaginary parts of eigenvalues describe the periodic oscillation of tearing modes, and the real parts of eigenvalues mean an exponential growth of the amplitude of oscillations. The author has shown theoretically /15/ that the evolution of nonlinear tearing modes is a quasi-periodic process. So its induced electric field and accelerated particles must vary with the same period, which may be used to interpret the evolution of radio spikes.

Derivations. The resistive MHD equations are /16/:

$$\partial\Psi/\partial t + (\vec{u}\cdot\nabla_\perp)\Psi = \eta\nabla_\perp^2\Psi - E \tag{1}$$

$$\partial U/\partial t + (\vec{u}\cdot\nabla_\perp)U = -S^2\hat{z}\cdot[\nabla_\perp\Psi \times \nabla_\perp(\nabla_\perp\Psi)] \tag{2}$$

$$\vec{u} = \nabla_\perp\Phi \times \hat{z} \tag{3}$$

$$\vec{B} = -r\nabla_\perp\Psi \times \hat{z} + \hat{z} \tag{4}$$

$$J_z = \nabla_\perp^2\Psi \tag{5}$$

$$U = -\nabla_\perp^2\Phi \tag{6}$$

Here Ψ and Φ are the potential functions of magnetic field $\vec{B}$ and velocity of magnetic fluid $\vec{u}$ respectively, η is the resistivity of the plasma, E is the electric field related to the electric current along the magnetic field lines; the parameter $S = \tau_R/\tau_H$, $\tau_R = a^2\mu_o/\bar{\eta}$, $\tau_H = R(\mu_o\rho_m)^{1/2}/B$, $r = a/R$, R and a mean the large and small radius of a toroidal plasma, $\bar{\eta}$ is the average resistivity of the plasma, ρ_m is the mass density of the magnetic fluid, μ_o is the magnetic conductivity in vacuum. Equations (1)-(6) are dimensionless: L/a, t/τ_R, $\eta/\bar{\eta}$, B/B_z, $J_z/(B_z/\mu_o R)$, Ψ/a^2B_z.

Then it is postulated that the growth of tearing modes depends mainly on the properties near the corresponding rational surface, and one is mainly interested in the evolution of tearing modes; hence, the solutions of (1)-(2) will be averaged in the boundary layer.

In the plane slab approximation, x is the radial coordinate, and y is the poloidal coordinate. Let:

$$\Psi = \Psi_o(x) + \Psi_1(x)\cos ky\, W(t) \tag{7}$$

$$\Phi = \Phi_1(x)\sin ky\, V(t) \tag{8}$$

Then the linear approximation of equations (1)-(2) can be written:

$$A\dot{W} + CV + DW = 0 \tag{9}$$

$$H\dot{V} + NW = 0 \tag{10}$$

$$A = \langle\Psi_1\rangle\cos ky \tag{11}$$

$$C = k\langle\Phi_1\Psi_o'\rangle\cos ky \tag{12}$$

$$D = -\eta\langle\Psi_1'' - k^2\Psi_1\rangle\cos ky \tag{13}$$

$$H = \langle\Phi_1'' - k^2\Phi_1\rangle\sin ky \tag{14}$$

$$N = S^2k\langle\Psi_o'\Psi_1''' - \Psi_1\Psi_o''' - k^2\Psi_o'\Psi_1\rangle\sin ky \tag{15}$$

Here $\langle\ \rangle$ means an average in the boundary layer, "." and "," express the derivatives of t and x respectively. Let:

$$X = -\omega_o WH/N \tag{16}$$

$$Y = V \tag{17}$$

$$\tau = \omega_o t \tag{18}$$

$$\omega^2_o = -CN/AH \tag{19}$$

Equations (9)-(10) can be written as:

$$-\dot{X} + Y = 0 \tag{20}$$

$$\dot{Y} + X + Y = 0 \tag{21}$$

$$g = D/\omega_o A < 0 \tag{22}$$

It is easy to find the solutions of equations (20)-(21):

$$X = c_1 \exp(-g\tau/2) \cos\tau \tag{23}$$

$$Y = c_2 \exp(-g\tau/2) \sin\tau \tag{24}$$

c_1 and c_2 are the integral constants, and the condition $|g| < 1$ is used.

Discussion

Comparison with the classical theory. From equations (23), (19), (11)-(15) and (3)-(6), the growth rates of the tearing modes are:

$$-g\omega_o/2 = k\eta \langle J_{z1}\rangle / \langle B_{x1}\rangle \tag{25}$$

If the parameter Δ' and the width of boundary layer h are defined:

$$\Delta' = \langle B_{x1}'\rangle h/\langle B_{x1}\rangle \tag{26}$$

Then from Ampere's law:

$$\langle J_{z1}\rangle = \Delta'\langle B_{x1}\rangle/kh \tag{27}$$

the growth rate in (25) may be changed into:

$$-g\omega_o/2 = \eta\Delta'/h \tag{28}$$

This is the result of Bateman /17/, and because:

$$h \sim S^{-2/5} (\Delta')^{1/5} \tag{29}$$

$$-g\omega_o/2 \sim \tau_R^{-3/5} \tau_H^{-2/5} (\Delta')^{4/5} \tag{30}$$

This is consistent with the classical theory /14/. On the other hand, the imaginary part of eigenvalue can be derived from (19), (11)-(15), and (5)-(8):

$$\omega_o^2 = k^2 S^2 \langle B_{yo} u_{x1}\rangle \langle B_{yo} J_{x1} + B_{xy} J_{z}'_{o}/k\rangle / (r\langle B_{x1}\rangle \langle U_1\rangle). \tag{31}$$

In fact, (31) is the dispersion equation of tearing modes.

Quantitative analysis. In the typical coronal condition: $R \sim 10^4$km, $a \sim 10^2$km, $r = a/R = 10^{-2}$, it can be estimated from the MHD equations /16/: $B_{yo} \sim r$, $u_{x1} \sim r$, $J_{z1} \sim r^2$, $B_{x1} \sim r^2$, $J_{z}'_{o} \sim r$, $U_1 = |\nabla_\perp \times \vec{u}| \sim r$ ..., the period of tearing modes equals:

$$T = \tau_R/\omega_o \sim \tau_R r/s \sim \tau_H r \sim 10^{-2} \text{ sec.} \tag{32}$$

This is comparable with the typical duration of a single spike. Moreover, the characteristic time of the exponential growth of the tearing modes is:

$$\tau_R/g\omega_o \sim \tau_H \sim 1 \text{ sec} \tag{33}$$

This is of the same order as the typical duration of a group of spikes. Otherwise, the phase velocity of tearing modes may be estimated by (31):

$$\omega_o^2/k^2 \sim a^2 S^2 / (\tau_r^2 r^2) \sim R^2 / \tau_H^2 = u_A^2 \tag{34}$$

This is just the value of Alfven velocity.

Note that the parameter $|g| \sim r \ll 1$.

Properties of the induced electric field. The typical order of magnetic field B in the corona is $10^2 G = 10^{-2} T$; therefore $B_1 \sim r^2 B_o \sim 10^{-4} T$, and $u_A \sim 10^6$ m/sec /18/. Then the induced electric field can be derived by Faraday's law:

$$E_1 \sim \omega_o B_1 / k \sim 1 \quad v/m.$$

This electric field can accelerate an electron to tens of KeV during a period of the tearing modes and satisfy the requirement of the radio spikes for the energetic particles.

Spicer /13/ estimated the induced electric field by the exponential growth rates:

$$E_1 \sim g\omega_o B/k \sim 10^{-2} \quad v/m.$$

This value is two orders of magnitude smaller than that in (35). On the other hand, the characteristic length of E_1 is: $L \sim a \sim 10^2$-km, which equals the distance passed by an electron at the velocity of light during a millisecond. The energy gain of an electron over this length scale is indeed several tens of KeV.

INTERPRETATION OF THE TIME STRUCTURE OF THE RADIO SPIKES

From the momentum equation of an electron:

$$m_e d\vec{v}/dt = e\vec{E}_1 \cos \omega_o t \tag{36}$$

it is easy to get:

$$\vec{v} = e\vec{E}_1 / m_e \omega_o \sin \omega_o t + \vec{v}_o. \tag{37}$$

Here the amplitude of velocity $eE_1/m_e\omega_o$ is about equal to 10^8 m/sec, which is of the same order of magnitude as the velocity of light in vacuum. Moreover, in a given direction the energetic electron beam is not uniform but of a periodic intermittence.

It is noticed that the growth of electron cyclotron maser instabilities depends on the energetic electron beam, so the intermittence of the beam will make the spike emissions decay rapidly to the background level. Otherwise in (31) the frequency ω_o is proportional to B_{zo}. That means the acceleration time decreases with increasing the magnetic field, which may be used to explain why the duration of radio spikes decreases with increasing the frequency /1/ For example, the duration of radio spikes in the metric range is one or two orders of magnitude larger than that in the decimetric range.

SUMMARY

In this paper an extension of the classical theory of tearing mode instabilities is discussed. It is suggested that the periodicity of tearing modes should be considered, and that the induced electric field will be available to accelerate the energetic particles that excite the radio spike emission. Moreover, the period of the tearing modes corresponds with the time scale of a single spike, and the characteristic time of the exponential growth of the tearing modes is comparable with the time scale of a group of spikes. Therefore the acceleration mechanism of the periodic tearing modes gives a reasonable model to describe the millisecond radio spikes in solar flares.

REFERENCES

1. A.O. Benz, Solar Phys. 104, 99 (1986).

2. C. de Jager, Space Science Rev. 44, 43 (1986).

3. D.B. Melrose, Astrophys. J. 259, 844 (1984).

4. A.R. Sharma and L. Vlahos, Astrophys. J. 280, 405 (1984).

5. L. Vlahos and A.R. Sharma, Astrophys. J. 290, 347 (1985).

6. H.W. Li, Solar Phys. 104, 131 (1986).

7. G. Huang, Solar Phys. 114, 363 (1987).

8. G. Huang, Publications of Purple Mountain Obs. in press (1988).

9. H.W. Li, Solar Phys. 111, 167 (1987).

10. G. Huang, Acta Astrophys. Sinica, in press (1988).

11. G. Huang, Acta Astrophys. Sinica, submitted (1988).

12. J. Heyvearts, Astron. AstrophysAstrophys. 37, 65 (1974).

13. D.S. Spicer, Solar Phys. 53, 305 (1977).

14. H.P. Furth, Phys. Fl uids 6, 459 (1963).

15. G. Huang, Acta Phys. Sinica 36, No. 10, 1024 (1987).

16. B.V. Waddel, Phys. Fluids 22, 896 (1979).

17. G. Bateman, MHD Instabilities, Atomic Publishing House, Beijing (1982).

18. E.R. Priest (ed.), Solar Flare Magnetohydrodynamics, Oxford, London (1983).